CALIFORNIA INSTITUTE OF TECHNOLOGY

DANIEL AND FLORENCE GUGGENHEIM JET PROPULSION CENTER

SOME EXPERIMENTS RELATED TO

L-STAR INSTABILITY IN ROCKET MOTORS

R. N. Kumar and R.P.McNamara

March 1973

SOME EXPERIMENTS RELATED TO L-STAR INSTABILITY

IN ROCKET MOTORS

by

R. N. Kumar and R. P. McNamara

Approved F. E. C. Culick

March 1973

Daniel and Florence Guggenheim Jet Propulsion Center
California Institute of Technology
Pasadena, California

SOME EXPERIMENTS RELATED TO L-STAR INSTABILITY
IN ROCKET MOTORS

R. N. Kumar and R. P. McNamara

California Institute of Technology, Pasadena, California

ABSTRACT

This project explores the role of solid phase heterogeneity on the low-pressure L^* instability of non-metallized AP/PBAN propellants. Four particle size distributions (fifty per cent weight average points at 11μ, 39.5μ, 175μ, and 350μ) are employed in propellants that are otherwise identical. Over one hundred test firings were conducted in the $2\frac{1}{2}"$ diameter L^* burner at JPL. Pressure time histories in the chamber and color movies of two firings constitute the raw data.

An economical firing program has been used. It enables the interesting range of L^* values to be covered during a single firing (at a set mean pressure), through the variations in the depleting propellant volume.

Time-independent combustion, Helmholtz mode, chuff mode, and the pressure-burst phenomena are revealed as the principal signatures. Of these, the Helmholtz mode is found to be the most ordered form of instability.

Motion pictures show the one-dimensional nature of the Helmholtz instability; frequency of oscillations is found to bear a much stronger relation to the characteristic residence time $(a/\bar{r})$ in the solid than to the characteristic heat transfer time $(\varkappa/\bar{r}^2)$; simple correlations of the frequency with L^* are found to be of limited validity.

The stability boundary on the $L^* - \bar{P}$ plot is found to be parabolic (with dual pressure values at a given value of L^*), although experimental difficulties

have prevented the obtaining of full loci for all four of the propellants. The predicted value of the high pressure stability limit is found to be excellent for the 11 μ propellant, but less convincing for the other three.

The amplitudes of pressure oscillations are found not to correlate satisfactorily with any of the chamber (or propellant) variables. The closest correlation is with a parameter based on the concept of volumetric energy release rate in the chamber.

Many features of the 11 μ oxidizer propellant are found to be significantly different from those of the other three <u>even on a qualitative basis.</u> Also, many of the variations in the dynamic characteristics (normalized frequency, for example) are <u>not</u> monotonic with the oxidizer particle size variations.

The chuff mode combustion is found, through color movies, to be far from one-dimensional or steady. The events behind a chuff are found to be random and statistical in nature.

The role of the condensed phase details in the unstable combustion is repeatedly emphasized in the present work; the oxidizer particle size is revealed as an important parameter in the instability.

ACKNOWLEDGMENTS.

TABLE OF CONTENTS

SOME EXPERIMENTS RELATED TO

L-STAR INSTABILITY IN ROCKET MOTORS

I. INTRODUCTION

It is almost paradoxical that the simplest of rockets is the hardest to understand. The state of the art with the mechanically complex liquid propellant rockets is one of theoretical predictability. The same is nearly the case with the less complex hybrid rockets, at least over a significant regime of operation. Performance predictions of the simple solid propellant rockets depend almost totally on empirical information. This state of affairs with the solid propellant rockets may be attributed to two causes. One is the difficulty of combustion modeling, and the other is the lack of fundamental chemical-kinetic/fluid-dynamic data from laboratory scale experiments. The two are, however, intimately related, for any theory needs a set of reproducible experimental data as its basis.

Added to the above mentioned fundamental difficulty with the solid propellant rockets, unstable operation has been observed as probably the most serious problem challenging successful applications. To a large extent, the difficulty with the instability problem is no doubt associated with a lack of knowledge regarding the fundamental combustion processes. The situation should improve with more research effort. However, another factor of great relevance is the lack of good experimental data covering the unstable operation of full-scale rockets. Data on actual rocket instability, even if made available, would be difficult to process because of the complex combinations of the parameters involved. Thus, experiments are to be conducted where the parameters are isolated and their variations are controlled.

Quite often, an experimental work planned to yield meaningful scientific information appears to be rather isolated from contemporary rocket technology. Research on the oxidizer and the fuel separately, non-metallized propellants, unimodal oxidizer distributions are typical examples. However, the benefits from such fundamental work, planned to lead into the close neighborhood of actual rockets, are to be appreciated. Frequently, the results from even the initial stages of such a long range program are directly applicable to actual rocket propellants, thereby enhancing the value of such research.

The present work was undertaken to obtain experimental data from tests, where the influences of compositional variables (in propellant formulation) on instability behavior are explored. The compositions of the state-of-the-art solid propellants are extremely varied. In order to understand, in a non-empirical manner, the effects of compositional variations, the simplest of experiments was designed. Only a single compositional parameter was varied, and the propellants were fired under very similar motor conditions.

A survey of pertinent literature is not one of the aims of the present report. No attempt is made to cite a reference except when very direct relations arise with the present studies. Also, it is not our aim to treat the experimental data theoretically. But for a few qualitative arguments related to correlations of experimental data, no attempt is made to theoretically account for the observed experimental trends. The presented experimental data should provide a working ground for future theoretical efforts.

In this introductory chapter, the reader is familiarized with the two primary aspects of the present research effort, namely the propellants and the instability mode. The main results and conclusions are also briefly summarized.

The propellant chosen must be readily unstable and must possess a simple composition. Previous experience at JPL had indicated that the NWC A-13 propellant is one that exhibits oscillatory combustion readily. The standard A-13 propellant has a unimodal distribution of AP oxidizer with polybutyl acrylonitryl acrylic acid polymer as the binder, with the EPON resin as the curing agent. The processing of the propellant from the ingredients is described in Chapter II. The details of the mixer and the mixing schedule are included for an important reason. It has been a matter of experience at JPL that propellant batches with identical compositions and ingredients have been known to reveal different characteristics depending on the mixer in which they are processed. A consequence of this discovery has been using different mixing schedules for the same propellant in different mixers. It is possible that the specific mixing action of the blades has an important influence on the curing of the propellant. In the present case, since all of the propellants used the same mixer, the relative effects on mixing are expected to be similar, if not identical.

Since the basic aim was to understand the manner in which the instability behavior of solid propellants would be affected by variations in propellant formulation, the simplest instability mode for examination was chosen as the familiar L-star mode, where the oscillations occur simultaneously in the bulk of the chamber leading to the earlier nomenclature "bulk mode instability" or "non-acoustic instability." (It has since been theoretically clarified, however, that the oscillations are the zeroth mode in a standard sequence of acoustic modes.) The L^* oscillations have been observed at relatively low pressures (a few atmospheres). Low pressures simplify the experimental set up.

Among the various parameters that characterize propellant formulation, a single parameter was selected to be varied over a significant range. Varying too many parameters at the same time leads to results that would be difficult to interpret. Oxidizer particle size was chosen as having a significant influence over the ballistic properties, besides being a simple parameter. Assuming complete combustion, the far-downstream quantities (flame temperature, species fractions, etc.) are not affected by oxidizer particle size. Steady-state linear burning rates of many propellants have been known to be significantly affected by AP particle size. A study of the literature[5, 7] indicates that oscillatory combustion characteristics are also affected, although a systematic study of the influences of this single parameter is not readily available.

Ideally, one would like to have a truly unimodal (Delta function) distribution of spheroidal particles of AP. In practice, easy availability dictated the choice of the distributions employed in the present study. The distributions used are shown in fig. 1.1 along with the names of the propellants they are used in. The $\widetilde{A}$-13 propellant used here was cast at JPL, as contrasted with the standard A-13 propellant supplied by the Naval Weapons Center. At this stage, it is worth pointing out that these oxidizer particle distributions are conventionally known as Ground AP, 90 μ AP, Unground AP, and 400 μ AP, in the order of increasing coarseness. However, as can be seen from fig. 1.1, this conventional nomenclature is not very descriptive of the true distributions. Throughout the present report, in order to maintain a consistent nomenclature, the 50 per cent weight point has been used to identify a distribution. Thus, 11 μ, 39.5 μ, 175 μ, and 350 μ are the oxidizer particle sizes associated with the propellants CIT-2, $\widetilde{A}$-13, CIT-3, and CIT-4, re-

Fig. 1.1 The AP Particle Size Distributions Used in the Four Propellants of the Present Program.
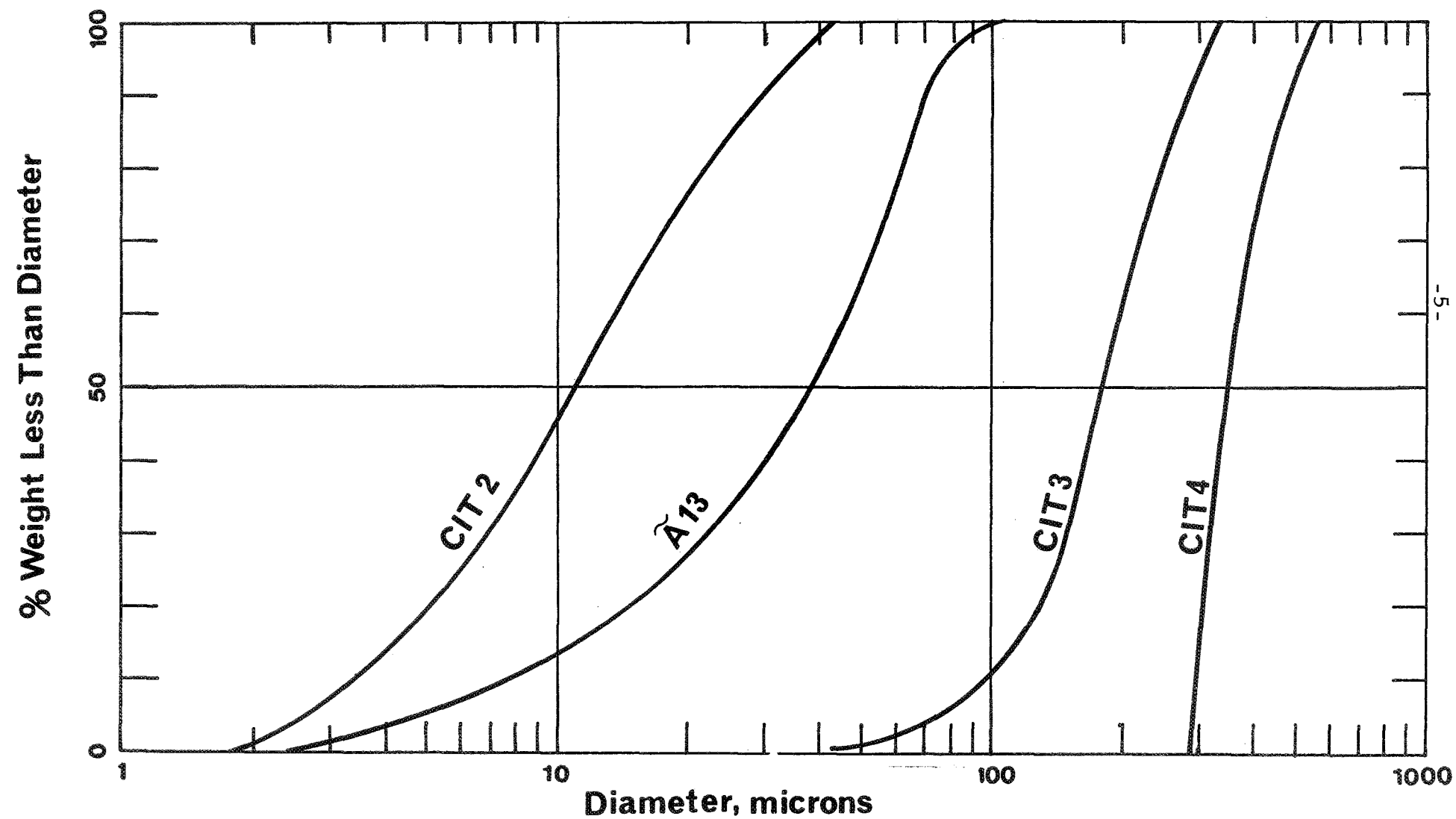
spectively. The diligent reader who may be wondering about the conspicuous absence of a CIT-1 propellant is informed that such a propellant was indeed formulated, but had a short history, to describe which no more than three figures of the present report would suffice.

The testing consisted of over one hundred and eighty firings during the period January - October 1972. Apart from the four propellants of the present report, the tests also covered a few other propellants not reported here. A very economical firing program, discovered early in these studies, was employed. The importance of ignition to the pressure-time history was felt in various different forms. A new ignitor paste was formulated, and it proved very helpful for use with the coarser oxidizer particle propellants.

Of the two principal modes of unstable combustion (namely, chuff and Helmholtz), the Helmholtz mode was found to be ordered, and hence maximum attention was given to its understanding.

Motion pictures through a transparent burner showed the one-dimensional nature of combustion during the Helmholtz mode. The three principal characteristics of unstable operation (examined in detail) were the frequency of Helmholtz oscillations, the stability boundary, and the amplitude of fluctuating pressure. The frequency was found to bear a much stronger relation to the characteristic residence time $(a/\bar{r})$ in the condensed phase than to the characteristic heat transfer time $(\varkappa/\bar{r}^{2})$. Also, simple correlations of frequency with the chamber characteristic length (L^{*}) were found to be of limited validity only.

The stability boundary, on the L^{*} - $\bar{P}$ plot, was found to be parabolic in shape, although experimental difficulties prevented the obtaining of the full locus for all of the propellants. The high pressure limit for unconditional

stability was predicted based on postulated importance of the rôle of the condensed phase as a heat reservoir. The agreement was found to be excellent for the CIT-2 propellant (11 µ), but less convincing for the other three.

The amplitudes of pressure oscillations were found not to correlate satisfactorily with any of the chamber or propellant variables. The closest correlation was with a parameter based on the concept of volumetric energy release rate in the chamber.

Many features of the finest oxidizer particle propellant (CIT-2) were found to be significantly different from those of the other three even on a qualitative basis. Also, many of the variations in the dynamic characteristics (normalized frequency, for example) were not monotonic with the oxidizer particle size variations.

The chuff mode combustion was revealed, by color movies taken through a transparent chamber, to be far from one-dimensional or steady. The events behind a chuff (a pressure spike) were found to be random and statistical in nature.

Finally, the role of the condensed phase details in unstable combustion was repeatedly emphasized in the present work, both during the testing phase and during the data processing phase. The extensive experimental data now invite theoretical research efforts.

CHAPTER II. THE PROPELLANTS

The propellants are simple variations of the NWC A-13 propellant.
The composition is shown in Table I.

With the exception of the first nine (exploratory) tests, all of the tests
used propellants processed in the JPL 5-gallon BEKEN mixer. Each batch
employed a standard load of 15 lb. ingredients. The mixing was carried out
mechanically under vacuum conditions (pressure levels under 0.15" of mer-
cury). The mixer is shown in fig. 2.1. The mixing chamber is heated by a
hot water jacket. The temperature of the inflowing water is measured by a
thermocouple and the control is achieved by premixing of hot and cold waters
entering the inlet manifold. A servomechanism controls the water temperature
at any preset level. However, the thermal inertia of the jacket heater system
is high enough to prevent a set temperature being reached within the relatively
short time of mixing (15 - 30 minutes). Hence, the initial setting was tempo-
rarily kept several degrees higher than the desired value. The setting was,
however, lowered to the desired temperature after the jacket temperature
reached approximately 90 per cent of the full value. In this manner, the jacket
was maintained near the optimum temperature during most of the mixing period.

The mixer blade details are shown in fig. 2.2. The central blade is
completely stationary. The outer blade mounted on the moving arm rotates
around the central blade, simultaneously spinning around its own axis. A
gear box enables the selection of forward or reverse action. The speed can
be chosen as Fast (28 RPM rotation, 84 RPM spinning) or Slow (7 RPM rota-
tion, 21 RPM spinning). Only the Fast speed was used in all of the present
processing. The temperature of the propellant (ingredients) that is being
mixed is measured by a thermocouple junction housed in the tube seen on the
axis of the inner (stationary) blade. The mixing chamber can be raised and

Table I. Composition of the Propellants

		weight per cent
Binder:	Poly Butyl Acrylo Nitrile Acrylic Acid (PBAN)	20.4
	Epon Resin 808	3.6
Oxidizer:	Ammonium Perchlorate (AP or NH_4ClO_4)	76.0

- - - - - - - - - - - -

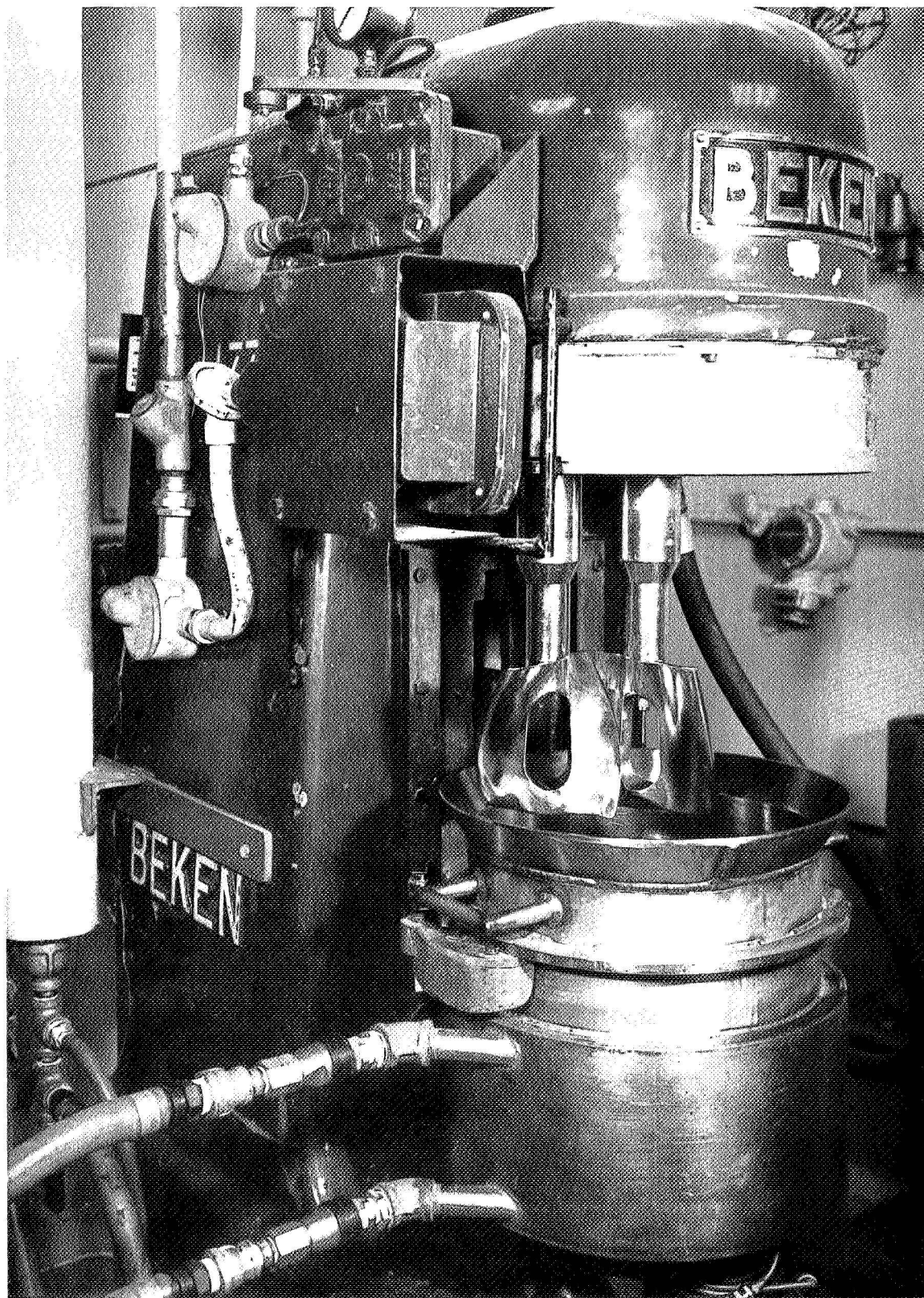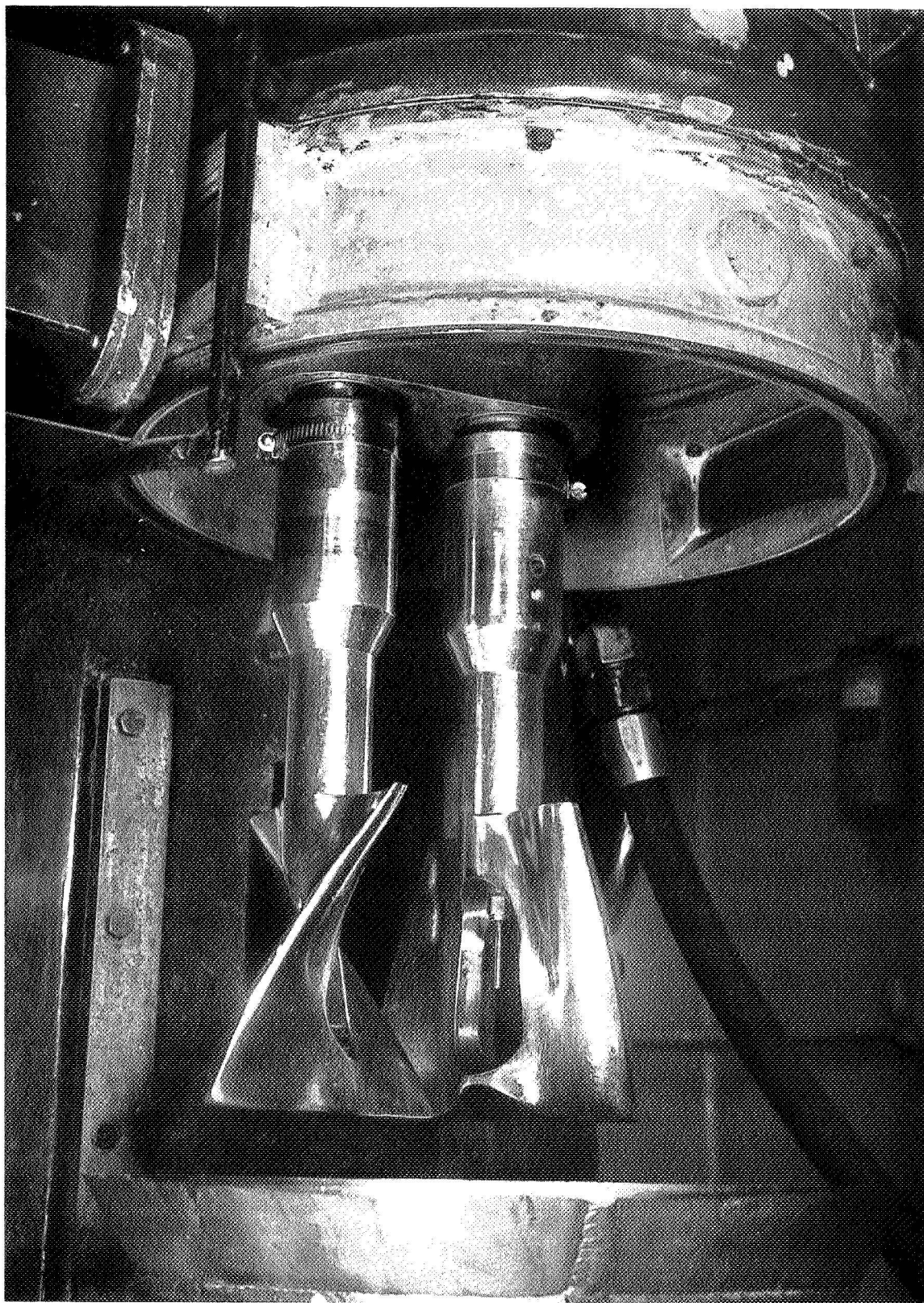| Density	1.56 gm/cc
Flame temperature at 300 psig	$2100^{\circ}K$

Fig. 2.1   The Five Gallon Mixer

Fig.2.2   The Mixer Blades

lowered vertically through a rack-and-pinion mechanism actuated by a hand wheel. In the fully raised position, the mixing chamber seals vacuum with the "O" ring in the head of the mixer. In that position there is a 3/16" clearance between the bottom of the mixing chamber and the bottom edge of the blades. There is a 1/8" clearance between the maximum radial reach of the blade and the side wall of the mixing chamber. Transparent windows in the mixer head afford a view of the ingredients while being mixed. Closed-circuit TV arrangement has to be used for visualization in the adjoining control room since the presence of personnel inside the mixing room during mixing is against safety regulations.

After mixing is complete, the uncured propellant is cast into the desired molds under vacuum. As shown in fig. 2.3, the tubing leading from the mixing chamber to the casting enclosure is also heated (by a water coil) to prevent hardening of the propellant in the tube. To prevent the occurrence of hollow pockets inside a mass of propellant, the flow of the propellant into the molds is carefully regulated to be a thin ribbon through the use of a "ribbon former." The CIT-2, $\widetilde{A}$-13, and CIT-3 propellants used the standard slot ribbon former (7 holes of 0.04" diameter each). It was discovered that the slots were too small for the CIT-4 propellant so that a conical ribbon former (with 1/8" clearance between its rim and the casting spout) was used for this propellant. The casting was done on a vibrator table (with compressed-air actuation).

The molds were kept in the 160°F oven for the desired time (4 days) for curing, after which the propellants were stored in the ambient temperature oven.

In all of the present runs cylindrical charges were employed. The thickness was either 1/4" or 3/8" (a 1/2" thick propellant was used once).

Fig.2.3   Vacuum   Casting

The cast cylinders are cut (in a mechanical saw) slightly thicker than the desired thickness. Final finishing to accurate dimensions is accomplished on a milling machine using an end mill. The propellant is held on the table through vacuum and the "chips" are cleared away by a vacuum suction system. The physical appearance of the four propellants is shown in fig. 2.4 along with the oxidizer particle size distributions used in them. The texture variations can be clearly seen.

The steady-state linear regression rate of a propellant as a function of pressure is an important characteristic. Satisfactory performance in comparison with previous data, smooth trends, and, indeed, an initial assessment of the very success or failure of a batch of propellants are reflected in the regression rate versus pressure data. The data were obtained in the Crawford bomb. The cast strands (approximately circular in cross section, with an effective diameter 1/4", length 7") are coated with the restrictor paste (87 % MEK, 10 % ethyl cellulose 10 cps.[*] and 3 % tricresolphosphate). Three holes are drilled, perpendicular to the axis, for electrical wires. The first houses the ignitor wire (nichrome, 28 gage). The second and the third house the 0.00025" copper timing wires spaced exactly 5 inches apart. The jig used for drilling the holes in a propellant strand is shown in fig. 2.6. The experimental linear regression rates obtained under nitrogen pressure are shown in fig. 2.7. In a recent work,[4] it was theoretically predicted that changes in oxidizer particle size without affecting any of the other compositional parameters should result in a variation in the linear regression rate but with little change in the burning rate index n. The present experimental data, which show approximately the same index for all four of the propellants, thus provide an encouraging support for that theoretical prediction.

---

[*] centipoise
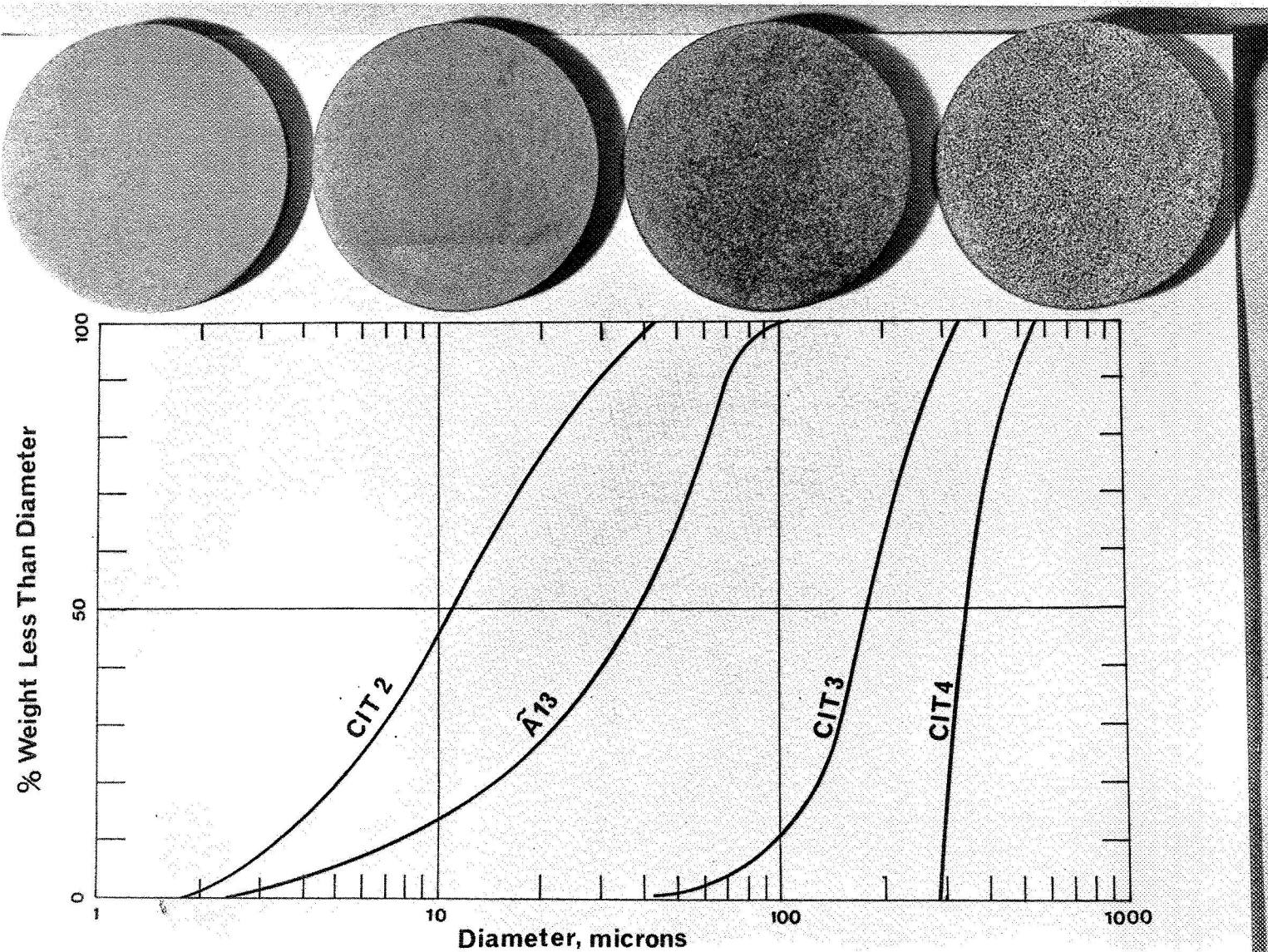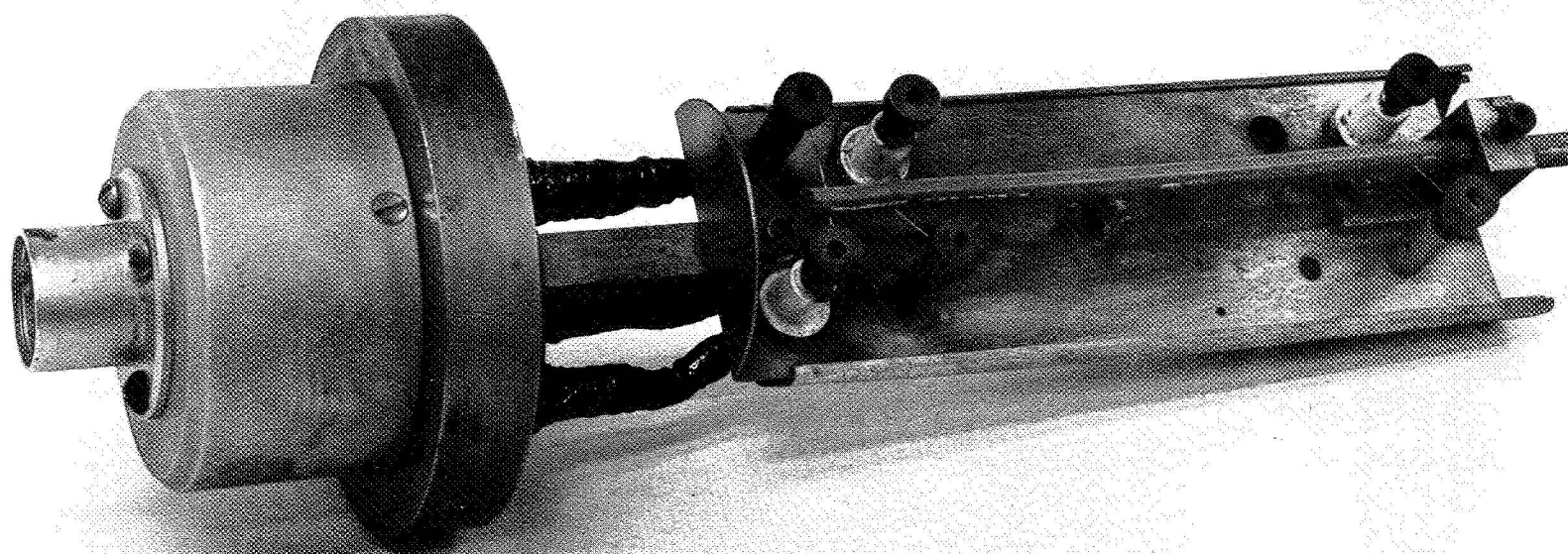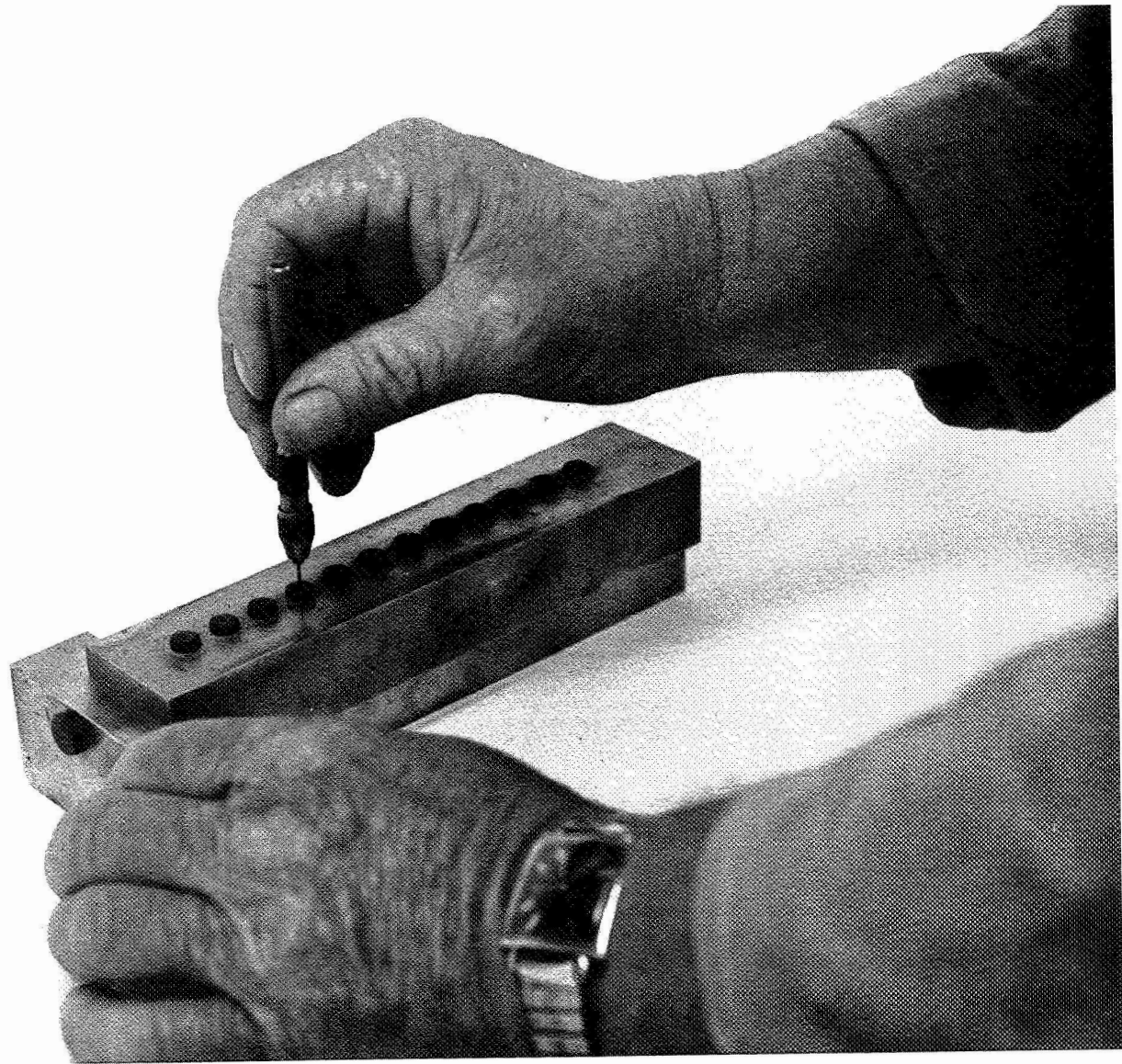
Fig. 2.4 The Propellants

Fig.2.5 The Strand-Holder

Fig.2.6 The Strand-Jig
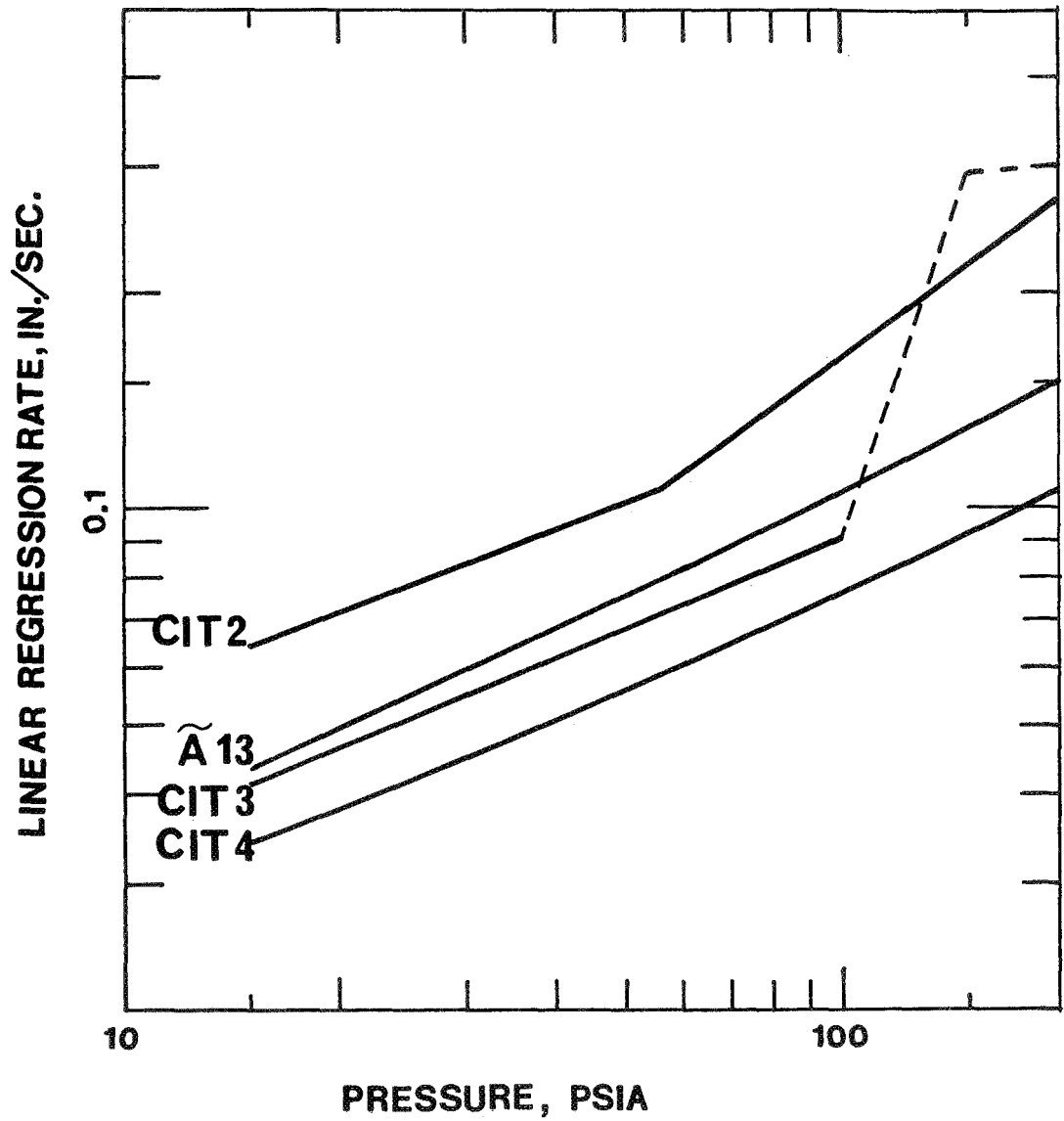
Fig. 2.7 Crawford Bomb Data on the Propellants.

III. TEST FACILITY AND INSTRUMENTATION

The test facility consists of the L-star burner, control and data acquisition instruments. These have been described in detail by the previous investigator[1]. Here, it suffices to recall that the burner (fig. 3.1) is a $2\frac{1}{2}$" (inside diameter), 5" long cylindrical chamber (C) with a nozzle end plate (N) and a piston end plate (E). The propellant disc is bonded to the piston (P) which is mounted at the end of a centrally-located screwed rod, the axial position of which enables the selection of different chamber volumes. The assembled view is shown in fig. 3.2, where the propellant surface coated with the ignitor paste is seen through the transparent nozzle end plate. The transparent end plate was used only in a few of the runs, when flow visualization inside the chamber was desired. All other tests used the stainless steel nozzle end plate.

Towards the end of the present program, the need was felt for low (subatmospheric) back pressures. The L*-burner was modified slightly to exhaust into a vacuum manifold. The modified design and the vacuum manifold are described in Appendix I.

The control instrumentation consisted of the "Test" and "Fire" circuitry (fig. 3.3).

The data acquisition instrumentation consisted of a pressure transducer[*] (Teledyne, models 217-SA, 0-100 and 176-SA, 0-300 psi) that communicates with the chamber through a short length (approximately 3") of 1/4" stainless steel tubing. Distortion of the pressure signal through the tubing should be negligible considering that only bulk-mode oscillations are encountered. The electrical output from the Taber gage was passed through an amplifier (General Dynamics, D.C. -10 K Hz, flat) and recorded on a CEC 5-124 oscillograph. A Tektronix storage oscilloscope was connected

---

[*]Taber gage

Fig. 3.1 The L*-Motor Disassembled
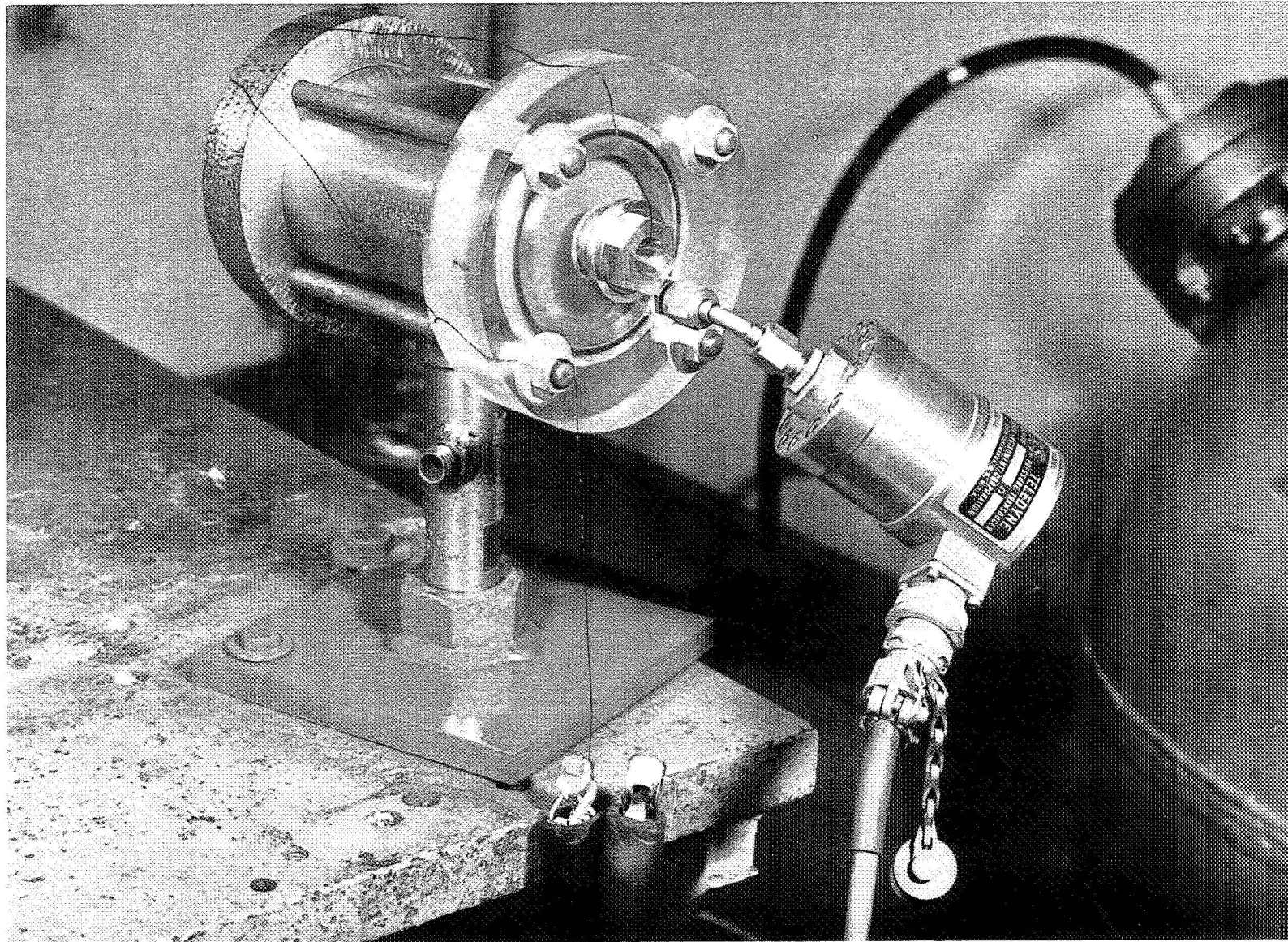
Fig.3.2 The L*-Motor

in parallel with the oscillograph to obtain a time-compressed display of the pressure history.

Early in the program, the need was recognized for visually observing the motor during a firing. Visual observation of the exhaust provides the least misleading indication of the termination of a run. Such information is necessary for stopping the recording instruments. A closed-circuit TV was used for this purpose. The overall view of the firing instrumentation is shown in fig. 3.4, which was photographed during a live firing.

Fig. 3.3 "Test" and "Fire" Circuitry in the Console
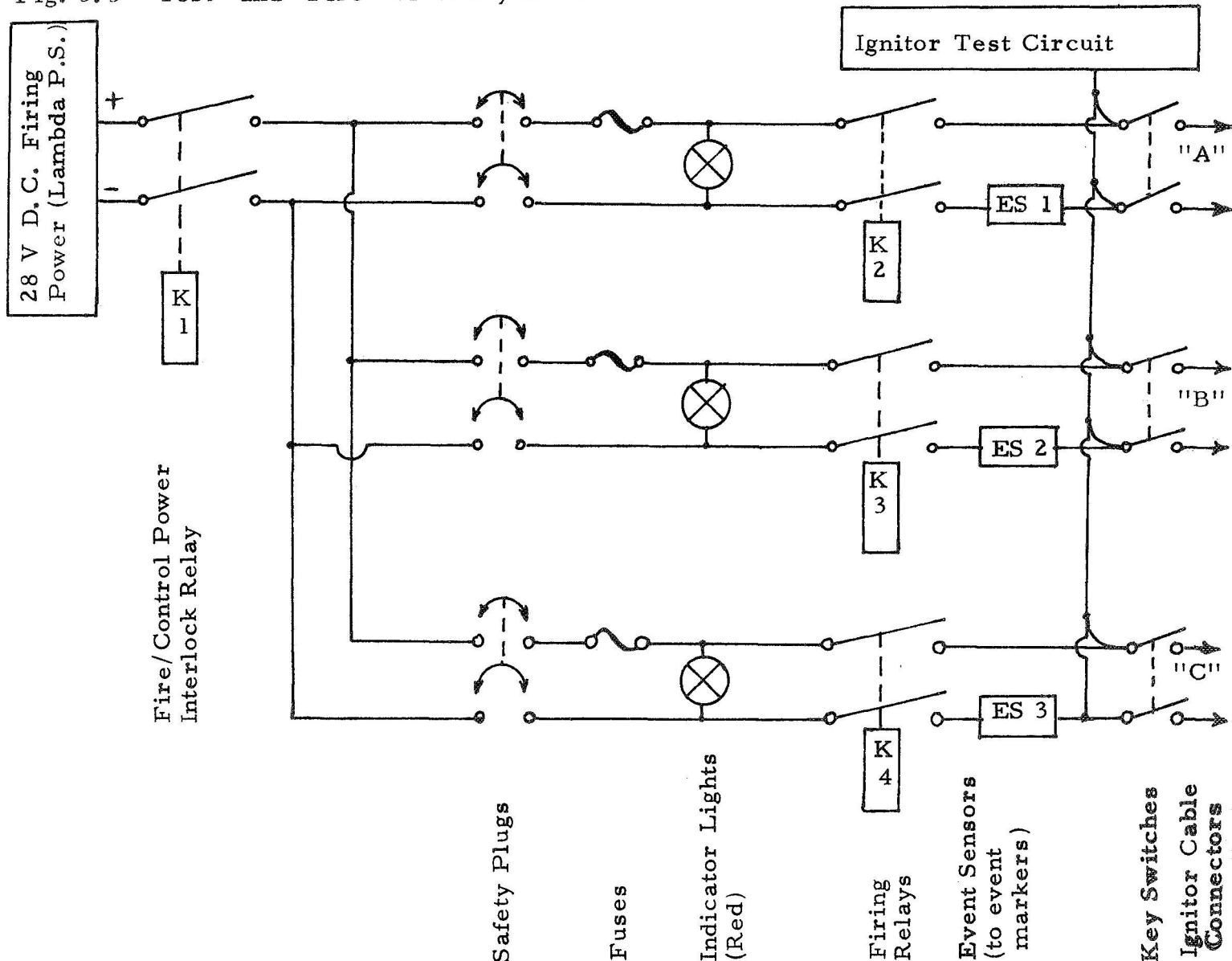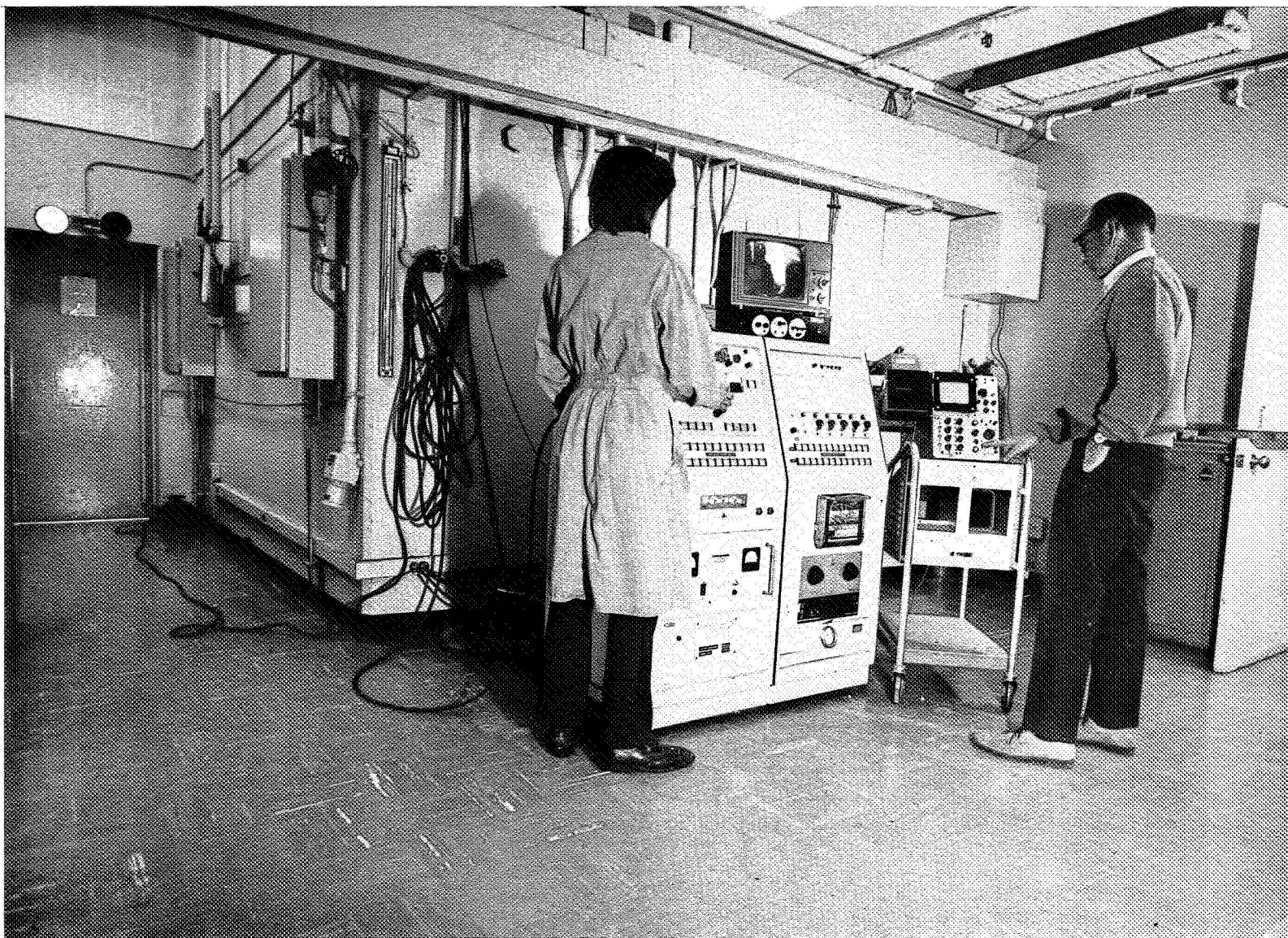
Fig. 3.4   A   Test   in progress

IV. TEST PROCEDURE

In this chapter we describe the details of mounting the propellant, selection of operating conditions, and ignition. Some of these details have a profound influence on the data obtained and also on the interpretation of data.

4.1 Propellant Mounting

The propellant discs were invariably bonded to the stainless-steel piston (P, fig. 3.1) with the EPON resin (five parts of Shell 828 resin with one part of curing agent D). The bond received cure for $2\frac{1}{2}$ hours in an oven maintained around $140^\circ F$. Thus, the propellants received a cure of $2\frac{1}{2}$ hours in excess of their 160-hour cure following casting. A few of the runs during the early part of this program had the propellant edges inhibited with the same EPON resin. The procedure proved to be both unsatisfactory and unnecessary. The tolerances in the machining of the combustion chamber C (fig. 3.1) are such that even the thin ($\approx 0.01''$) layer of hard resin on the edge of the propellant prevented the easy assembling of the motor. Secondly, the edge of the propellant is so close to the cold wall of the chamber that no combustion over the edge seems plausible. Lastly, no experimental evidence indicated that edge burning (i.e., radial regression of the propellant) was significant even when the edge was not inhibited. Several of the tests got terminated before the propellant was fully consumed during a firing, and a scrutiny of the semi-consumed propellant gave no visible evidence of radial regression.

4.2 Experimental Variables

The two primary variables are the nozzle throat diameter (D^*) and the chamber free volume (V_c). The D^* sets the chamber pressure during

time-independent burning of any given propellant for a specific burning area.
The chamber free volume, for a given D^*, sets the motor characteristic
length (L^*) by the very definition

$$L^* = \frac{\text{Chamber Free Volume } (V_c)}{\text{Nozzle Throat Area } (\pi D^{*2}/4)} \quad .$$

The pressure-time history of a run is strongly influenced by these
two variables D^* and L^*. Indeed, the very character of the rocket firing
changes, almost dramatically, depending on changes in D^* and L^*. For
convenience, we use the variable P_c (mean chamber pressure) to signify
variations in inverse D^*, being fully aware of the fact that such a usage is
strictly justified only during steady burning of the propellant. In order to
have a clear feel for the overall behavior, fig. 4. 1 has been composed from
actual test records obtained on the storage oscilloscope. At low values of
L^* and P_c, pressure spikes are seen (fig. 4. 1a). The motor is said to be
chuffing. At high values of L^* and P_c, time-independent burning is observed
(fig. 4. 1c). This mode is characterized by an almost constant mean value of
the chamber pressure that varies only randomly at the intrinsic "noise level"
characteristic of the propellant.

At intermediate values of L^* and P_c, regular pressure oscillations
are observed around a mean value (fig. 4. 1b). These are the bulk-mode or
Helmholtz oscillations in the chamber. If we expand the pressure record in
time, almost sinusoidal oscillations are revealed. (It would appear that in
the literature the term "L^* instability" is frequently reserved exclusively
for these Helmholtz oscillations.) These are the three fundamentally differ-
ent pressure signatures obtained in an L^*-burner. As a slight variation, we
often see the "pressure burst" phenomenon, where the rapidly growing Helm-
holtz oscillations are abruptly terminated on reaching a sufficiently high

L. # 101   10ᵗʰ July 1972* — a

low L*, low P   CHUFF   —— t→

L # 170   1ˢᵗ SEPT 1972* — b

med. L*, med.P   HELMHOLTZ   —— t→

L #107   18 July 72* — c

high L*, high P   STEADY   —— t→

23ʳᵈ March 1972   L # 31* — d

—— t→

L #42   14 April 72* — e

Ignition Influence?   —— t →
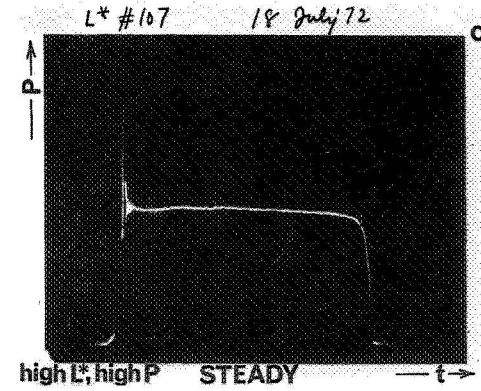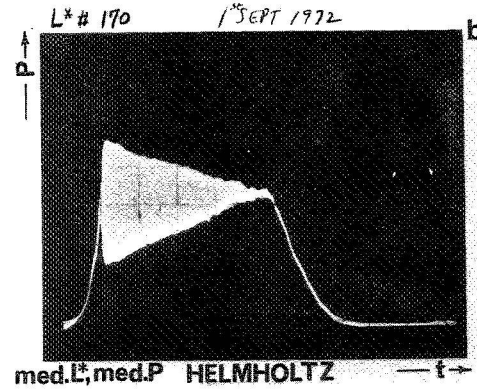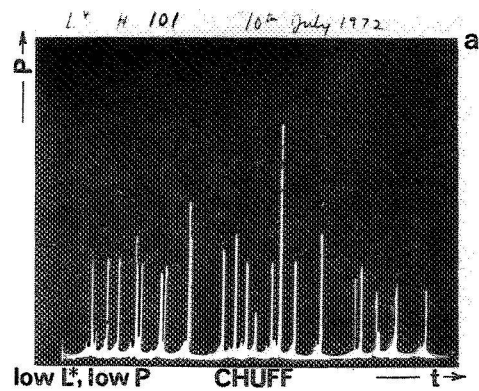
1. The pressure-time history in a rocket motor depends on the propellant, chamber volume, and the nozzle throat size.

2. For a set mean pressure (determined by the nozzle throat size), the important geometrical parameter is

$$L^* \equiv \frac{\text{chamber volume}}{\text{throat area}}$$

3. Pressure traces, such as the ones shown in the first three figures here, enable us to determine the stability boundary of the propellant on the L* vs. pressure plot.
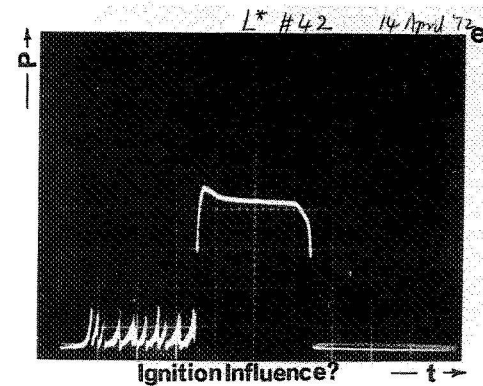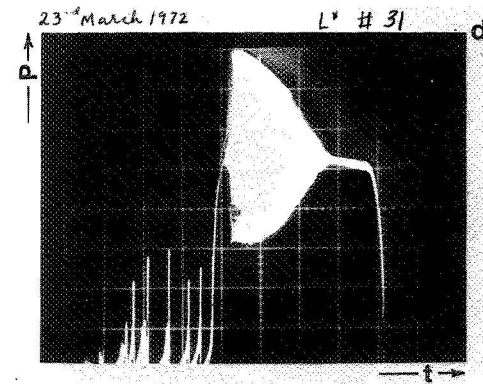
4. Great economy in the number of rocket firings is achieved by having all of the three different modes of combustion (Chuff, Helmholtz, and Steady) in a SINGLE firing.

5. Such a combined firing is achieved by adjusting the initial propellant volume so as to vary the chamber volume over the range of interest through the depleting propellant volume.

6. A few of the runs have hinted at the possibility of nonlinear nature of the Helmholtz mode, which may require a large pulse for its initiation.

Fig. 4.1

amplitude, resulting in a depressurization extinguishment, following which the chamber pressure falls to zero. Representative run records of this phenomenon are shown in fig. 4.2. It is to the various possible combinations of these simple-looking pressure traces that the L^* instability research owes its continuing fascination.

In order to understand the L^* instability behavior as fully as possible it was desired to vary the two primary variables (L^* and P_c) over as wide a range as feasible. Presumably, at any value of P_c, the L^* value would be varied over the range that takes the motor from chuff mode (low L^*) through Helmholtz mode (medium L^*) to steady mode (high L^*). In order to do this, the chamber free volume has to be varied from a low value to a high value for any given P_c. Such a variation is possible during a single firing, when one recognizes that the chamber free volume is increasing <u>during</u> a run because of the depleting propellant volume. The initial propellant volume and chamber free volume are adjusted such that the three fundamentally different modes of motor operation are encountered in a single firing. The actual values to be used in testing a propellant have to be arrived at after one or two exploratory runs. However, an actual test lasts a <u>maximum</u> period of 30 seconds (a majority of them between 5 and 10 seconds), while the preparation for a test lasts approximately 30 minutes in addition to the $2\frac{1}{2}$ hours cure time for the bond. Thus, great economy in testing can be achieved by covering the full range of L^*'s of interest in a single firing. If we had aimed for discrete L^*'s, approximately 6 - 10 runs would have been necessary to determine with reasonable accuracy, the boundaries between chuff, Helmholtz, and steady burning (fig. 4.3, line A).

With the present program, a single firing (fig. 4.3, line B) covers the L^* range of interest; a typical firing is shown in fig. 4.1d. We thus

(a) CIT-2 Propellant   Run No. 34   ◄—Time (t)—

(b) $\widetilde{A}$-13 Propellant   Run No. 155   ◄—Time (t)—

(c) CIT-3 Propellant   Run No. 71   ◄—Time (t)—

(d) CIT-4 Propellant   Run No. 173   ◄—Time (t)—
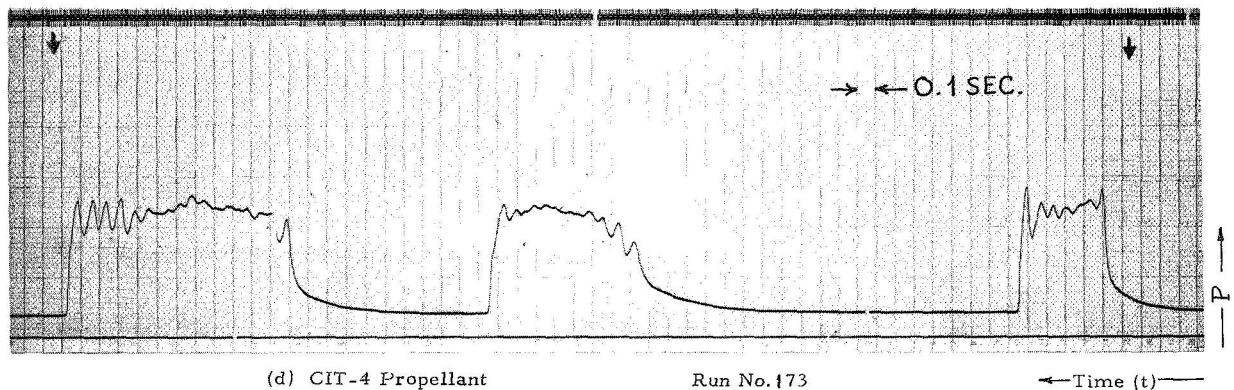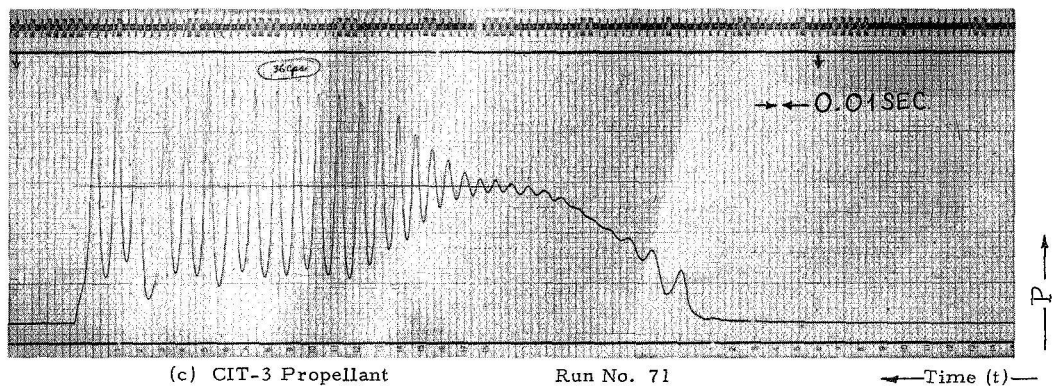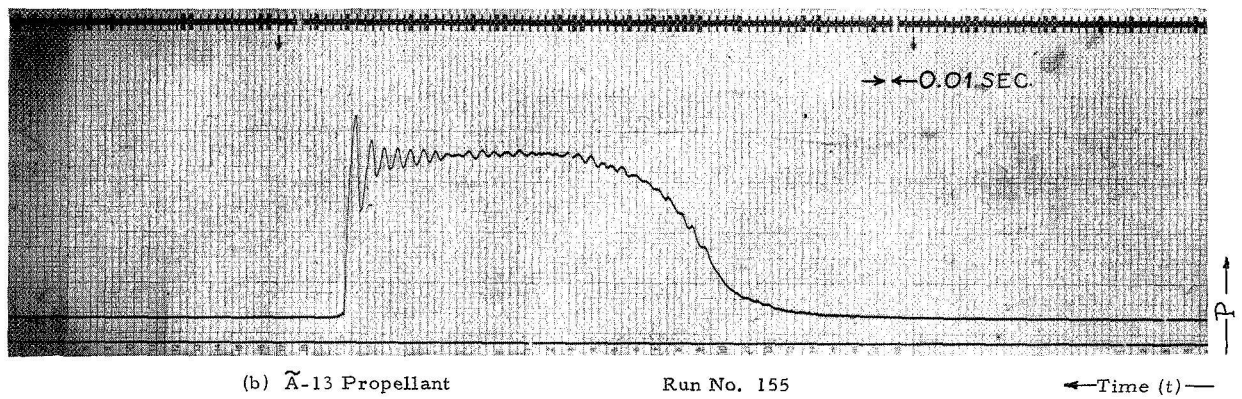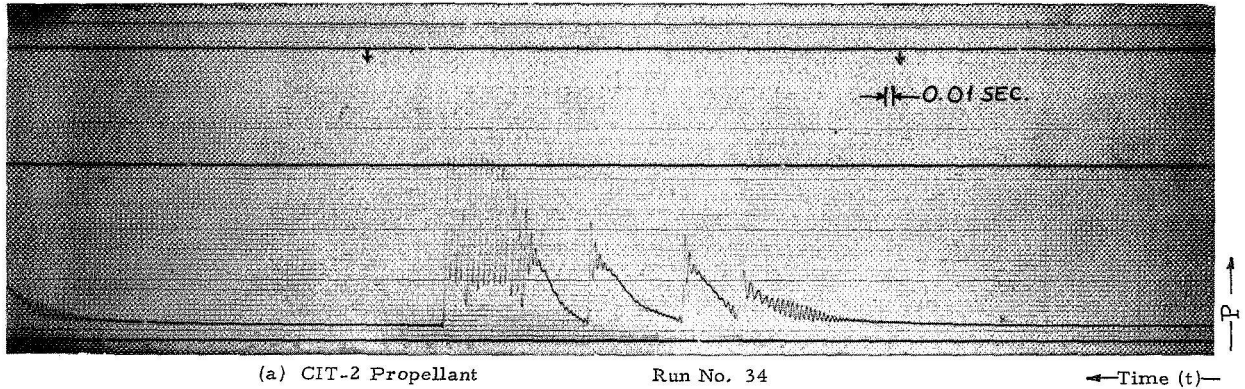
Fig. 4.2 Typical Signatures of the Four Propellants in the Depressurization Rate $(\frac{dP}{dt})$ Extinguishment Mode
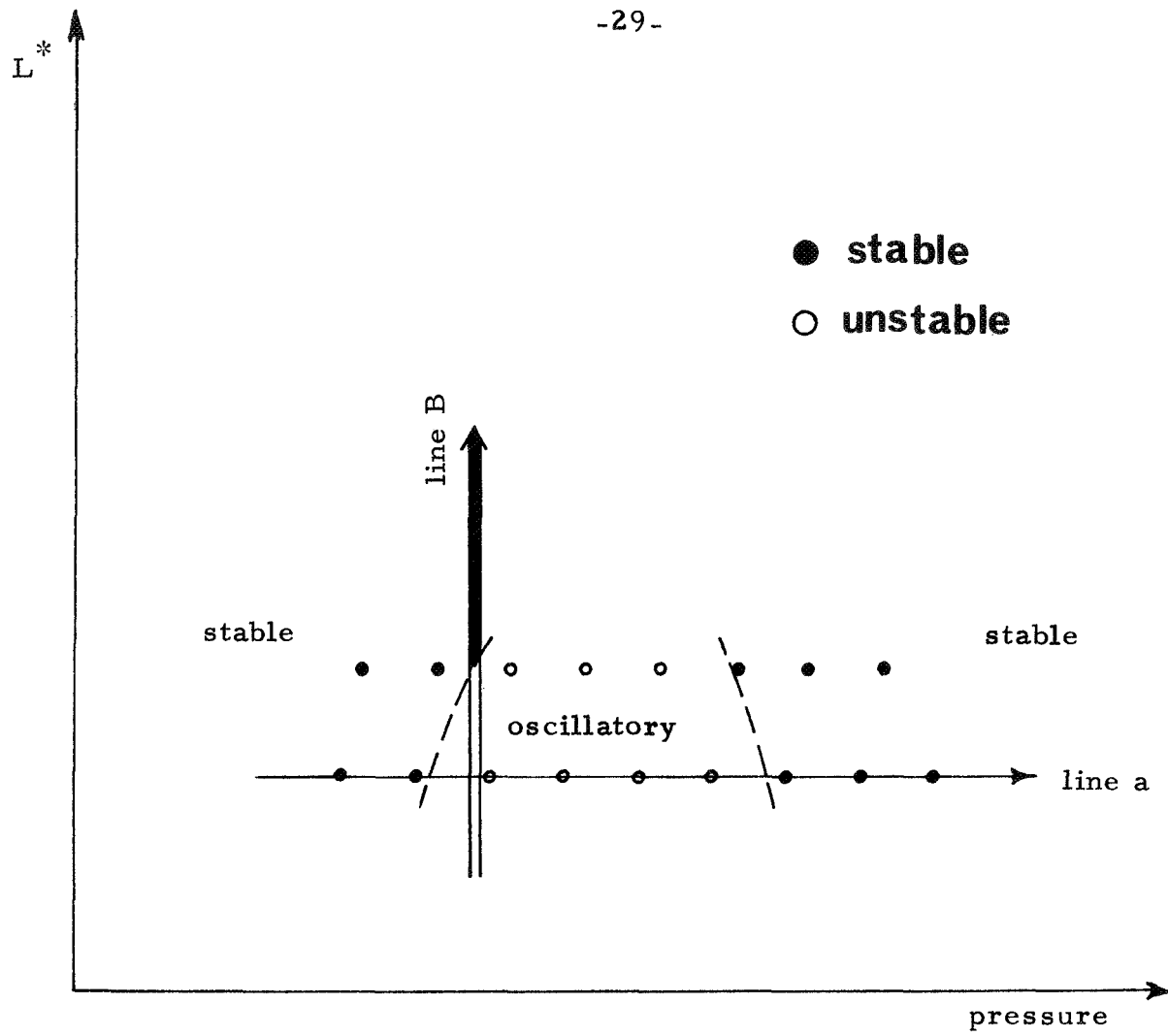
Fig. 4.3 METHODS OF OBTAINING THE STABILITY MAP OF A PROPEL-
LANT.

obtain very accurate stability boundaries through these continuous variations.
It was the realization of the possibility of this method of testing that resulted
in obtaining the stability boundaries for all four of the propellants (along with
the associated data, such as amplitudes and frequencies for all of the pro-
pellants) in as few as a little under two hundred test firings.

4.3 Ignition

During the course of these investigations, some interesting details
of propellant ignition were revealed. Also, the widely recognized importance
of ignition to rocket motor operation was confirmed.

The objective of ignition is to start the combustion of the propellant
in a uniform manner all over the propellant surface simultaneously. In the
selection of the actual ignition procedure, an earlier work at JPL provided
valuable guidance. Different methods of propellant ignition had been com-
pared in T-burner firings, and a method that proved to yield consistently
good results used a centrally-located ignitor pellet over the propellant sur-
face coated with a layer of the ignitor paste. The central pellet, upon igni-
tion (through electrical heating of a nichrome wire located at the core of the
pellet), sprays hot particles symmetrically over the layer of ignitor paste on
the surface of the propellant, and ignition is initiated, fairly symmetrically,
at several different spots. This results in a rapid and uniform ignition of
the propellant.

Two different ignitor pastes were used in the present experiments.
One of them, generously supplied by the Naval Weapons Center, goes by the
name of X-225 and has the following composition: polyisobutylene, 6.0 wt.
percent; boron powder, 6.9 wt. percent; titanium powder, 14.8 wt. percent;
potassium perchlorate, 72.3 wt. percent. The other ignitor paste, formulated
at JPL, is named CIT IP 1 and has the following composition: polyisobutylene,

7.0 wt. percent; boron powder, 6.0 wt. percent; aluminum powder, 14.0 wt. percent; and ammonium perchlorate 73.0 wt. percent.

CIT IP 1 was originally intended as a substitute for the NWC X-225, but revealed such poor mechanical and handling characteristics compared to X-225 that it was discarded in favor of the latter. However, as the experiments progressed, CIT IP 1 proved invaluable for the ignition of the propellants with coarser oxidizer particles. It must be recalled that the burning rates of the propellants decrease in the order of increasing coarseness of oxidizer particles (fig. 2.7). The X-225 ignitor paste, while very successful in the ignition of CIT-2 propellant (11μ AP particles) and also successful in the ignition of the $\widetilde{A}$-13 propellant (39.5μ AP particles), burned too fast for the CIT-3 (175μ AP particles) and CIT-4 (350μ AP particles) propellants. That is, upon ignition of the central pellet, the layer of X-225 on the surface of the propellant burned out quickly, while the propellant never had sufficient time for ignition. The need was felt for a slower-burning ignitor paste. The readily available CIT IP 1 was employed for coating the propellant surface after recognizing that aluminum is slow burning at the low pressures encountered. This choice proved highly successful and, in fact, made all the difference between our ability and inability to get the CIT-3 and CIT-4 propellants to ignite at low chamber pressures[*].

Thus, the thought emerged that for satisfactory ignition of propellants, we need an ignitor paste, the characteristic combustion time of which is not too different from the characteristic combustion time of the propellant itself. This empirical information, obtained during the present program, has proved

---

[*]Exposure of fresh oxidizer particles in the propellant, through a mild abrasion of the propellant surface, before applying the coat of ignitor paste, proved helpful at times.

very useful so far.

Except for the choice of the surface layer of ignitor paste as noted above, an attempt was made to maintain a standard ignition technique in all of the firings. The thickness of the surface layer could have varied (around 0.01 inch) from run to run, but not by much. Also, the size of the central ignitor pellet was varied a little in order to obtain satisfactory performance as dictated by experience. As a general rule, smaller pellets were needed for smaller volumes of the combustion chamber. This is probably due to a depressurization rate effect. The gas produced upon ignition of the ignitor paste has to vent through the nozzle. The venting process produces a (dp/dt) transient in the combustion chamber that could become severe enough to extinguish the propellant (if it is already lit). A smaller pellet, producing less gas, results in a smaller (dp/dt) transient for a given chamber condition, and the propellant could remain lighted during such a transient.

The most interesting result of the variation in the pellet size was the complete suppression of the Helmholtz mode oscillations on occasions. The motor went from the chuff mode at low L^* values into the steady mode at high L^* values through the steady mode at intermediate L^* values, instead of through the Helmholtz mode. This difference is strikingly displayed in figs. 4.1d and e. It would appear that even when the conditions in the motor are suitable for Helmholtz oscillations, a large amplitude disturbance (such as available during the final stages of a violent chuff mode) may be necessary for exciting the Helmholtz mode oscillations. The implications of such a non-linear behavior are not clearly understood. As a matter of fact, the very phenomenon was found not to be readily reproducible. It depends presumably on small, as yet obscure, details of chamber conditions. More research is needed to shed light on the situation. The importance of such research is

readily appreciated when one recognizes the possibility of totally suppressing chamber pressure oscillations.

It is noted in passing that a careful record has been maintained of the precise details of the ignition technique used in every one of the firings, so that any future study pertaining to correlations of test results with the ignition technique has available the data to work from.

4.4 Volume Measurement

After a test was over (even if the propellant was not fully consumed during the run) the chamber volume was measured by filling the chamber with water from a graduated jar. Throughout the present report, the combustion chamber volume (V_c) is implied to signify the free volume of the chamber up to the throat of the nozzle. The error in the volume measurement is estimated to be within ± 0.5 cc. The measured volumes ranged from 20 cc. to 200 cc.

V. STUDIES IN A TRANSPARENT MOTOR

In this chapter, some visual observations in the L-star motor are described. The observations helped to clarify certain features of L^* instability. The observations clearly showed the ignition sequence, luminosity variations during Helmholtz instability, and the complicated nature of the chuff-mode combustion.

Our understanding of a physical phenomenon is usually in terms of a model for the constituent processes behind the phenomenon. Based on such a model, an attempt is made (either through theoretical analyses or through physical reasoning) to predict the observations concerning the phenomenon. If the predictions are consistent with the observations, the postulated model is assumed to be sufficiently representative of the phenomenon. Generalizations from such a model may then be attempted. If the model yields results that are inconsistent with observations, new models are postulated until a better agreement is obtained. It is when our understanding is at such a level of uncertainty that a direct experimental observation of the phenomenon can prove to be very valuable.

In more concrete terms, let us examine the classical problem of rocket motor pressure-time history. A simple one-dimensional linear regression rate of the propellant is assumed according to de Saint-Robert's law $(r = aP^n)$. The mass discharge rate from the choked nozzle is equated to the mass regression rate of the propellant. The equality determines the chamber pressure which is predicted to be practically constant during a run for a constant burning area. When it is experimentally observed that the pressure-time trace does indeed show a near-constant value, it is concluded that the model of one-dimensional combustion is sufficiently accurate, at

least for the calculation of pressure-time histories.

Generalizing the above thoughts to the pressure-time trace obtained during the Helmholtz oscillations, we can visualize the same one-dimensional combustion giving rise to the pressure trace observed. We recall that the frequencies encountered in the Helmholtz mode are of the order of 100 Hz (30 - 60 Hz, more often). Typical characteristic times for the vapor phase combustion processes above the propellant are like the ratio of the "flame" standoff distance to the mean velocity of the gases. Employing typical numbers we arrive at $(200\,\mu \div 20 \text{ cm. sec}) \sim 10^{-3}$ sec for the characteristic time. Since the characteristic time for the pressure oscillations is much longer than the characteristic time associated with the combustion processes, the model applicable during time-independent combustion may be expected to be valid during the Helmholtz-mode instability also.

Now let us examine the chuff mode. Both the sharp pressure spikes and the periods of no apparent activity in the chamber (reflected in the near-zero pressure levels) are difficult to interpret in terms of a simple one-dimensional picture used earlier. Near-zero pressures could be caused by several different phenomena. For example,

(i) propellant extinction,

(ii) extremely low regression rates of the propellant for some unknown reason,

(iii) combustion over only a small fraction of the propellant surface, again for some unknown reason.

It is readily appreciated that the number of such speculative possibilities is very large. Rather than carry out an analysis for each of the possible cases and compare the predictions with observations, a direct visual

observation was attempted. The attempt was preceded by the observation of a propellant charge that had been extinguished during a severe chuff mode. As shown in fig. 5.1, the extinguished propellant clearly reveals remarkable surface distortions in comparison with the plane surface of an unfired propellant. The surface unevenness is seen to be nearly ten times the magnitude of the characteristic length scales associated with propellant combustion ("flame" standoff distance, effective thermal depth in the solid, etc.) during time-independent combustion, which are approximately $\sim 100 \mu$. Without revealing the details of the processes during the chuff mode, fig. 5.1 clearly shows that the one-dimensional model is of doubtful validity during chuffing.

5.1 The Experimental Setup

A transparent nozzle end plate was machined from a one-inch thick block of plexiglas. The very low cost of the material, together with easy machineability, led to the choice of plexiglas. It was recognized that the poor heat resistance characteristics of the material may obscure the details inside the chamber during the visual observations. However, cost considerations ruled out the possibility of quartz windows and inert gas purge over the wall. Besides, the deterioration in the transparency of the plexiglas end plate was not expected to commence until after the heavy flow of combustion gases over it. Thus, the details, at least during ignition and the initial stages of a chuff, were anticipated to be seen clearly. Later observations revealed not only the limited details anticipated, but extensive details of the chuff mode as well, for reasons that should be obvious shortly.

The assembled L-star burner with the plexiglas end plate was shown in fig. 3.2. A Hycam Model 400 motion picture camera was stationed with its lens approximately three feet away from the nozzle end plate. Motion

Fig. 5.1 SURFACE DISTORTIONS SEEN AFTER A (dP/dt) EXTINGUISHMENT.
Run no. 36, Propellant CIT-2. The extinguished propellant surface is compared with an
unfired propellant at the right. A <u>large</u> ignitor pellet is also shown.

pictures were taken on Kodak Ektrachrome films of two separate firings. The first one (run no. 32) exhibited strong Helmholtz oscillations but no chuffing; the pictures were taken at 4000 frames per second. The second firing (run no. 33) exhibited several chuffs before entering the time-independent combustion mode. No Helmholtz oscillations were observed; the motion pictures were taken at 3000 frames per second. The originals of the processed films are with Section 381 at the Jet Propulsion Laboratory. Several prints taken from the movie frames, and presented in this report, are described below.

5.2 The Helmholtz Mode

The Helmholtz oscillations were revealed as cyclic luminosity variations in the movie. One complete cycle is presented in fig. 5.2. To orient the reader with respect to the movie camera, it is observed that the movies are taken from exactly the same relative position from which fig. 3.2 was taken.

The ignitor leads (31 gage copper wires) are seen on the left of the nozzle in all of the frames. Another feature common to all of the frames in fig. 5.2 is the inhomogeneous appearance of luminosity. The origin of this "patchy" appearance is the non-uniform erosion of the plexiglas on the inside surface. The invariable spatial variations during ignition (when the hot particles emanate from the central pellet) are believed to be among the prime causes of the asymmetric erosion pattern of the plexiglas. (Minor variations in the thickness of the silicone grease on the inside surface could be another factor.) The point of these observations is that the inhomogeneous luminosity pattern seen in the frames is due to the plexiglas erosion pattern and not due to inhomogeneous luminosity inside the chamber. This fact can be appreciated by following the entire sequence of events (beginning with ignition) in the movie.

.002 sec

.004 sec

.001 sec

.003 sec

TIME

0 sec
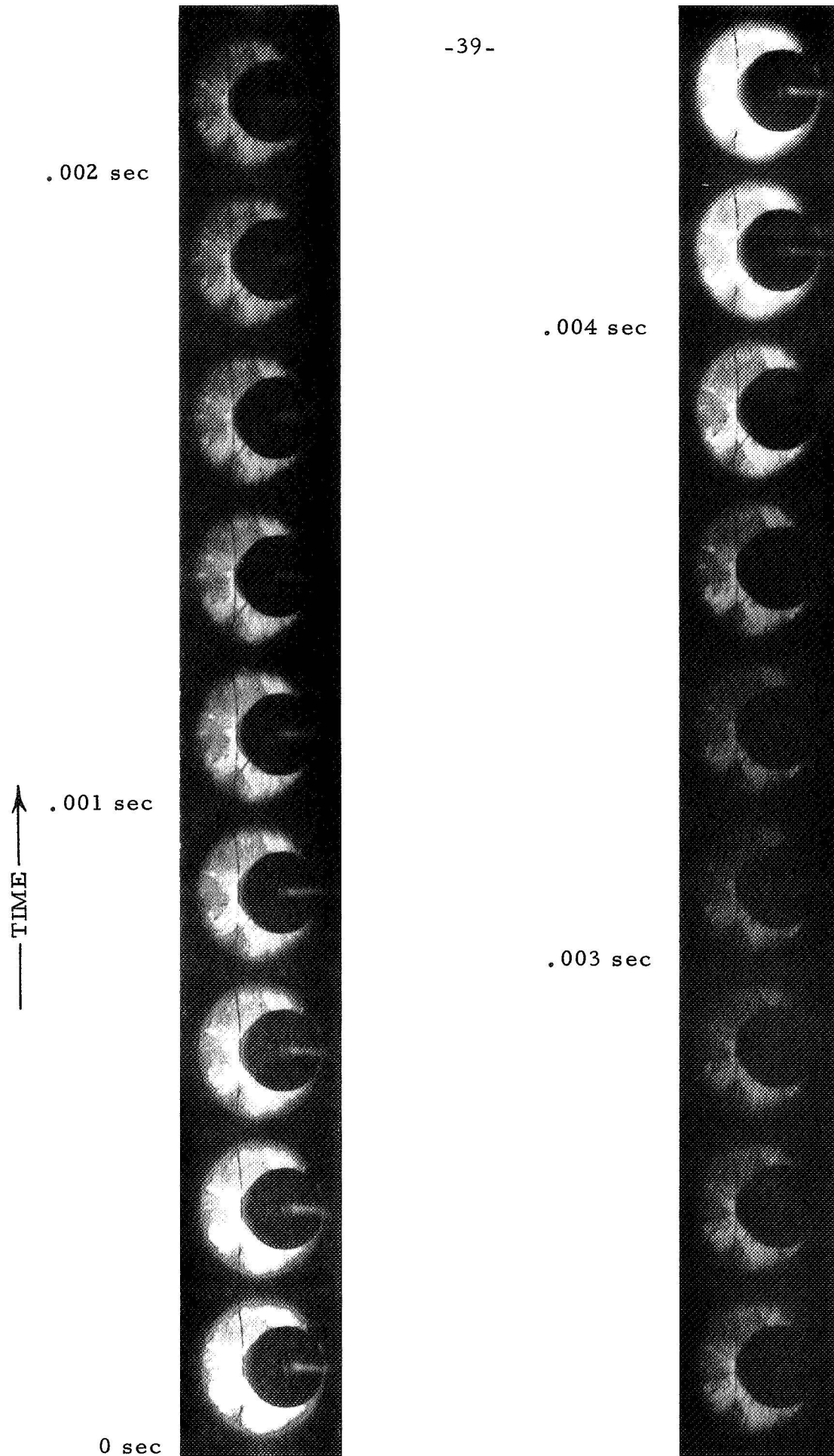
Fig. 5.2 THE HELMHOLTZ MODE (Run no. 32, Propellant CIT-2).

To appreciate this fact in fig. 5.2, it is suggested that some specific spot (spatial location) be followed from frame to frame. It is seen that only the light intensity varies and not the general pattern around such a spot. The lack of spatial variations inside the chamber is taken to signify the one-dimensional nature of combustion during the Helmholtz oscillations. Thus, the earlier conjecture based on order-of-magnitude estimates of time scales during Helmholtz-mode oscillations is supported by visual observations. An interesting feature seen both in the movie and in fig. 5.2 is that the luminosity variations do not possess symmetrical growth and decay patterns. While the growth needs approximately one millisecond (4 frames), the decay is spread over approximately three milliseconds (12 frames). The pressure oscillations recorded on the oscillograph at a paper speed of sixteen inches per second indicate that the waveform is apparently symmetrical. However, one of the tests (Run No. 39) on the CIT-2 propellant had its data recorded at sixty-four inches per second, which reveals the actual waveform with much greater clarity. As seen in fig. 5.2(b), the pressure oscillations are indeed asymmetrical and conform rather closely to the luminosity oscillations. The asymmetrical oscillations are among the several exclusive features observed with the CIT-2 propellant as discussed in Chapter VIII. The other three propellants reveal nearly symmetrical oscillations as may be seen in figs. 4.2 (b), (c), and (d) and 6.2 (a) and (b).

Because of the qualitative nature of these studies, no measurements of luminosity variations were attempted. However, we recognize that it is a simple matter to run the movie before a photocell and obtain the quantitative luminosity pattern that existed during the firing.

5.3 The Chuff Mode

The chuff mode was revealed as high-activity periods, isolated in time, superposed on a general background of very low activity in the chamber.
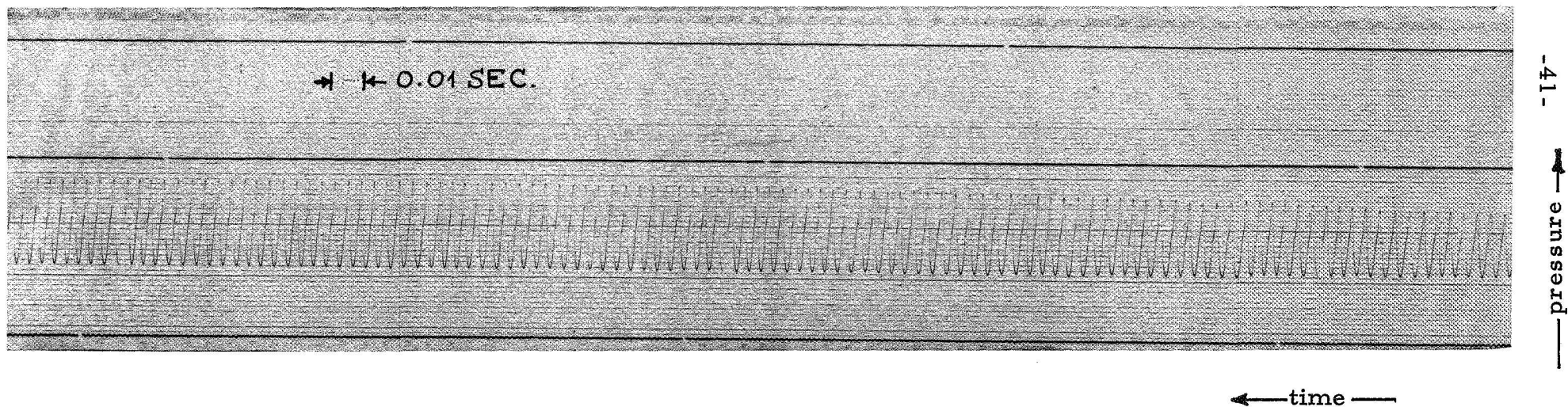
Fig. 5.2(b).   Extended-time Pressure History of the CIT-2 Propellant.   Asymmetric Waveform Is Evident.   Run No. 39.

Such a picture was fairly evident from the earlier pressure traces. But what was not evident from the pressure traces was the nature of the low-activity background in the chamber, which was clarified by the movie photographs.

During most of the ignition sequence, very little difference was found between this run (no. 33) and the one that exhibited Helmholtz instability (no. 32). However, towards the end of the ignition sequence, it was observed in the motion pictures that no luminous area (the "flame") covered the surface of the propellant, in contrast with the earlier run. Isolated bright spots were seen and these were identified as the hot metal particles from the ignitor paste. (It is to be remembered that the propellant itself is non-metallized.) Following the actual sequence of events, surface distortions of the propellant became perceptible. Isolated regions of subdued brightness (nowhere near the brightness of a full flame over the surface) were seen. The bright metal particles were seen to circulate slowly around the circumference of the chamber, possibly signifying the existence of mild eddying motion of vapors inside the chamber.

If relative motion occurred between the hot metal particles and the surrounding vapors, it must have been in the Stokes/Oseen regime. Occasionally the isolated regions of subdued brightness gave rise to a brighter gas evolution that discharged through the nozzle in a "puff," presumably corresponding to a chuff in the pressure-time trace shortly before the discharge.

All these activities took place in the chamber, with the general background being fairly dark. At no time during the entire sequence of these events was there a heavy evolution of combustion gases uniformly from the propellant surface. The lack of erosive flow of hot gases over the plexiglas nozzle end plate, kept the plate fairly transparent all through these events and afforded a

visibility that was better than expected.

Even when the propellant was not burning in the normal manner, evolution of vapors from the propellant surface was evident in isolated areas. This mass loss, even in the absence of steady burning, can introduce large discrepancies between the regression rate calculated on the basis of total chuff duration and propellant thickness variation, and the regression rate measured in a bomb. The increasing chamber volume (due to the depletion of the propellant volume), and hence the increasing L-star, finally placed the propellant in the steady-burning mode, after which event, fig. 5.3a was obtained. This photograph is to be compared with those obtained during the Helmholtz mode in the previous run (fig. 5.2). The point is to note the general uniformity in luminosity inside the chamber, although the view is a little obscured due to plexiglas erosion (already discussed).

During the initial stages of ignition, fig. 5.3b was obtained. As well as can be judged, the bright metal particles are seen with as much clarity inside the chamber as outside the chamber, indicating that the plexiglas plate has not yet suffered erosion. Figures 5.3 c, d, and e were obtained during various stages of the chuff mode operation. It is readily appreciated that there does not exist a uniform combustion zone over the propellant surface. The isolated regions of activity are also seen. These frames were specially chosen to reveal the "puff" of hot gases leaving the nozzle. This is to be compared with the supersonic exhaust (which results in a visible shock after nozzle exit) during normal combustion in fig. 5.3a. In comparison with the prints in fig. 5.3, we note that the details of surface distortion are far more clear in the original movie. Nevertheless, the prints should indicate the general features described earlier.
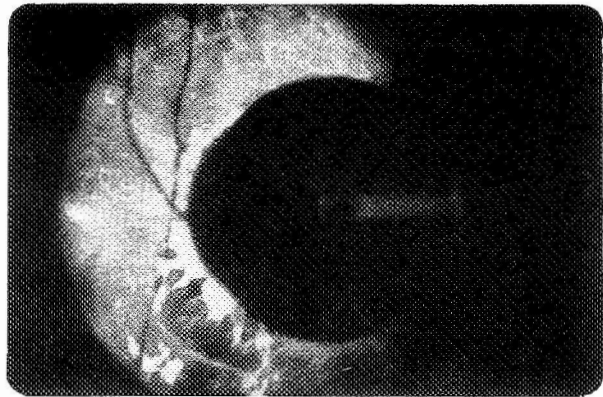
(a)

Time-independent combustion. Uniform
glow. Choked nozzle.
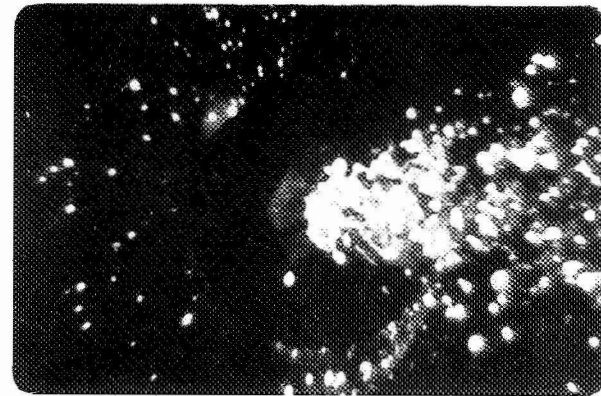
(b)

Early stages of ignition. Spray of hot
metal particles from the ignitor paste.
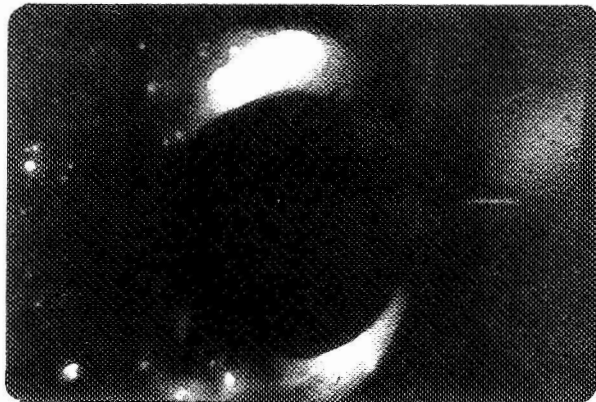
(c)
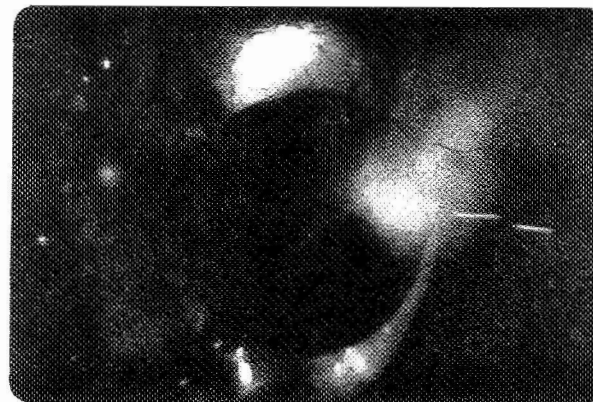
(d)

(e)

The chuffing operation. Isolated regions of subdued brightness. Distortion of propellant surface. Slow circulation of
hot metal particles. Occasional "puffs" of gas exhaust. Unchoked nozzle.

Fig. 5.3 DETAILS OF A RUN WITH CHUFF-MODE (Run No. 33; 3000 frames per second).

Based on these observations, an overall description of the chuff-mode operation is attempted as follows. For some poorly understood reason, the $L^* - D^*$ combination places the propellant in a regime where non-uniform combustion over the surface is possible. The local heating of the propellant causes both severe mechanical distortions and evolution of vapors locally. If these vapors happen to have available an ignition source, such as a hot metal particle from the ignitor paste, local combustion of this mass of vapors gives a momentary surge of pressure in the chamber. A rapid depressurization follows the exhaust of this mass of burned gas. The observation that the combustion of this mass of gas does not initiate the familiar "flame" uniformly over the propellant surface, until after the L^* has increased to a sufficiently large value, needs further study.

One fact that emerges unmistakably from these studies is that combustion near the propellant surface during the chuff mode operation is far from being one-dimensional or steady. Any realistic analysis of the chuff mode will have to incorporate these essential features. Another aspect is the possible contamination of the chamber gases with ambient air due to the very low flow rate of propellant vapors (burned or unburned) through the nozzle from the chamber. This feature is obviously absent during choked flow observed when the propellant is burning normally.

Two tests on the propellant CI T-2, conducted under practically identical conditions of L^* and D^* need special mention. In run no. 37, a very thin layer of ignitor paste was applied over the propellant surface and a small ignitor pellet was employed. The ignition variables were chosen so as to create as small a pressure disturbance as possible and were naturally conducive to poor ignition of the propellant surface. From the foregoing descrip-

tion of the chuff-mode operation, we might expect that the poor ignition would result in chuffs, if the $L^* - D^*$ combination permits them. In the oscilloscope trace obtained during the run (fig. 5.4a), chuffs are visible as anticipated, and also no Helmholtz mode is evident.

Run no. 38 employed a thick layer of ignitor paste over the propellant surface and also a very large ignitor pellet. The ignition variables here were chosen so as to give as uniform an ignition as possible, and were naturally conducive to the occurrence of large pressure disturbances in the chamber. As seen in the oscilloscope trace presented in fig. 5.4b, the chuff mode was totally eliminated, but the Helmholtz mode got initiated.

While these observations support both the postulated influence of ignition on the chuff mode and the nonlinear nature of the Helmholtz mode, quantitative correlations are very difficult. Quantitative correlations form the basis of a theory, and also enable us to usefully employ these observations in an actual rocket motor, at least in an empirical manner.

Fig. 5.4 INFLUENCE OF IGNITION DETAIL ON L-STAR INSTABILITY
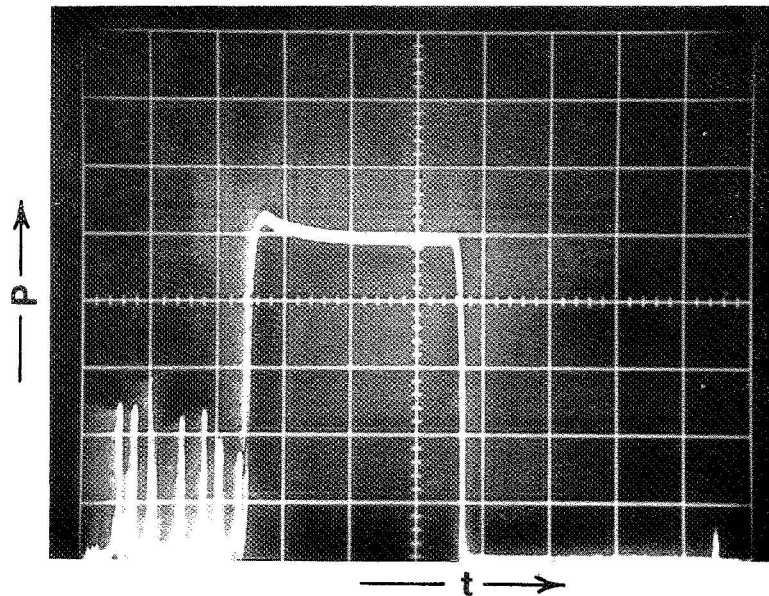
(a) Run No. 37
    Propellant: CIT-2
    Volume at burnout: 58 cc
    L^* at burnout: 89.2 cm
    Ignition: a thin layer of ignitor paste
               over the surface; a small
               pellet of ignitor paste at
               the center.
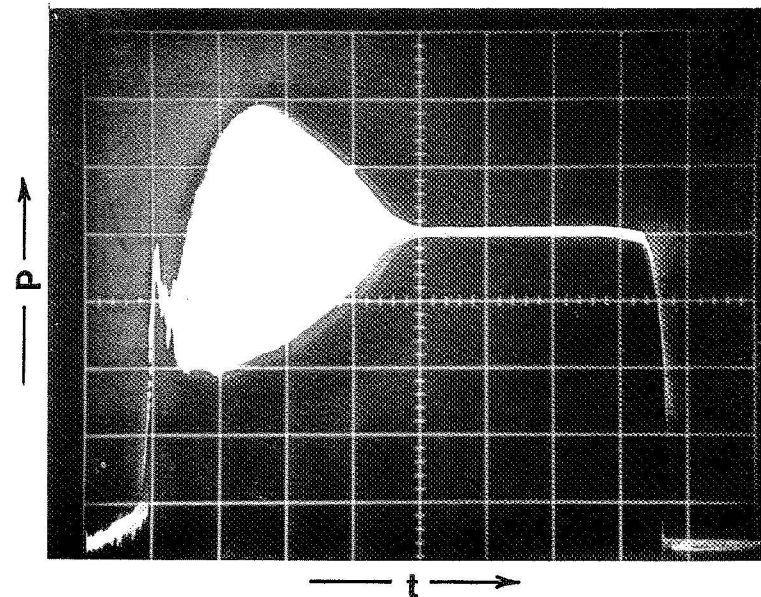
(b) Run No. 39
    Propellant: CIT-2
    Volume at burnout: 56 cc
    L^* at burnout: 86.1 cm
    Ignition: a thick layer of ignitor paste
               over the surface; a large
               pellet of ignitor paste at the
               center.

[Oscilloscope sweep speeds were not the same in (a) and (b).]

TABLE 5.1 Experimental Results of the CIT-2 Propellant

Date	Run No.	D^* inch	$\bar{P}$ psia	$\bar{r}_{run}$ in/sec	$\bar{r}_{bomb}$ in/sec	L^* cm (beginning)	P' psi	f Hz	L^* cm (middle)	P' psi	f Hz	L^* cm (end), i.e., noise level	P' psi	f Hz
20 Mar 72	19	0.327	46.1	0.107	0.099	24.20	51.60	243	35.30	24.10	264	41.25		
21 Mar 72	22	0.338	42.8	0.103	0.098	33.90	31.50	234	47.30	15.90	262	51.40		
21 Mar 72	23	0.338	42.8	0.107	0.098	34.90	31.50	245	44.20	15.90	268	49.10		
21 Mar 72	24	0.348	39.92	0.092	0.096	37.40	29.0	225	50.90	15.00	258	55.50		
22 Mar 72	25	0.348	40.55	0.0885	0.096	39.95	27.0	240	53.65	13.0	258	58.00		
22 Mar 72	26	0.349	41.80	0.0925	0.097	41.10	24.0	250	53.65	13.0	255	51.40		
22 Mar 72	27	0.349	40.3	0.088	0.096	40.15	29.0	225	53.35	14.0	255	59.00		
23 Mar 72	28	0.349	40.3	0.0915	0.096	41.25	26.0	225	54.95	13.0	258	63.00[+]		
23 Mar 72	29	0.349	40.3	0.0945	0.096	51.30	18.0	250	57.80	8.50	263	61.20		
23 Mar 72	30	0.349	42.8	0.0905	0.098	42.20	23.3	245	46.20	11.60	262	49.20	practically indiscernible	
23 Mar 72	31	0.349	40.3	0.0925	0.096	40.50	24.0	242	49.10	11.60	262	54.20		
11 Apr 72	41	0.358	38.1	0.121	0.095	58.30	13.75	258	61.90	6.3	268	64.10		
17 Mar 72	16	0.312	52.7	chuffs	0.105	15.4	59.2	233.3	19.09	31.95	266.7	21.30		
17 Mar 72	17	0.312	52.1	chuffs	0.104	22.3	55.9	266.7	25.13	39.7	266.7	26.8		

TABLE 5.2 Experimental Results of the $\tilde{A}.13$ Propellant

Date	Run No.	D* inch	$\bar{P}$ psia	$\bar{r}_{run}$ in/sec	$\bar{r}_{bomb}$ in/sec	L* cm	P' psi	f Hz	L* cm	P' psi	f Hz	L* cm	P' psi	f Hz
18 Aug 72	127	0.272	53.1	0.0805	0.078	136	23.9	35.5	140	17.9	37.65	146.5	1.57	42.55
25 Aug 72	147	0.262	67.3	0.0845	0.087	139.7	14.81	41.5	142	11.4	40	145.1	1.56	40
25 Aug 72	149	0.25	76.2	0.1055	0.0925	121	19.65	41	125	10.8	39	131	1.229	41
28 Aug 72	154	0.237	82.85	0.1084	0.096	steady in the L* range covered			82.2 - 156.2 cm				1.5	40
28 Aug 72	155	0.237	92.8	0.148	0.102	68.6	47	56.1	none observed					
28 Aug 72	156	0.237	92.8	0.125 if chuff du- ration is included	0.102	no more oscillations observed						68.6	2.0	52.5
28 Aug 72	157	0.262	67	uncertain because of chuff duration	0.0865	121	11.87	41	122.7	5.55	40	124.9	1.58	42.65
30 Aug 72	160	0.327	28.2	"	0.058	56.65	5.85	71.2	58.85	2.63	71.2	61.9	0.31	72.0
30 Aug 72	161	0.312	32.55	"	0.062	67	19.2	53.4	71	14.17	52.2	77.2	0.59	56
30 Aug 72	163	0.298	38.0	0.07355	0.0665	76	30.4	45.7	99	13.45	41.5	-	-	-
30 Aug 72	164	0.223	111.9	0.1178	0.11	L* = 22.4 cm, P' = 25.15 psi, f = 106.7 Hz								
1 Sept 72	170	0.298	39.1	0.07725	0.0675	72.7	24.2	49.2	103	13.78	40	130	1	35.6

TABLE 5.3 Experimental Results of the CIT-3 Propellant

Date	Run No.	D* inch	$\bar{P}$ psia	$\bar{r}_{run}$ in/sec	$\bar{r}_{bomb}$ in/sec	L* cm (beginning)	P' psi (beginning)	f Hz (beginning)	L* cm (middle)	P' psi (middle)	f Hz (middle)	L* cm (end), i.e., noise level	P' psi (end), i.e., noise level	f Hz (end), i.e., noise level
2 May 72	45	0.312	27.9	C	0.0535	131	15.35	17.8	$(dP/dt)_E$					
4 May 72	46	0.312	29.4	C	0.055	116.5	15.85	21.3	$(dP/dt)_E$					
20 June 72	68	0.272	37.15	0.0755 PNAA	0.0605	57.5	18.36	35.7	64.0	10.95	35.0	70.8	1.562	33
21 June 72	71	0.262	41.05	C	0.063	60.25	36.3	36	$(dP/dt)_E$					
26 June 72	74	0.25	54.3	0.0714	0.071	76.1	29.5	37	82.3	23.6	38.4	98.7	1.24	37.5
26 June 72	75	0.25	50.9	0.069	0.069	74.7	33.9	30.75	88.3	20.2	36.4	102.1	1.505	40
27 June 72	79	0.223	77	C	0.0820	45.7	52	53.4	$(dP/dt)_E$					
6 July 72	90	0.237	61.0	0.0761	0.0745	47.7	47.3	42.1	69.2	36.0	41.7	95.75	1.33	25
6 July 72	92	0.223	76.0	0.083	0.082	39.25	30.0	64	45.2	16.65	64	52.85	1.33	60
7 July 72	97	0.223	73.6	0.0818	0.0805	36.0	25.2	56.5	39.1	16.67	59.25	44.25	1.445	45.75

C appreciable chuff periods

PNAA appreciable periods of no apparent activity

$(dP/dt)_E$ depressurization extinguishment before burnout

-50-

TABLE 5.4 Experimental Results of the CIT-4 Propellant

Date	Run No.	D* inch	$\bar{P}$ psia	$\bar{r}_{run}$ in/sec	$\bar{r}_{bomb}$ in/sec	L* cm	P' psi	f Hz	P' psi noise level	f Hz	General Remarks
31 Aug 72	165	0.223	69.1	0.074	0.0645	33.85/113	steady run				large scale unsteadiness
31 Aug 72	166	0.25				23.2/87.7	steady run		1.49	21.6	
31 Aug 72	167	0.262	34.0	C	0.0475	78.9⁻	6.15	13.3	-	-	
31 Aug 72	168	0.272	31.93	C & TD	0.0465	95.1	7.36	15	0.99	16.66	
1 Sept 72	169	0.272	chuff dominated run			80.5	chuff dominated run				
7 Sept 72	171	0.272	29.57	C & TD	0.045	93.95	11.9	10	≈1.4	16.66	
7 Sept 72	172	0.298	26.95	C & TD	0.0433	63.2⁻	5.15	11.87	-	-	
7 Sept 72	173	0.298	29.10	C & TD	0.0447	97.5⁻	4.15	13.33	0.76	20.0	
8 Sept 72	174	0.298	28.5	C & TD	0.0443	132.1⁻⁻	2.4	11.1	-	-	not sinusoidal at all; very random
12 Sept 72	182	0.198	87.5	0.0696	0.0715	15/116	steady run		-	-	large scale unsteadiness
12 Sept 72	183	0.223	57.55	0.0625	0.0595	11.65/91.4	steady run		-	-	large scale unsteadiness
29 Sept 72	184	0.272	29.53	0.0568	0.045	79.75/133.3	steady run		2.05	12.85	evaporation of propellant?

VI. EXPERIMENTAL DATA AND INTERPRETATION

An overall view of the fundamentally different types of pressure traces obtained in the L-star burner was presented in fig. 4.1. Here, we describe the interpretation of such pressure traces to yield significant information. The information of interest is the boundaries between the different regimes of operation and the amplitudes and frequencies of pressure oscillations as functions of L^* and the mean chamber pressure for the different propellants.

It will be recalled (see Chapter III) that the only two records obtained during a run were one each on the storage oscilloscope and the CEC oscillograph. In other words, no record was stored in an information retrieval system (a tape, for example) to be played back on the oscillograph at a speed desired by subsequent considerations.

In figures 4.1a, b, and c the different regimes of the L^* motor operation are highlighted, each in a separate run. However, the goal was always to conduct a test such as the one shown in fig. 4.1d, not only because of the wealth of information concentrated in a single run, but also because of the sharply-defined boundaries between the different regimes of combustion. Such a run is reproduced in fig. 6.1 to illustrate the data reduction method. This trace was obtained in the run no. 22, in the present program, and employed the CIT-2 propellant. The trace displays the chamber pressure variations as a function of time which progresses from right to left in fig. 6.1.

The pressure transducer (Taber gage) responded to both the large amplitude oscillations and the small amplitude random fluctuations that correspond to the natural noise level of the propellant that is observed even during "time-independent" combustion. This natural noise level is more significant on a relative scale between the propellants than on an absolute scale, since the noise amplitudes rarely exceed one per cent of the Taber gage full-
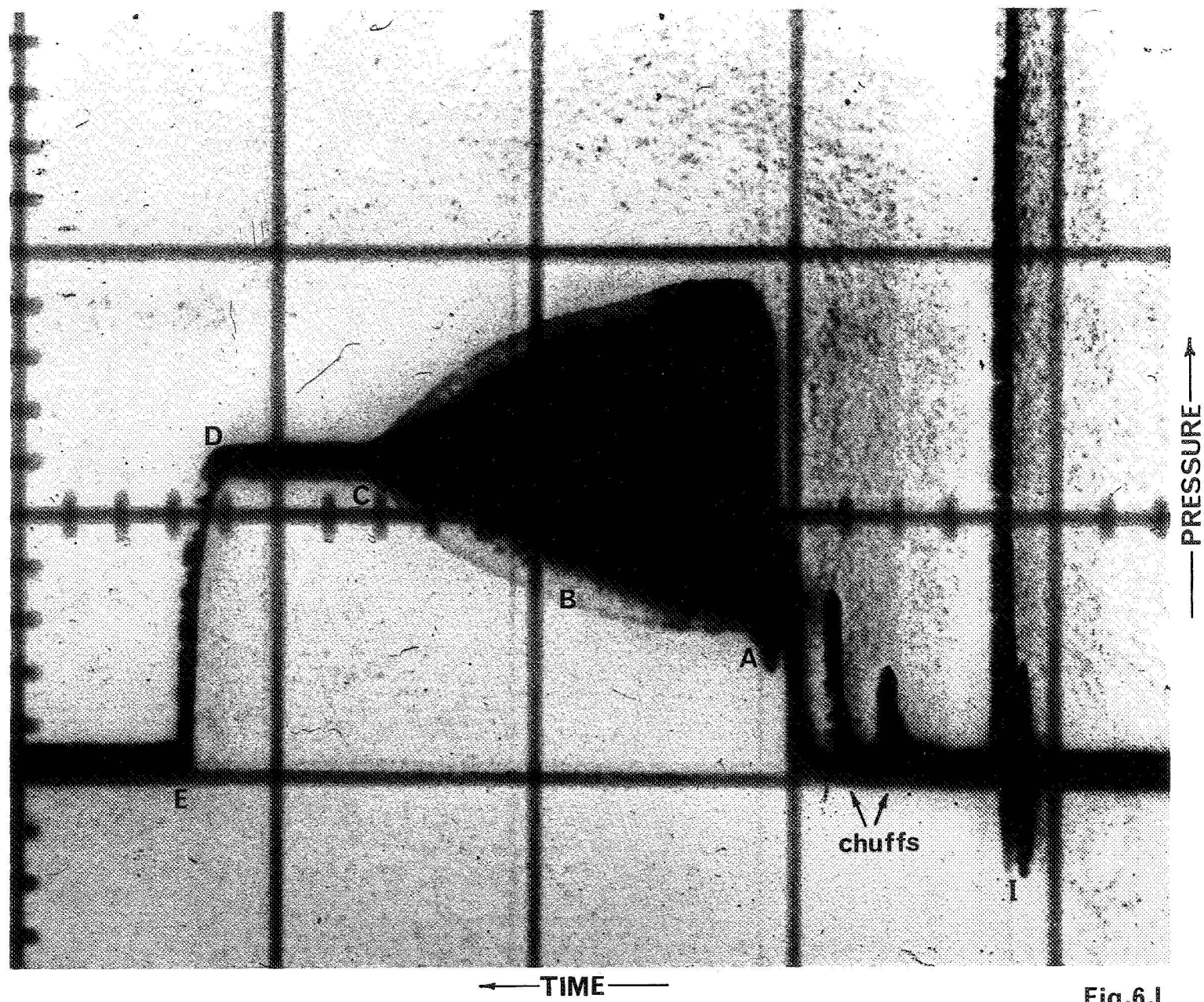
Fig.6.1

scale range. Neither the noise oscillations nor the discrete waveforms during the Helmholtz mode oscillations are discernable in fig. 6.1 because of extensive compression on the time axis. However, both of these are clearly revealed in the extended oscillograph trace (see fig. 6.2, for example).

Now we examine the trace in fig. 6.1. A large pressure pulse originating from the ignitor paste is seen at I. After a time delay of approximately 0.2 second, a pressure spike, corresponding to a chuff, is seen. This is followed by another chuff of a larger magnitude. The mean chamber pressure has not yet registered a value corresponding to time-independent combustion. This is easily understood in view of the non-existence of regular combustion during the chuff mode (discussed in Chapter V). Following these chuffs, the mean chamber pressure rises at A to a value of nearly 28.5 PSIG, corresponding to the establishment of uniform regression of the entire propellant surface. Large amplitude (maximum value, approximately 30 PSI, peak to peak) Helmholtz oscillations appear. These oscillations, superposed on the steady mean value of the chamber pressure, decay in amplitude as time progresses.

The point B represents approximately the mid-location of the Helmholtz mode regime during this run. We remind ourselves that because of propellant consumption as time progresses, the chamber free volume, and hence the characteristic length L^*, increase as time progresses. At C, the L^* has reached a sufficiently large value for the motor to enter the stable regime of operation. Propellant burnout occurs at D, after a short duration of time-independent burning from C to D. The chamber pressure falls to zero at E within approximately 0.05 second after the burnout at D.

In order to know the exact locations of the points of interest (A, B, C, and D) on the L^* scale, it is necessary to have the values of chamber free

volume at these instants. With a knowledge of the speed of data recording, the lengths measured on the trace are related to the time coordinate. The value of the mean regression rate of the propellant in the chamber is needed to relate this time to the chamber free volume. Ideally, one would use the mean regression rate of the propellant, measured during the run; knowing the thickness of the propellant used and the total duration of the run, we can calculate the regression rate. In practice, difficulties are encountered in the precise determination of the significant run duration. The main reason is that the amount of propellant consumed during the chuff mode is difficult to determine from the total duration of the chuff mode operation. This problem is readily appreciated, since the conditions during this regime are far from one-dimensional (see Chapter V).

Attempts to measure the equivalent linear regression rate during the chuff mode were not readily abandoned. There had been a few firings that consisted entirely of the chuff mode (fig. 4.1a, for example). In such firings, it is naturally a simple matter to compute the equivalent linear regression rate as the ratio of the initial thickness of the propellant to the total duration of the run.

Secondly, several of the runs got terminated due to total propellant extinguishment during severe chuff modes. In such cases, measuring the chamber free volume at extinguishment enabled us to determine the amount of propellant consumed during the chuff mode whose duration had been recorded during the firing. Such measurements enable a calculation of the equivalent linear regression rate during the chuff mode operation. Lastly, a time-extended pressure history, as obtained on the oscillograph, gave the actual duration of each individual chuff, which appeared as a sharp spike in the time-compressed storage oscilloscope trace. Summing all such chuff

durations gave an approximate equivalent run time, and hence the regression rate during the chuff mode.

It is regretfully recorded that none of these methods gave a consistent and reliable equivalent regression rate during the chuff mode. However, considering the random and statistical nature of the entire chuff phenomenon, this failure was hardly surprising, although undeniably disappointing.

Returning to our main problem of mean regression rate determination during a run, Crawford bomb data on whichever propellant was under consideration was consistently used in all of the data reduction. Since the mean pressure during the Helmholtz and steady modes of operation could be determined fairly accurately, obtaining the corresponding mean regression rate from fig. 2.7 was straightforward. Comparisons with actual regression rates were made whenever possible; that is, whenever the chuff mode was either absent or insignificant during a run. (Such comparisons are presented in the data tables.) Special care was exercised during the data reduction not to use the Crawford bomb data on the linear regression rates in the calculations pertaining to the chuff mode. This point is further amplified with reference to fig. 6.1. The time intercept DC was measured. This time was multiplied by the linear regression rate (measured at 28.5 psig in fig. 2.7) to get the variation in propellant thickness in the chamber during DC. Since the diameter of the propellant was accurately known, the volume variation during DC was determined. Since the chamber free volume at D had been measured, it was a simple matter to obtain the chamber free volume at C as a simple addition. The free volumes at D and C, together with the nozzle throat diameter (0.338" for run no. 22 on hand) gave the L^*'s at D and C. Following a similar procedure, the L^*'s at B and A were also determined as simple

additions. However, the procedure was not continued into the chuff mode.

The linear regression rate data obtained in the Crawford bomb are definitely not applicable during the chuff-mode operation. The amplitudes of pressure oscillations at A and B were measured, knowing the calibration level of the Taber gage output during the run. The noise level amplitude at C was also measured whenever possible.

The frequencies at A and B (and also whenever possible, the random frequency at C) were measured, selecting short segments of the oscillations on the time axis for counting the number of oscillations during a known interval of time. A suitable reference signal of known frequency was recorded on the CEC oscillograph, along with the Taber gage output, to facilitate accurate determinations of the time coordinate.

While the majority of firings, particularly with the CIT-2 and the $\widetilde{A}$-13 propellants, yielded good experimental data such as the trace shown in fig. 6.1, several runs produced less clearly defined data. The Helmholtz-mode segment of two runs with the A-13 propellant is compared in fig. 6.2. Figure 6.2a presents a pressure trace that is easy to interpret. The beginning, the midpoint, and the end of the Helmholtz mode are clearly defined at instants A, B, and C, respectively. The pressure trace in fig. 6.2b does not yield the same information with equal clarity. The pressure oscillations appear, grow gradually, decay to a smaller amplitude, and grow again; the pressure amplitude never grows to a large value, but varies a little around a small value that is not much larger than the instrinsic noise level characteristic of the propellant (which is seen around the point N). While such pressure traces cannot be called imperfect, with our incomplete comprehension of what a pressure trace ought to be during an unstable firing, they are certainly inconvenient
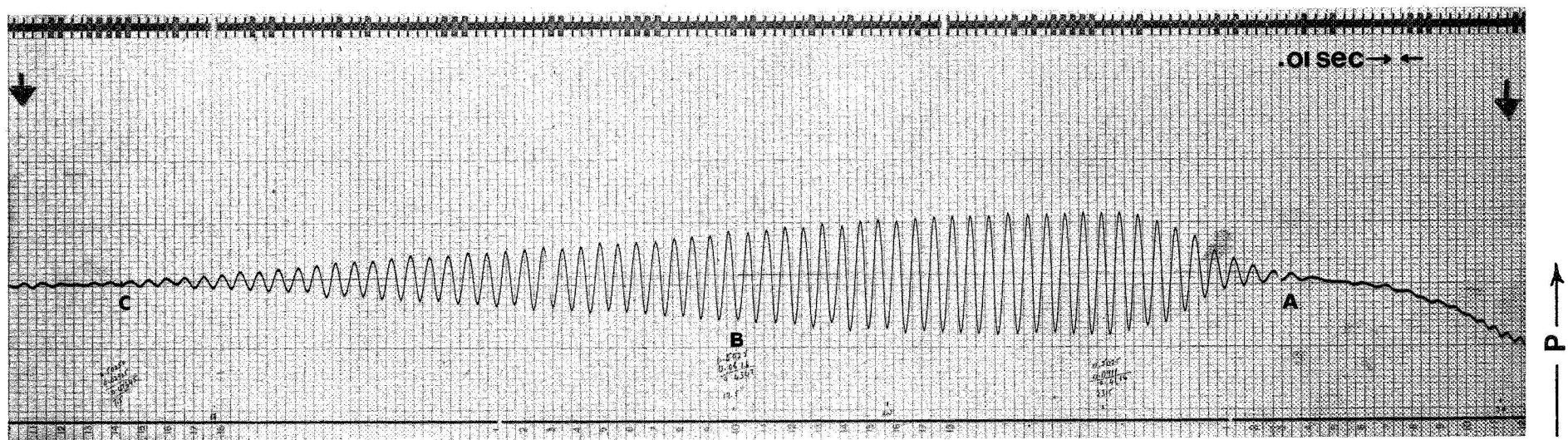
(a) Easily interpreted history (run no. 161, $\overline{P}$ = 32.55 PSIA, L^* - 60 - 80 cm).
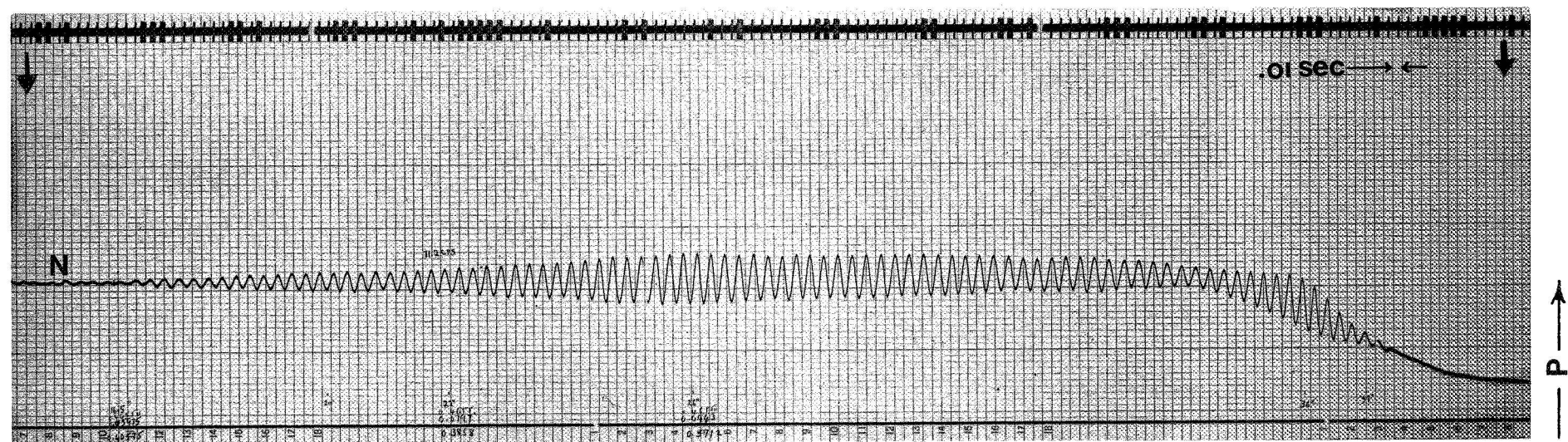
(b) Less certain history (run no. 160, $\overline{P}$ = 28.20 PSIA, L^* - 50 - 70 cm).

Figure 6.2 PRESSURE-TIME TRACES OBTAINED ON THE OSCILLOGRAPH. EXAMPLE: $\widetilde{A}$-13 PROPELLANT.

for data interpretation and generally have not been included in the data tables in this report. One qualitative feature common to many of the firings that produced traces such as the one shown in fig. 6.2b was that the ignition process departed from the normal in one way or another.

In general, the difficulty in obtaining experimental data increased with the size of the oxidizer particle in the propellant. This difficulty with the coarser oxidizer particle propellants was manifest in two principal characteristics. First, these propellants exhibited a general reluctance to enter the Helmholtz mode instability; second, even if these propellants could be persuaded to enter the Helmholtz mode with careful tailoring of the experimental conditions, the (dp/dt) during the oscillations was often strong enough to extinguish the propellants after only a few cycles. A stability map for the propellant is about the only information that can be obtained from a test unless the propellant enters the Helmholtz mode. (During a firing, the L^* and the D^* are known, and the pressure trace reveals whether the firing was stable or unstable. Such information, covering a wide range of L^* and D^*, yields the stability map for the propellant.)

However, unless the pressure trace shows Helmholtz oscillations gradually decaying into the time-independent regime, as shown at C in fig. 6.1, the stability boundary cannot be sharply defined. Also, the interesting details of pressure amplitudes, frequencies, and their relation to L^* and the mean chamber pressure cannot be obtained from a pressure trace devoid of Helmholtz oscillations. During the present program, all of the propellants except CIT-4 yielded at least a few runs with extensive Helmholtz oscillations.

The difficulty of exciting the Helmholtz oscillations in the coarser oxidizer particle propellants is believed to hold the key to an understanding of the L-star instability in rockets as discussed in the subsequent chapters.

VII. RESULTS AND DISCUSSION

7.1 Introduction

A thorough understanding of L^* instability in rockets should ultimately result in the elucidation of the variations of any parameter of interest. For the present, we are concerned with those facets that are thought to be funda-mental enough to incorporate in them most of the significant information. These are the frequency of oscillations, the stability maps, and the amplitude of pressure oscillations. In the absence of theoretical predictions for these quantities, our success at explaining these phenomena is reflected in recon-ciliation of experimental data with qualitative physical explanations.

A majority of discussions in this chapter is concerned with the Helm-holtz mode oscillations; that is, the segment AC in pressure traces such figs. 6.1 and 6.2a. Excluding time-independent combustion (fig. 4.1c, for example) of the various pressure-time histories obtained, the Helmholtz mode appears to be the most ordered, and presumably the one most amenable to a theoretical explanation. Naturally, treatments of the other modes of operation, namely chuff and depressurization-rate extinguishment, may be attempted subsequently. However, as seen later in this section, several im-portant aspects of even the Helmholtz mode elude complete comprehension at the present time.

The frequency of Helmholtz oscillations is seen to bear a strong rela-tion to the characteristic transit time in the condensed phase, namely ratio of the oxidizer particle size to the mean regression rate. Also, simple correla-tion of the frequency with the chamber characteristic length (L^*) is shown to be limited to each particular propellant only, and to lack universal validity. It is also seen that the oxidizer particle size is a more relevant length scale in the condensed phase than the characteristic thermal depth ($\varkappa/\bar{r}$), at least

for the Helmholtz oscillations.

The stability maps, which separate regions of time-independent and time-dependent combustion on plots of pressure versus L-star, are seen to be parabolic in shape, with dual pressure limits for stability in the L-star range of interest. Attempts are made to preduct the high pressure limit for unconditional stability. Postulating that the condensed-phase heat reservoir $(c \cdot \Delta T)$ effects are important for driving the oscillations, a criterion is sought for classifying the condensed phase as homogeneous or heterogeneous for the purposes of heat transfer calculations. The relative magnitudes of the characteristic thermal depth in the condensed phase and the oxidizer particle size are used for such a criterion. The agreement is found to be excellent for the 11μ (CIT-2) propellant and fair for the 39.5μ ($\widetilde{A}$-13) propellant; the agreement is rather poor for the coarser oxidizer (CIT-3 and CIT-4) propellants.

The amplitudes of pressure oscillations are seen to present very difficult problems, even for simple correlations. While several explanations are offered for this difficulty, it is evident that more research is needed to clarify matters.

Finally, no attempts are made to compute the response functions from the pressure-time traces. In the L^* burner, the growth of pressure oscillations occurs during progressive decreases in the L^* value, and unless a careful account is taken of this non-stationary nature, the results may not be valid. Since the full growth usually occurs within a few cycles, it is not easy to measure the growth constants, which are meaningful only in the small amplitude (linear) regime. That is, when the growth is spread over a large number of cycles (at least a hundred), the growth constants are readily in-

terpreted. Also, the rapidly varying chamber conditions could introduce large uncertainties in all such interpretations. (The readers will note the similarity to the decay constants measured in T-burners[3], where large uncertainties are present because of the rapidly changing chamber conditions.)

The pressure records obtained during these tests are available for extracting more information than what has been presented in the data tables of this report.

7.2 Frequency of Helmholtz Oscillations

After an extensive study of NAI (Non-Acoustic Instability, or L^* instability in the present terminology) covering four different propellants, researchers at the Naval Weapons Center present[5] an unique correlation between the values of the characteristic length, L^*, and frequency of oscillations, f. The correlations (fig. 5.16 in ref. 5) cover data on the different propellants at various chamber pressures. Consequently, one of the first correlations attempted in the present study was a plot of L^* versus f. Such a plot is presented in fig. 7.1 for the four propellants of the present program. It is seen that the correlation is most unsatisfactory, although for each particular propellant, good correlation is evident. Since our experimental data appear to be at least as good as the NWC data, this lack of correlation indicates in a very simple way that an important effect is being overlooked.

It is apparent that the oxidizer particle size must be the important parameter. This follows from the simple reasoning that the oxidizer particle size is the only parameter that is different among the four propellants of the present study. Consequently, the differences in L^* instability behavior, noted in fig. 7.1, must be attributable to it. Proper incorporation of the particle size in the frequency variable is, therefore, expected to improve the correlations.

The normalized frequency $(f a/\bar{r})$ incorporates the effects of the particle size naturally. The ordinate L^* is a variable that is far more directly relevant to the vapor phase processes than to the condensed phase processes; L^* should be normalized by another significant length scale in the vapor phase. The only relevant length scale appears to be the flame standoff distance X^*, whose numerical value is not readily accessible. However, the value of X^* scales with the ratio of the thermal diffusivity $\varkappa_{gas}$ (of the combustion gases) to the mean flow velocity $\bar{u}$ above the propellant. Hence, $(L^* \bar{u}/\varkappa_{gas})$ is used as the
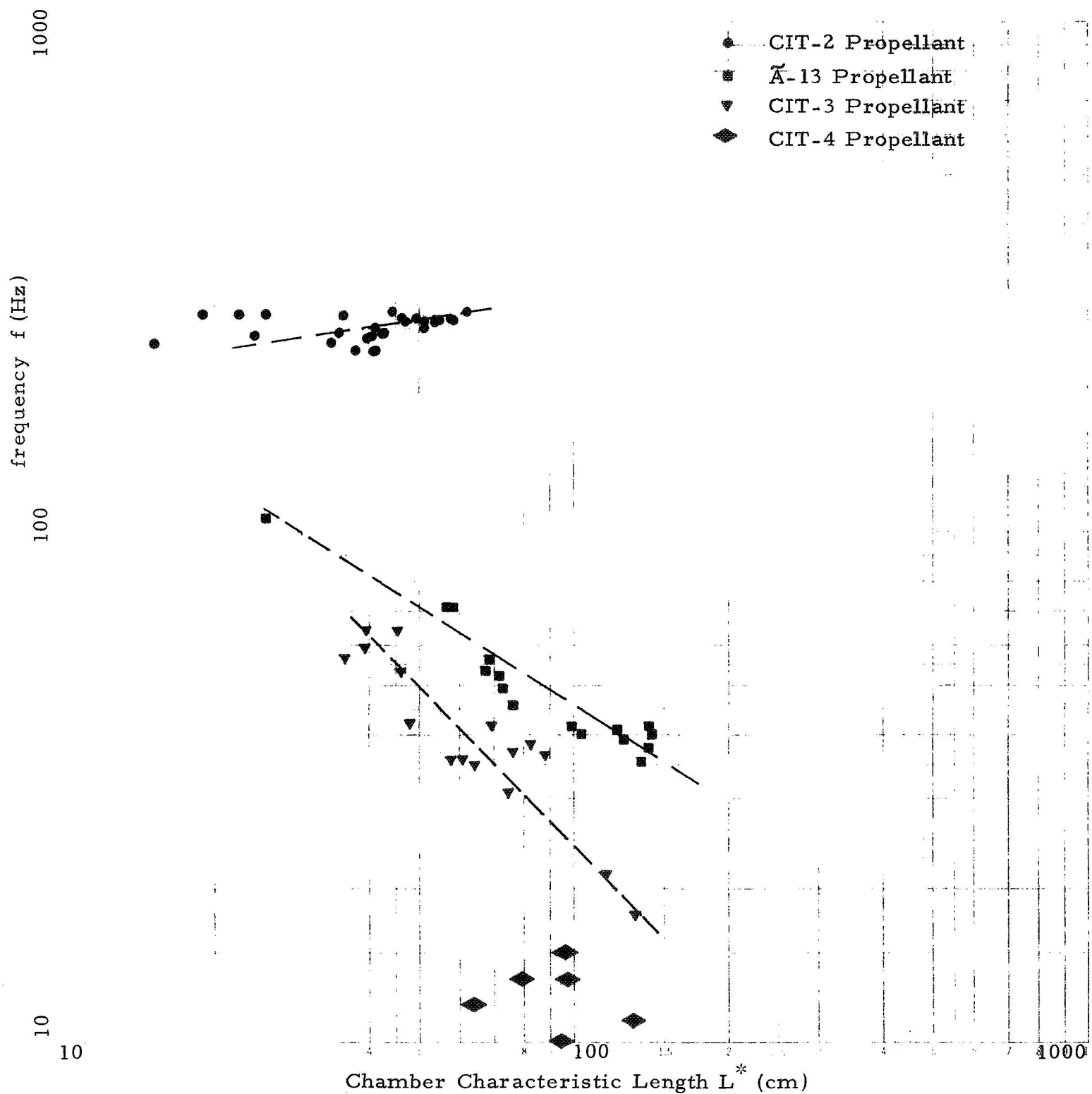
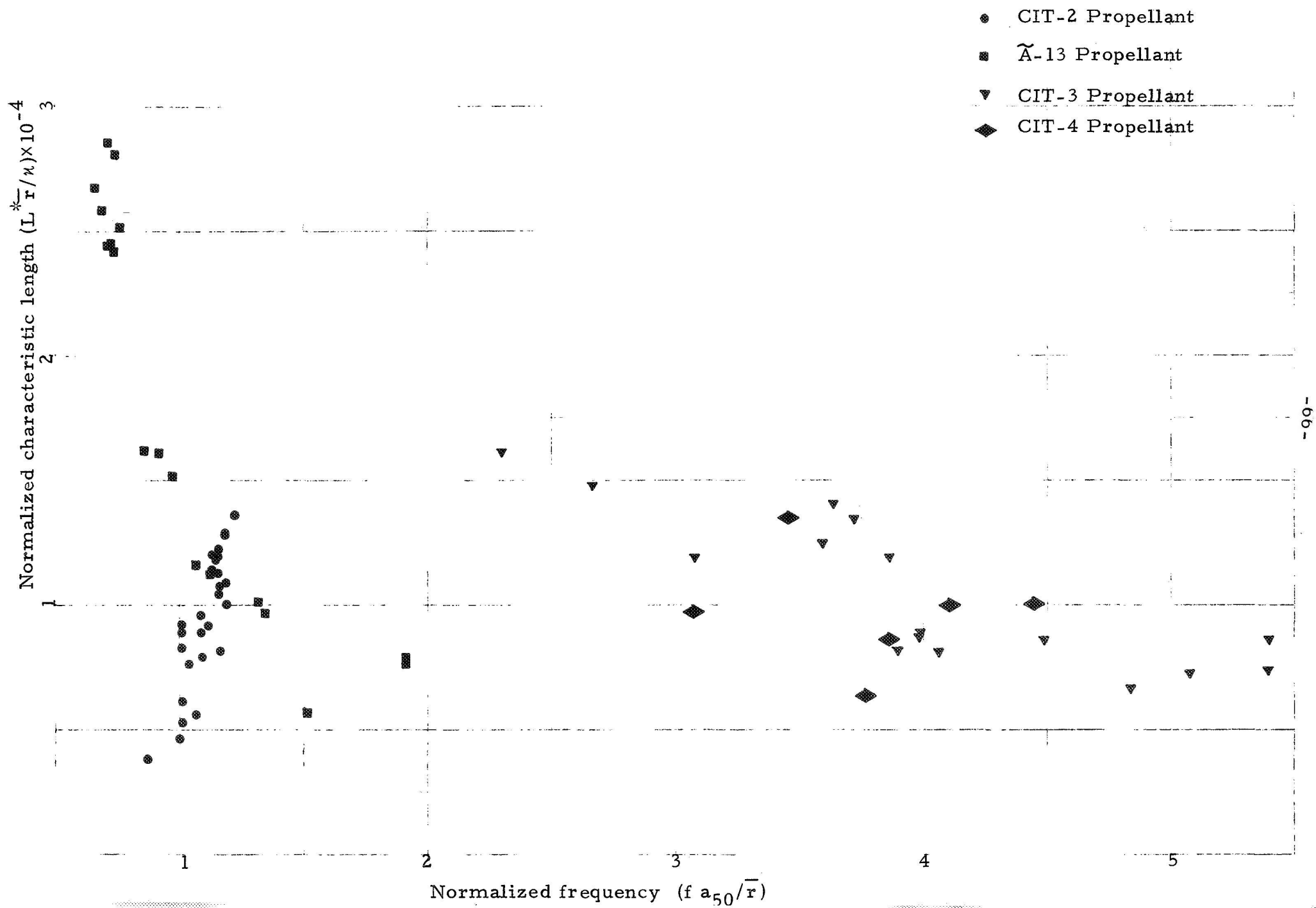Fig. 7.1 FREQUENCY DEPENDENCE ON L^* DURING HELMHOLTZ OSCILLATIONS.

normalized ordinate. Recognizing that $\bar{u} = \bar{r}\,(\rho_{solid}/\rho_{gas})$, and that the value

of k/c for the gas is not too different from that for the solid, we write

$$\frac{L^{*}\bar{u}}{\varkappa_{gas}} \propto \frac{L^{*}\bar{r}}{\varkappa}$$

and use the latter group as the normalized L^{*}. The values of both $\bar{r}$ and $\varkappa$

are convenient to use in the present context. Nevertheless, the above sequence

of relations should always be remembered while examining the correlations to

be discussed shortly. In the present report, a constant value of $\varkappa$ is used for

all four of the propellants. First, the values of $\varkappa$ are not precisely known for

the different propellants, although a value of $0.0011 \text{ cm}^2/\text{sec}$ is normally

taken as reasonably representative of reality. Second, even if the value of

$\varkappa$ is found to be different for the propellants, the ordinate $(L^{*}\bar{r}/\varkappa)$ would not

change, as the preceding arguments indicate that $\varkappa$ is introduced only as a

convenient substitute for $\varkappa_{gas}$. The value of $\varkappa_{gas}$ should be nearly identical

for the four propellants, which are identical in chemical composition. It is

noted in passing that other normalizations of L^{*}, like for example $(L^{*}f/\bar{u})$,

invariably introduce the frequency into the ordinate and their correlations with

frequency may not be meaningful.

Before proceeding with the plots, the question of the particle size has

to be resolved. It is recalled that the existence of distributions for the parti-

cle sizes introduces a degree of arbitrariness (that would be absent with truly

unimodal particles). At this stage, we use the conventional 50 per cent wt.

average point and plot the results in fig. 7.2. An unmistakable improvement

in correlation is evident in comparison with fig. 7.1. Thus, the choice of the

parameter $(f\,a/\varkappa)$ has proved fruitful. The correlation in fig. 7.2 also indi-

cates that the heterogeneity scale (a) in the propellant is very important for

L^{*} instability. This conclusion naturally points out that the 100 per cent wt.

Fig. 7.2 NORMALIZED L* DEPENDENCE ON NORMALIZED FREQUENCY DURING HELMHOLTZ OSCILLATIONS.

CIT-2 Propellant
$\widetilde{A}$-13 Propellant
CIT-3 Propellant
CIT-4 Propellant

Normalized characteristic length $(L^* \bar{r}/\varkappa) \times 10^{-4}$

Normalized frequency $(f\, a_{50}/\bar{r})$

-99-

average point may be a better choice (for a) than the 50 per cent wt. average point. The physically realistic heterogeneity is more readily associated with the a_{100} than with a_{50}, which is after all a designation of convenience only. A plot based on $(f a_{100}/\bar{r})$ is presented in fig. 7.3. In comparison with fig. 7.2, vast improvement is evident, and definitely leads one to believe that a_{100} is the proper length scale of importance in L^* instability.

It now remains to account for the remarkably simple correlation obtained by the NWC researchers. Although they obtained data on four different propellants, three of those propellants used the <u>same oxidizer particle size</u>; the fourth propellant used a bimodal distribution whose weight-average equivalent mean size was not far from those of the other three (table 5.1 in ref. 5). In other words, although various parameters such as the chemical composition, fuel binder, metal content, and the fuel/oxidizer ratio were varied in their study, the single most important parameter (a) was varied little among the four propellants. Thus, the propellants that were "different" in many respects might as well be considered identical so long as we restrict our attention to L^* instability, where the oxidizer particle size appears to be the prime variable.

In normalizing the energy equation applied to the condensed phase, the group $\Omega \equiv f \varkappa/\bar{r}^2$ is often brought out as the only relevant nondimensional frequency. However, behind such treatments is the implicit assumption that the condensed phase is homogeneous. If the condensed phase is treated as homogeneous, for the purposes of heat transfer calculations, $\varkappa/\bar{r}^2$ appears to be the only natural time scale in the problem, and hence the group $(f \varkappa/\bar{r}^2)$. If the effects of particle size are explicitly retained in writing the energy equation for the condensed phase, $a/\bar{r}$ is a very relevant time scale which leads to the group $(f a/\bar{r})$ as a significant normalized frequency. To clearly display the

Fig. 7.3 NORMALIZED L* DEPENDENCE ON NORMALIZED FREQUENCY DURING HELMHOLTZ OSCILLATIONS.
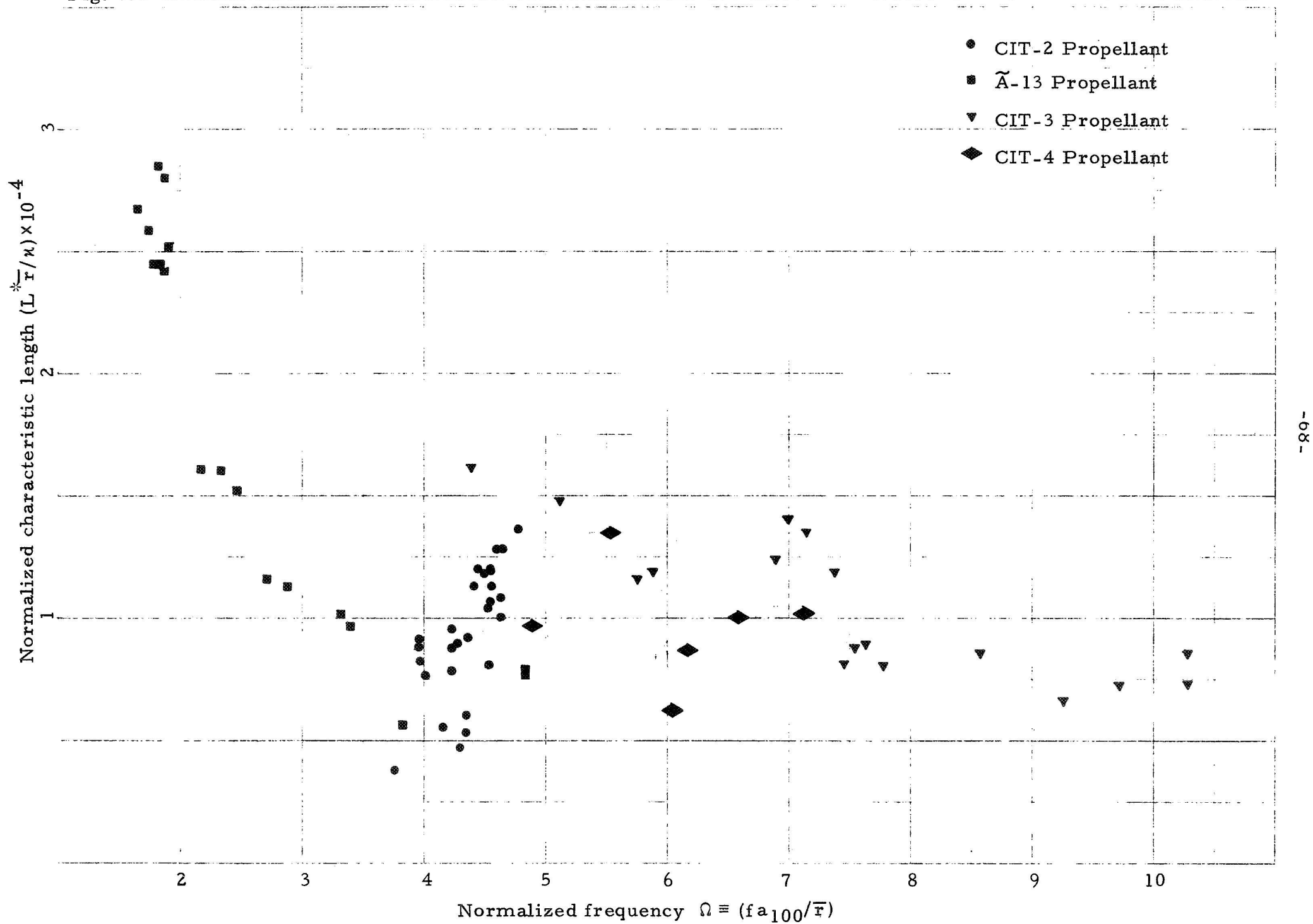
consequences of such a reasoning, figs. 7.4 and 7.5 were prepared. The physical characteristic length L^* is plotted against $\Omega \equiv f\varkappa/\bar{r}^2$ in fig. 7.4 and the normalized characteristic length $(L^*\bar{r}/\varkappa)$ is plotted against Ω in fig. 7.5. It is seen that the correlations are unsatisfactory and are most definitely inferior to the ones in figs. 7.2 and 7.3. The fact that the group $(fa/\bar{r})$ correlates experimental data much better than the group $(f\varkappa/\bar{r}^2)$ strongly supports the view that the oxidizer particle size in the propellant is indeed a very important parameter in L^* instability.

Figures 7.4 and 7.5 indicate that although the mean regression rate $\bar{r}$ implicitly incorporates the effects of oxidizer particle size in the propellant, it is not sufficiently significant in bringing out the strong influences of the oxidizer particle size on L^* instability. This conclusion has far-reaching consequences, and is of fundamental importance to all analyses of L^* instability in rockets.

Fig. 7.4 L* DEPENDENCE ON CONVENTIONAL NORMALIZED FREQUENCY.

-70-
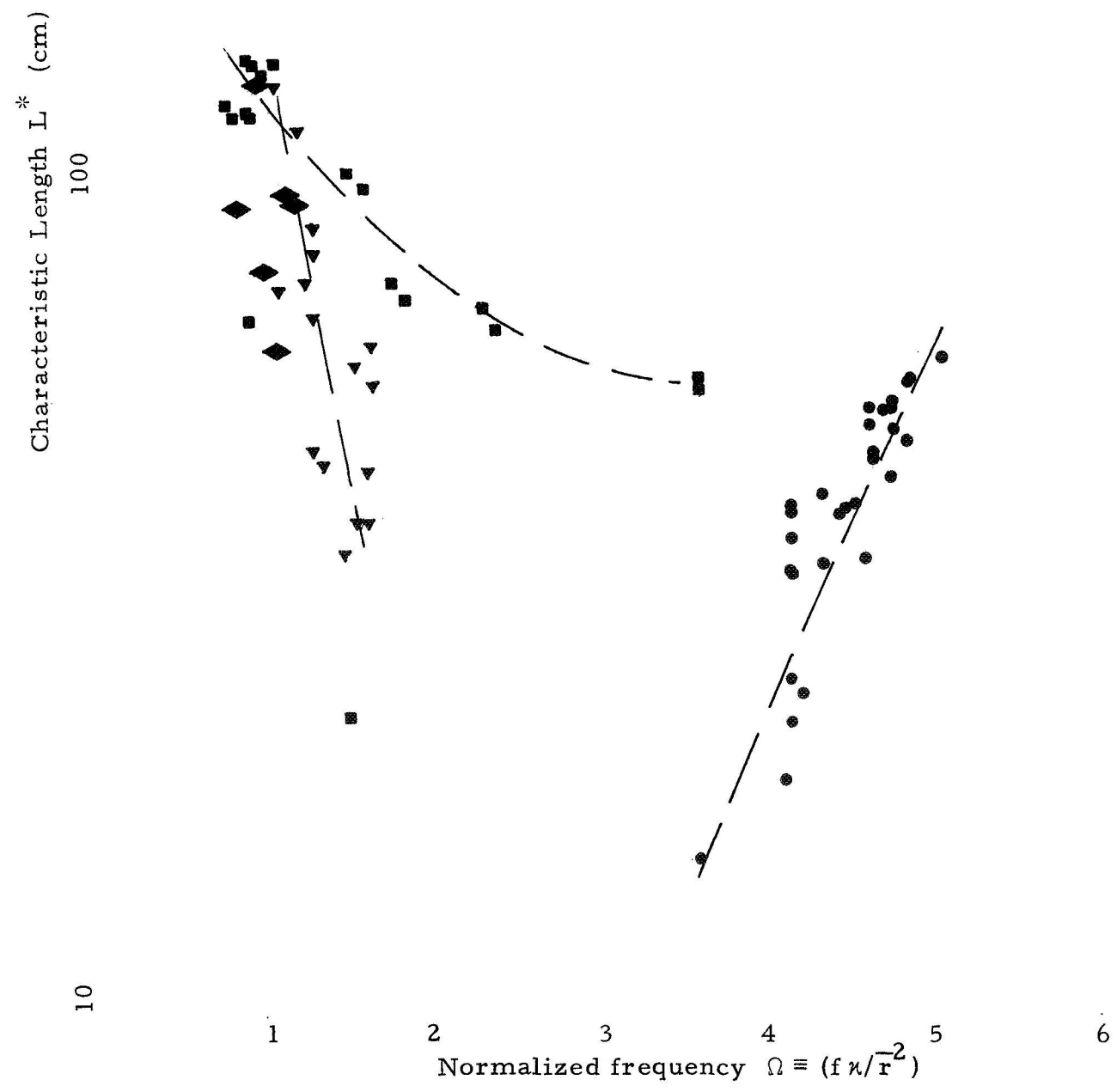
Fig. 7.5 NORMALIZED L* DEPENDENCE ON CONVENTIONAL NORMALIZED FREQUENCY.

CIT-2 Propellant

$\widetilde{A}$-13 Propellant

CIT-3 Propellant

CIT-4 Propellant

Normalized characteristic length $(L^* \bar{r}/\varkappa) \times 10^{-4}$

Normalized frequency $\Omega \equiv (f\varkappa/\bar{r}^2)$
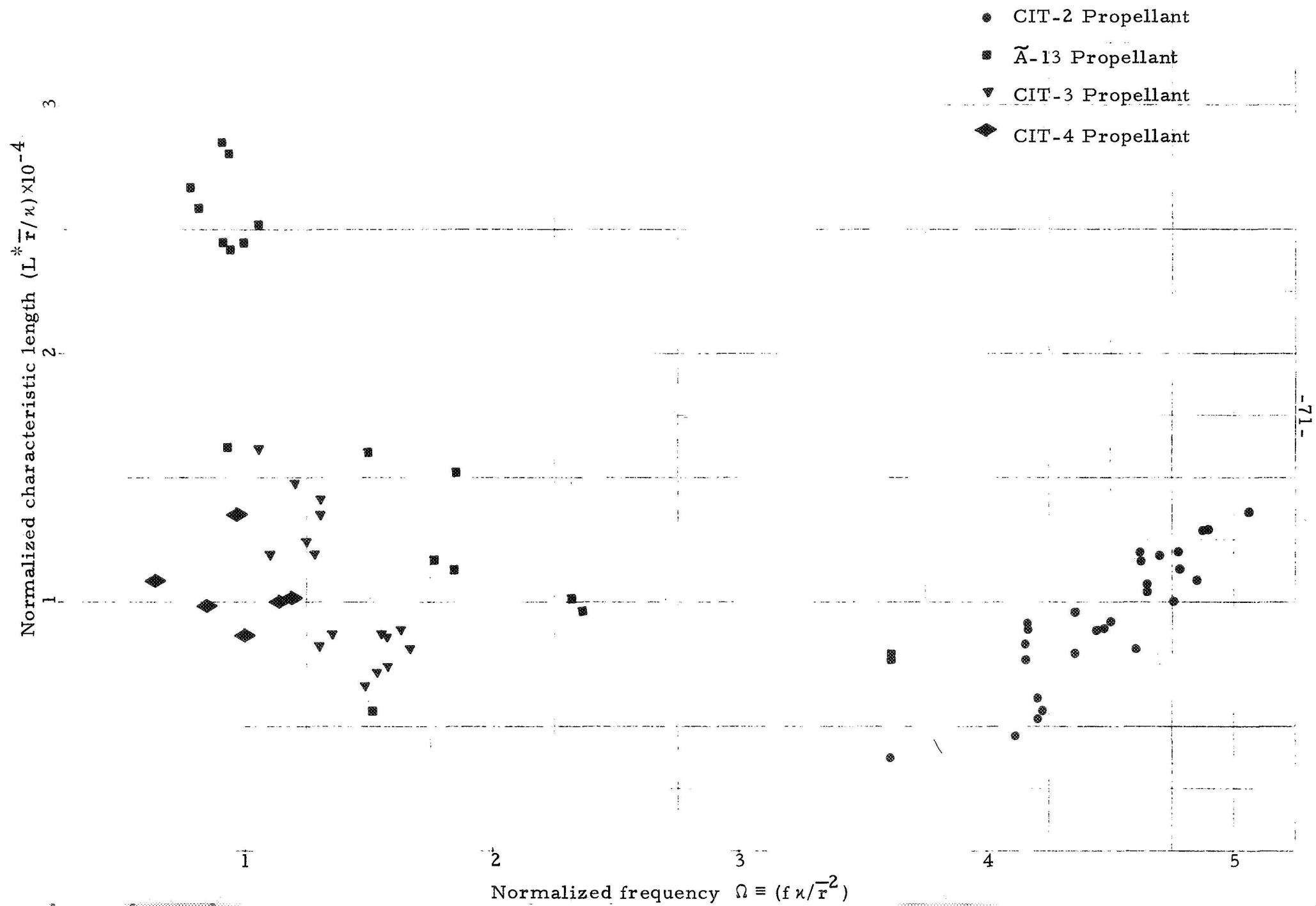
7.3 The Stability Boundary

The classical characterization of the L^*-instability tendencies of a propellant is simply a map for the propellant where the regions of time-independent combustion are distinguished from the regions of oscillatory (or unsteady) combustion. Normally, the value of L^* is plotted against the mean chamber pressure, P. Such maps are obviously valuable for rocket motor design. In fact, the principal aim at the start of the present program was to obtain the maps for all four propellants in an effort to understand the influences of propellant heterogeneity on combustion stability. Since the mean chamber pressure and the value of L^* at the transition point (C in figs. 6.1 and 6.2a) between Helmholtz and time-independent combustion mode are generally known from the experimental data, the maps are prepared easily. Curves representing the loci of such points separate regions of stable and time-dependent combustion of the propellants. As already mentioned, the CIT-4 propellant was the only one (among the four) that did not yield traces such as the ones shown in figs. 6.1 and 6.2. This fact resulted in obtaining sharp stability boundaries for three of the propellants only. The stability maps are presented in figs. 7.6 - 7.9.

The general characteristic of the stability boundary appears to be a closed region, nearly parabolic in shape, on the P-L^* plot. (The lower limit on the value of L^* is obviously zero.) Experimental data on the $\widetilde{A}$-13 propellant clearly indicate such a boundary (fig. 7.7). With somewhat lower clarity the CIT-3 propellant also indicates such a boundary (fig. 7.8). For the CIT-2 propellant, experimental difficulties prevented motor operation in the region covering the lower-pressure segment of the parabola. The nozzle unchokes at the lower chamber pressures with atmospheric back pressures. The unchoking introduces a number of new difficulties in data interpretation. Although

Fig. 7.6 STABILITY MAP OF THE CIT-2 PROPELLANT.

Ã·13 PROPELLANT

stable

oscillatory

L*
(proportional to chamber free volume), cm

100

10

300
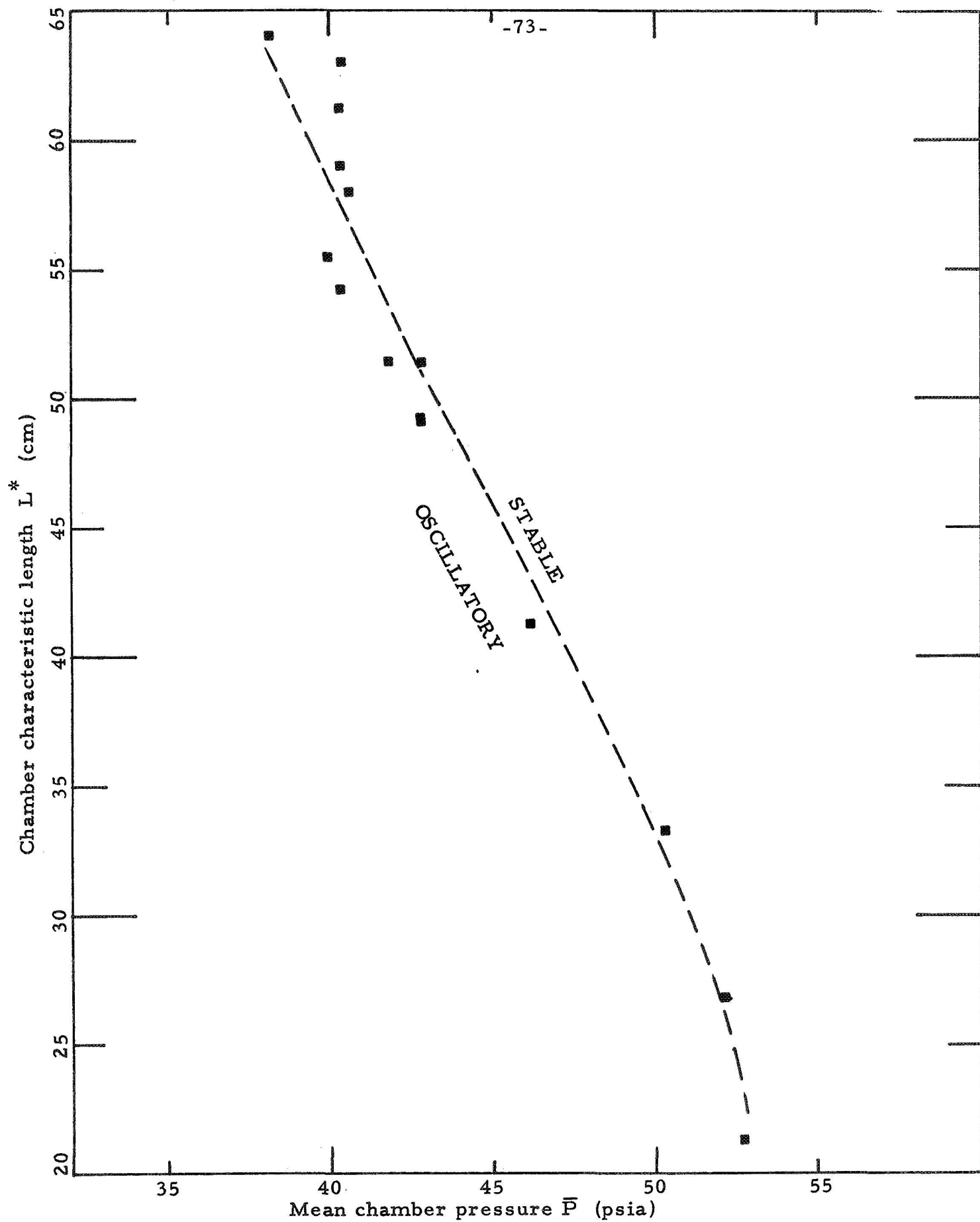
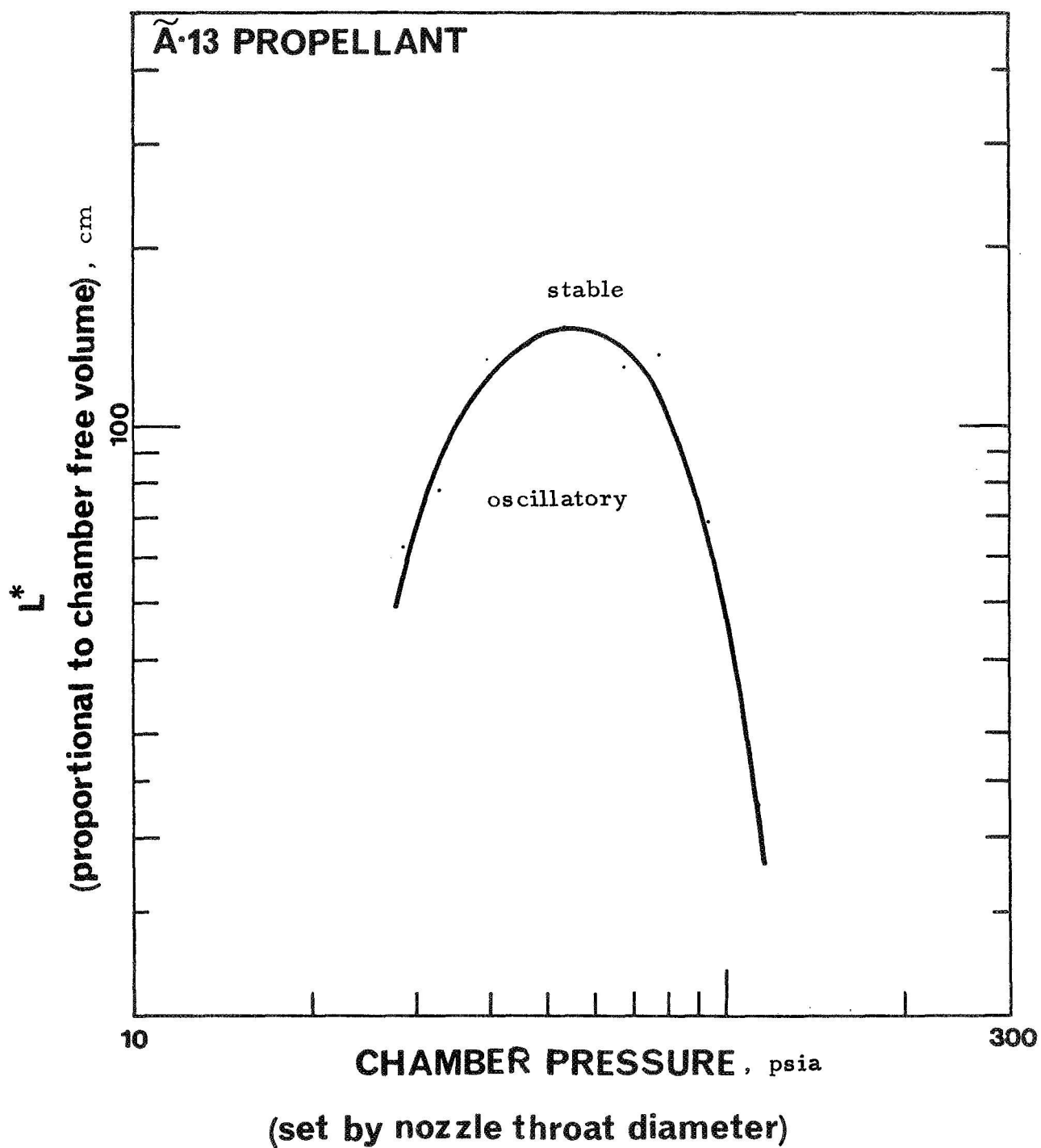CHAMBER PRESSURE, psia

(set by nozzle throat diameter)

Fig. 7.7 STABILITY MAP OF THE Ã-13 PROPELLANT
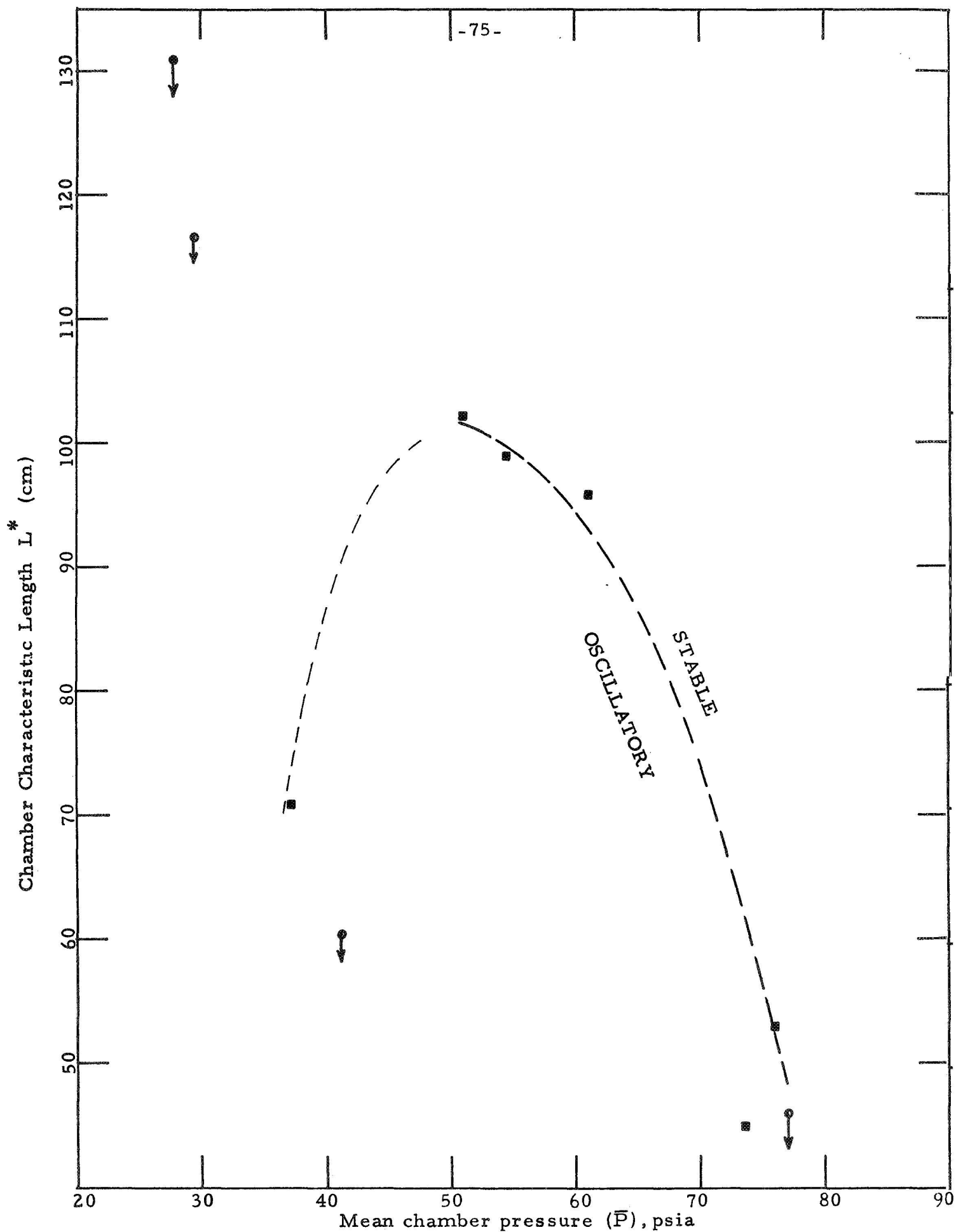
Fig. 7.8 STABILITY MAP OF THE CIT-3 PROPELLANT.
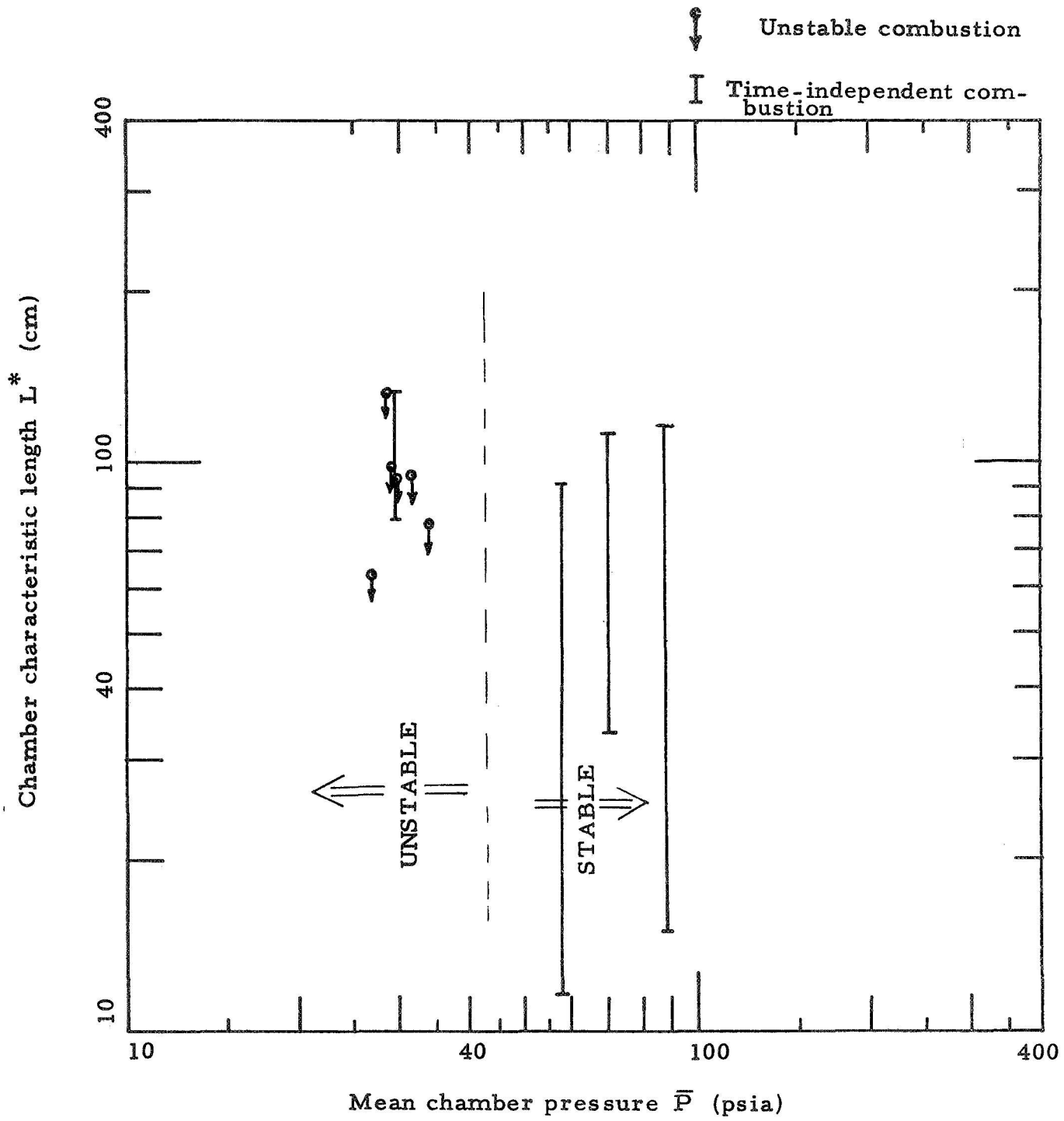
Fig. 7.9 STABILITY MAP OF THE CIT-4 PROPELLANT.

a program was initiated to conduct a few tests with subatmospheric back pressures, the tests were not pursued fully, for reasons explained in Appendix I. Data on the CIT-4 propellant (fig. 7.9) do not show a sharp boundary, even in the higher pressure region, and it is easily appreciated that data are not easily obtained at the lower pressures.

The parabolic shape for the stability boundary is at variance with earlier data[2] that had indicated a straight-line boundary on the log P - log L^* plot. The experiments[2] referred to used a bimodal oxidizer distribution with a different (from PBAN) binder system; however, such details are not expected to alter the qualitative nature of the stability boundary. It would appear that the earlier data[2] covered the high-pressure segment of the parabolic boundary. A straight line is a reasonable approximation for that segment, sufficiently away from the maximum L^* point. The very recent data[8] from ONERA, which clearly indicate the parabolic nature of the stability boundary, provide further support for our experimental results.

While the universal nature of the parabolic boundary has not been conclusively established, at least the high pressure limit has been known for several years. That is, the existence of a mean chamber pressure for each propellant, above which the combustion is time-independent irrespective of the value of L^*. Naturally, an understanding of this phenomenon can be associated with progress towards an understanding of L^* instability itself. While there may be several paths towards the delineation of this phenomenon, the approach chosen here is through the condensed phase details. Needless to add, this choice is influenced by the earlier revelation of the important role of the oxidizer particle size during the Helmholtz oscillations (Section 7.2).

Even in the absence of a formal analysis of L^* instability, the role of the condensed phase as a heat reservoir is evident. Temperature fluctuations

in the condensed phase, "charge" and "discharge" the reservoir through the

$c \cdot \Delta T$ effect. This effect, when coupled to the fluctuations in gas phase

energetics, can lead to self-sustained oscillations in combustion-related

variables. For the condensed phase to act like a good heat reservoir, it would

appear that the condensed phase material be homogeneous. By its very nature

the composite propellant has come to be regarded as a heterogeneous sub-

stance; however, the physical scale of heterogeneity is more relevant than a

characterization such as homogeneous/heterogeneous substance. The physical

scale of heterogeneity in the propellant is the oxidizer particle size (a) .

The physical scale of relevance to heat transfer in the solid is the

thermal depth in the propellant material (see fig. 7. 10). The mathematical

depth appears as infinity, but a distance to reach 1/e of the wall temperature

difference $(\overline{T}_w - T_o)$ is normally taken as a physically meaningful characteristic

depth. Application of the thermal energy equation to the condensed phase,

neglecting for simplicity the chemical reactions, yields the solution

$$\frac{\overline{T} - T_o}{\overline{T}_w - T_o} = \exp(-\overline{r} x / \varkappa) \; ,$$

so that the distance $x_T = \varkappa / \overline{r}$ is the characteristic thermal depth in the solid.

So long as x_T is greater than the characteristic heterogeneity scale (a),

the condensed phase may be considered homogeneous for the purposes of heat

transfer calculations. If x_T gets to be comparable to a , it is difficult to

visualize the condensed phase as homogeneous for the purposes of heat transfer.

Naturally, the heat reservoir effects are expected to be much less pronounced

in regimes of operation where

$$(\varkappa / \overline{r}) = x_T \lesssim a \; .$$

The above arguments show that increasing values of the mean regression rate
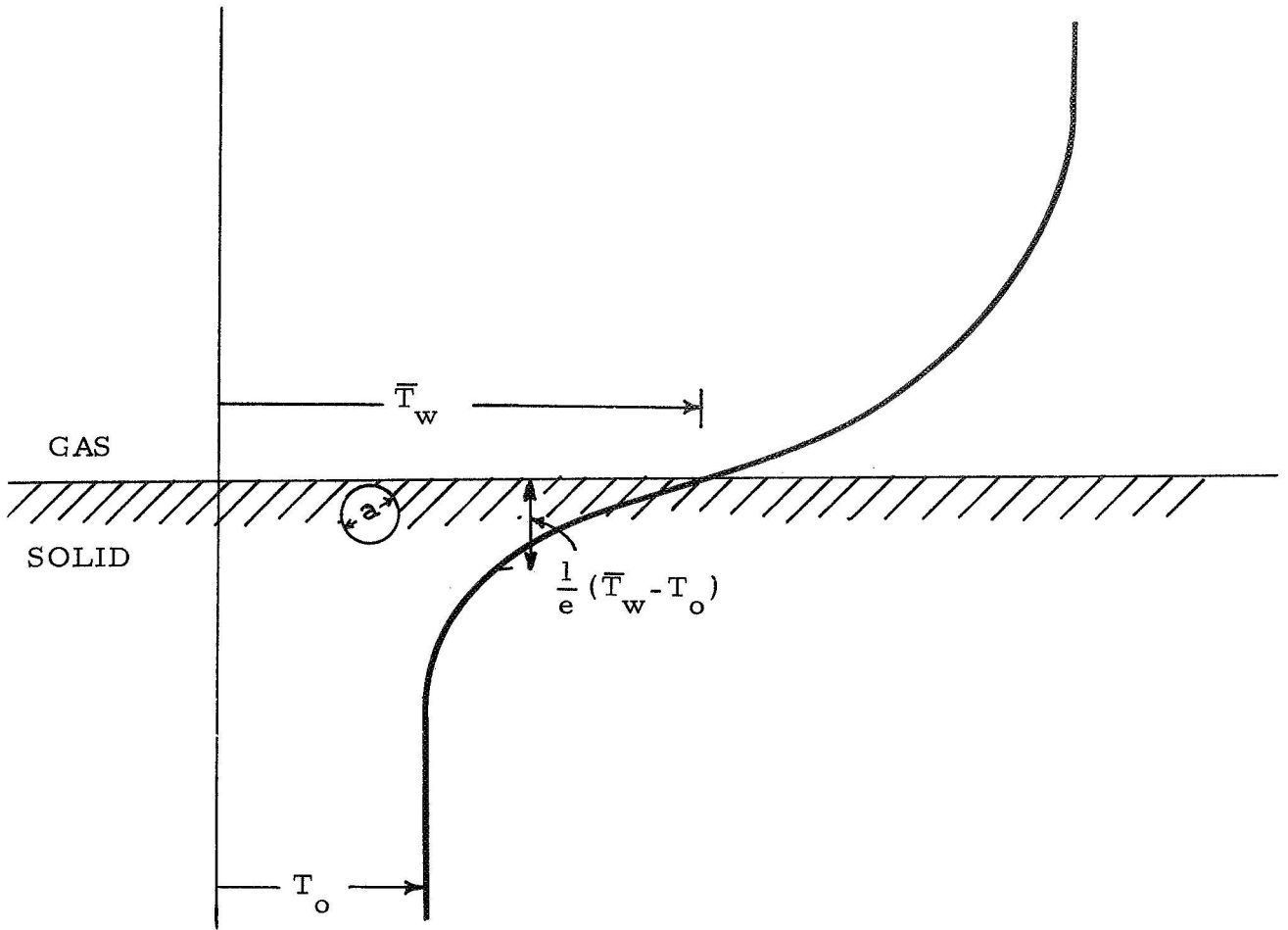
Fig. 7.10 THERMAL PROFILE IN THE CONDENSED PHASE.

progressively take the propellant away from the homogeneous-solid limit.
(The thermal diffusivity $\varkappa$ is assumed not to vary significantly with the mean
regression rate; $\varkappa$ is known to be temperature dependent and the condensed
phase temperature near the wall is known not to vary significantly with regres-
sion rate.) Since increasing regression rates are generally associated with
increasing chamber pressures (i. e. , a positive value for the pressure index
n like all four of the present propellants have), the preceding reasoning indi-
cates that there should exist a mean pressure for each propellant, above which
the instability tendencies are subdued.

In order to verify this reasoning, table 7. 1 has been prepared. Values
of the mean regression rate, above which the instability tendencies are ex-
pected to be small, are compared with the values of the mean regression rate $(\hat{r})$
beyond which each propellant is experimentally found to be unconditionally
stable in the L^* mode. The value of a_{100} is used instead of a_{50}, since pre-
vious developments (Section 7. 2) indicate that a_{100} is the physically significant
length scale in the condensed phase.

Table VII. 1 Comparison of Deduced and Experimental Stability Limit

Propellant	a_{100} cm	$\varkappa/a_{100}$ cm/sec	$\hat{r}$ (experimental) cm/sec
CIT-2	0.0043	0.256	0.266
$\widetilde{A}$-13	0.01	0.11	0.295
CIT-3	0.0175	0.0328	0.211
CIT-4	0.035	0.0195	$\langle 0.142 \rangle$

As seen in Table 7. 1, the agreement for the CIT-2 propellant is very
close. There exists an independent observation that strengthens the argument

further. When the thermal depth gets to be smaller than the heterogeneity scale in the condensed phase, the steady-state linear regression rate plot is expected to reveal interesting characteristics. For example, surface reactions at the wall are likely to assume greater importance at regression rates greater than $\hat{r}$. If they do, the slope (n) of the Crawford bomb data must undergo a considerable change, as discussed[5] in connection with surface reactions. The Crawford bomb data on the CIT-2 propellant (fig. 2.7) shows an abrupt break at $\hat{r}$ (0.266 cm/sec $\sim$0.105 in/sec). Thus, the CIT-2 propellant seems to fit the thermal-depth picture remarkably well.

The agreement for the $\widetilde{A}$-13 propellant (Table 7.1) may be considered reasonable, although the agreement suffers in comparison with the CIT-2 data. Agreement for the CIT-3 and CIT-4 propellants is poor. However, the abrupt break in the Crawford bomb data on the CIT-3 propellant (fig. 2.7) near a mean regression rate of $\bar{r} = 0.08$ in/sec ($\approx$0.204 cm/sec) is remarkably close to the stability limit $\hat{r}$ noted in table 7.1. Naturally, this would seem to indicate the importance of the condensed phase details. Also, it is difficult to believe that the thermal-depth picture can lose its applicability completely, after such a success in explaining the CIT-2 data. A progressive increase in the value of the thermal diffusivity ($\varkappa$) with increases in the material heterogeneity improves the agreement somewhat. But in the absence of accurate data on $\varkappa$ such a hypothesis is purely speculative. However, the slower-burning propellants (coarse oxidizer particle propellants) are likely to have a lower surface temperature, and the $\varkappa$ is known to decrease substantially with temperature, so that the postulated effects of $\varkappa$ variations are not completely ad hoc.

Another explanation is offered for the progressive deterioration in the comparisons noted in table 7.1. As a rule, the low burning-rate propellants

are prone to condensed-phase "cooking" before burning. This empirically known effect is supported by theoretical considerations[5] also.

Consider a thin slice (dx in mathematical models) of the propellant that moves from the deep solid (unaffected state, ambient temperature) towards the wall (at high temperature) at the propellant regression rate eigenvalue $\bar{r}$. The lower the regression rate $\bar{r}$, the longer the time that the propellant material spends in the high-temperature regions near the wall; this favors large variations in the physical properties. Until accurate experimental data become available on material properties, covering a wide range of temperature, the above influence is difficult to test, but at least the discussion indicates that uncertainties should increase with coarser oxidizer (lower regression rate) propellants.

Finally, considering the usual uncertainties in such comparisons, the agreement in table 7.1 should not be very discouraging.

7.4 The Amplitude of Pressure Oscillations

An understanding of the L^* instability in rockets should result in an acceptable explanation of the amplitude of pressure oscillations. It is to be recognized that we have in question a nonlinear phenomenon, since finite amplitudes are encountered in an isolated system. In the literature on L^* instability, pressure amplitudes are mentioned[6] only rarely. At least a few of the reasons for this negligence will probably become obvious before the end of this section.

The pressure oscillations are driven by the burning propellant. The fact that the amplitude does not grow indefinitely indicates the simultaneous operation of a loss mechanism. The maximum amplitude observed at any instant is a dynamically controlled parameter in a non-stationary system, and

hence the imprecise nature of conventional terminology like "the limiting amplitude" must be clearly recognized. Nevertheless, the amplitude of pressure oscillations is a very important quantity in rocket design. Hence, several correlations were attempted to elucidate possible mechanisms controlling the "limiting amplitude." It is noted that at this stage a completely satisfactory explanation has not been possible. This incomplete success is reflected in correlations that are less than satisfactory.

All of the data on the Helmholtz oscillations have shown a general decrease in the amplitude(s) with increasing L^*, except for the rapid growth region near the initial stages; see, for example, figs. 4.1b, 4.1d, 6.1a. Thus, one is naturally led to a plot of P' vs. L^* (fig. 7.12). The correlation for the CIT-2 propellant is satisfactory. The same cannot be said of the other three propellants. It is fairly evident that the fundamental effect behind the limiting amplitude is still obscure.

The next logical step would be to attempt correlations of suitably normalized variables. In the absence of even a rudimentary understanding of the phenomenon, it is difficult to determine what constitutes a suitable normalization. The first attempt is presented in fig. 7.13 which indicates that a physical examination of the relevant processes may prove more helpful.

A simple way of visualizing the Helmholtz oscillations is to consider periodic charging and discharging of the chamber free volume with the combustion gases. At a mean regression rate $(\bar{r})$ and a chamber free volume V, the "driving force" or the energy density behind the oscillations is obviously proportional to $(\bar{r}/V)$. If the pressure amplitude is indeed controlled by such a simple phenomenon, correlations of P' versus $\bar{r}/V$ should be better than the previous ones. Figure 7.14 shows that such is indeed the case, although the scatter in the data points is quite large.

The above reasoning shows that it is always the absolute magnitude of the pressure amplitude (P') that is important and not the relative amplitude like (P'/$\bar{p}$), for example. The plot in fig. 7.15 was prepared to further strengthen this argument.

There exists a parameter of importance to L^* instability, which incorporates in it all of the significant variables. The significant variables are the L^* and the mean regression rate ($\bar{r}$) determined by the experimenter, and the frequency (f) determined by the motor itself. The parameter $L^* f/\bar{r}$ is thus a "constrained" parameter which should probably not be used to correlate any of the three variables it incorporates. However, the dynamically determined pressure amplitude could have a meaningful correlation with this "constrained parameter." The plot in fig. 7.16 shows that the correlation for each particular propellant is good indeed.

The chamber free volume varies from run to run. But, for the purposes of volumetric energy density calculations, an "equivalent" chamber volume has to be considered. Since the frequency correlations obtained earlier (section 7.2) strongly indicate the importance of the natural regression rate ($a_{100}f$), the observed regression rate is normalized as

$$\bar{r}/a_{100}f \ .$$

Now, the equivalent chamber volume is written

$$V.(a_{100}f/\bar{r}) \ .$$

Since the propellant density and the chamber cross-sectional area are the same for all of the tests, the variable ($a_{100}f/\bar{r}$) represents, on a relative scale, the mass of the propellant entering the chamber during each cycle. The equation of state (P = ρRT) for the combustion gases indicates that the pressure increase due to this mass addition should be proportional to $\dfrac{\bar{r}}{a_{100}f} / V$, since

the gas temperature is approximately constant under all conditions encountered. The correlation is shown in fig. 7.17. There appears to be an unmistakable trend, even among the scattered data points.

Before ending this section, a few of the possible explanations are given for the great difficulty encountered in pressure amplitude correlations.

(i) The phenomena are so nonlinear that simple treatments are not meaningful.

(ii) The amplitude, at least during the initial stages in many of the runs, is strongly controlled by the ignition pulse, which is a random variable.

(iii) During many of the runs, the amplitude of pressure oscillations results in cyclic choking and unchoking of the nozzle; this could introduce a new factor of uncertainty.

Fig. 7.12 MEASURED PRESSURE AMPLITUDE VS. THE CHARACTERISTIC LENGTH

CIT-2 Propellant
$\widetilde{A}$-13 Propellant
CIT-3 Propellant
CIT-4 Propellant

p' (PSI)

L* cm
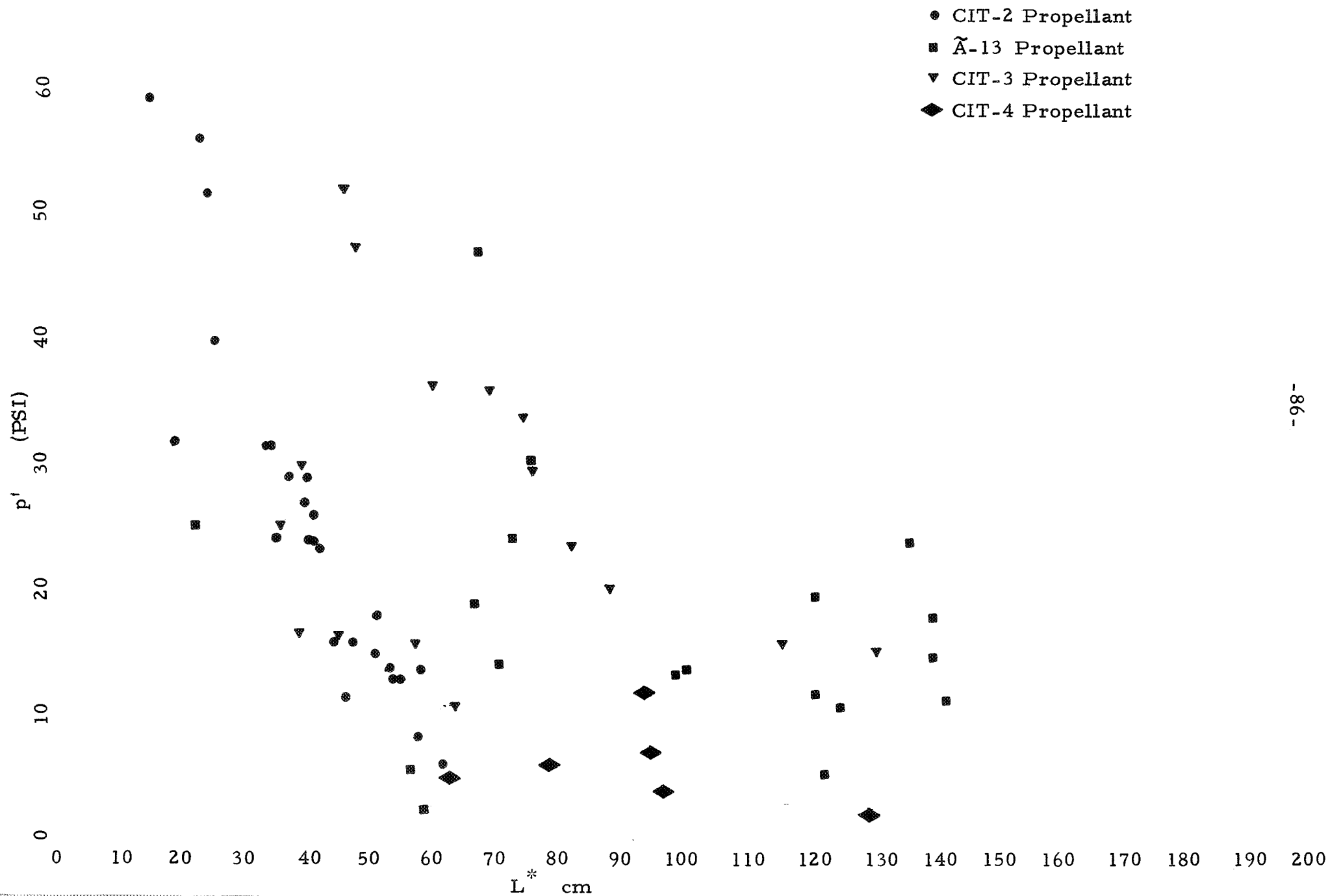
Fig. 7.13 NORMALIZED PRESSURE AMPLITUDE VS. NORMALIZED L*.

- CIT-2 Propellant
- $\widetilde{A}$-13 Propellant
- CIT-3 Propellant
- CIT-4 Propellant

$P'/\overline{P}$

$(L^* r/n) \times 10^{-4}$
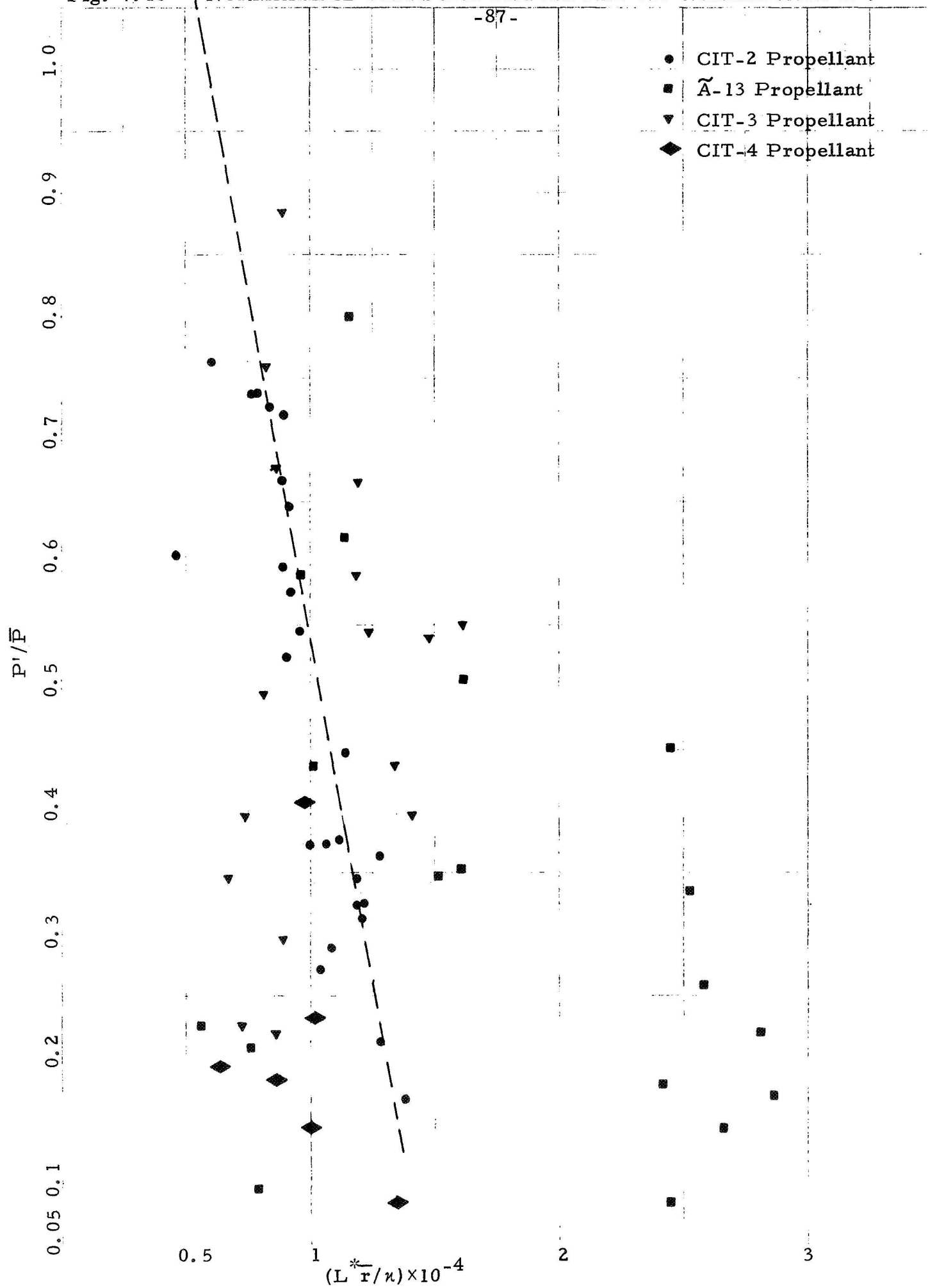
Fig. 7.14 MEASURED PRESSURE AMPLITUDE VS. INVERSE VOLUMETRIC ENERGY DENSITY

Pt. A Pt. B
● ○ CIT-2 Propellant
▨ ▢ $\widetilde{A}$-13 Propellant
▼ ▽ CIT-3 Propellant
◆ ◇ CIT-4 Propellant

P' (psi)

(Chamber Free Volume $V_{c.c.}$) ÷ (Mean Regression Rate $\bar{r}$ cm/sec) cm^2 sec

-88-
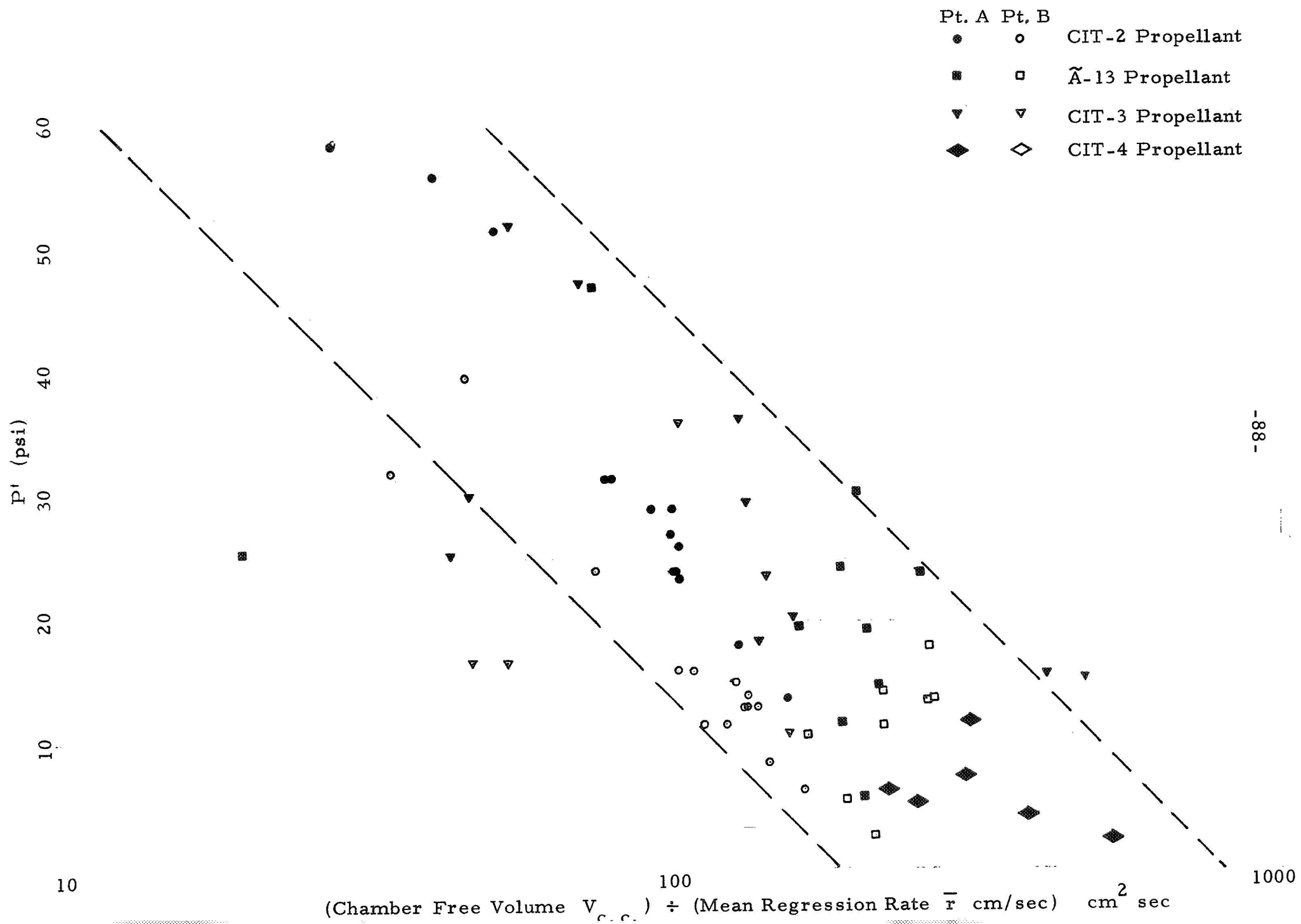
Fig. 7.15 NORMALIZED PRESSURE AMPLITUDE VS. INVERSE VOLUMETRIC ENERGY DENSITY

(Chamber Free Volume $V_{c.c.}$) ÷ (Mean Regression Rate $\bar{r}$ cm/sec) $cm^2 \cdot sec$

$(P^!/\bar{P})$
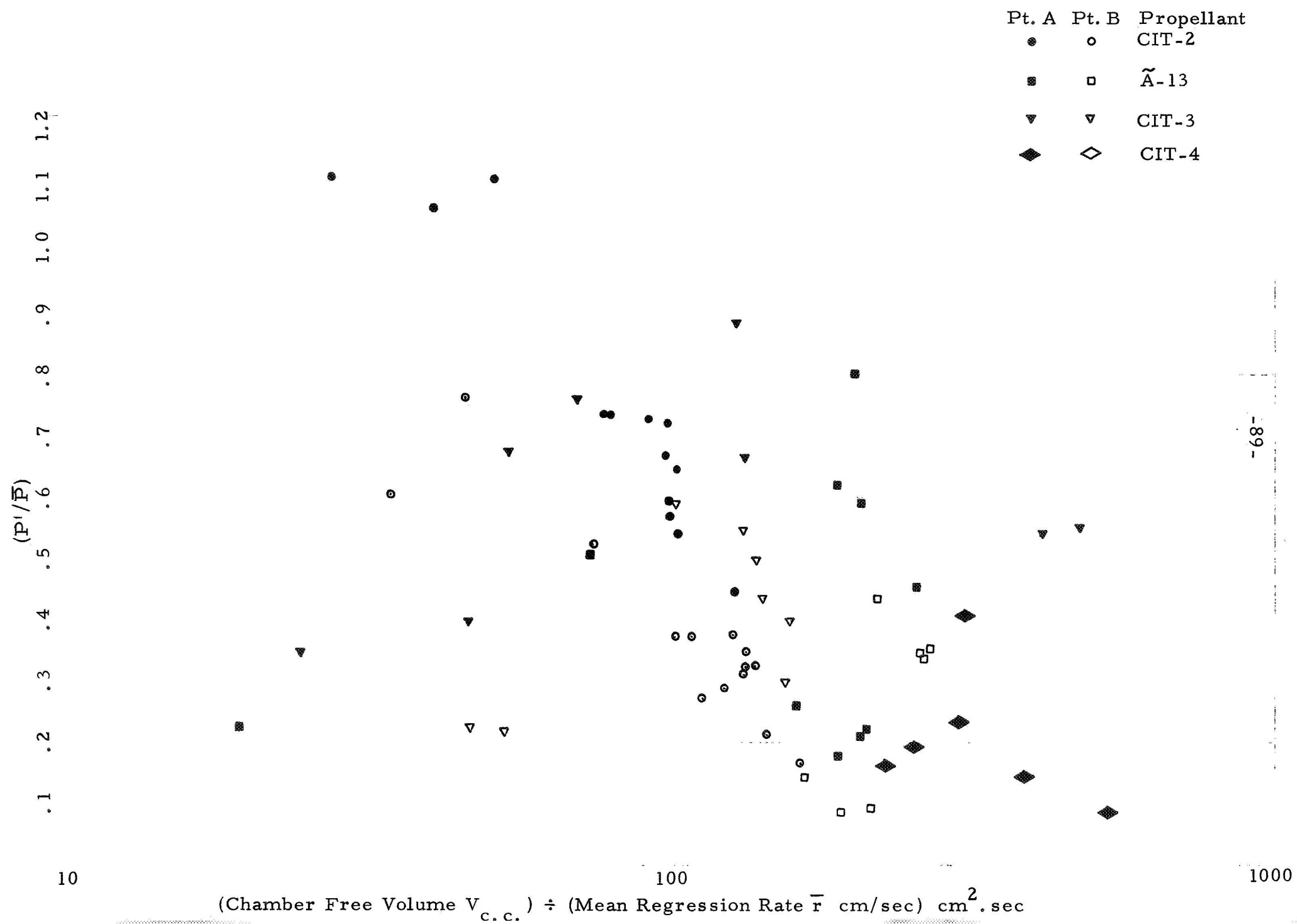
Fig. 7.16 NORMALIZED PRESSURE AMPLITUDE VS. THE "CONSTRAINED" PARAMETER

Pt. A Pt. B

●   ●   CIT-2 Propellant

▩   ▩ $\widetilde{A}$-13 Propellant

▼   ▼   CIT-3 Propellant

◆   ◆   CIT-4 Propellant

$(P'/\overline{P})$

The "Constrained" Parameter $(L^* f/\overline{r}) \times 10^{-4}$
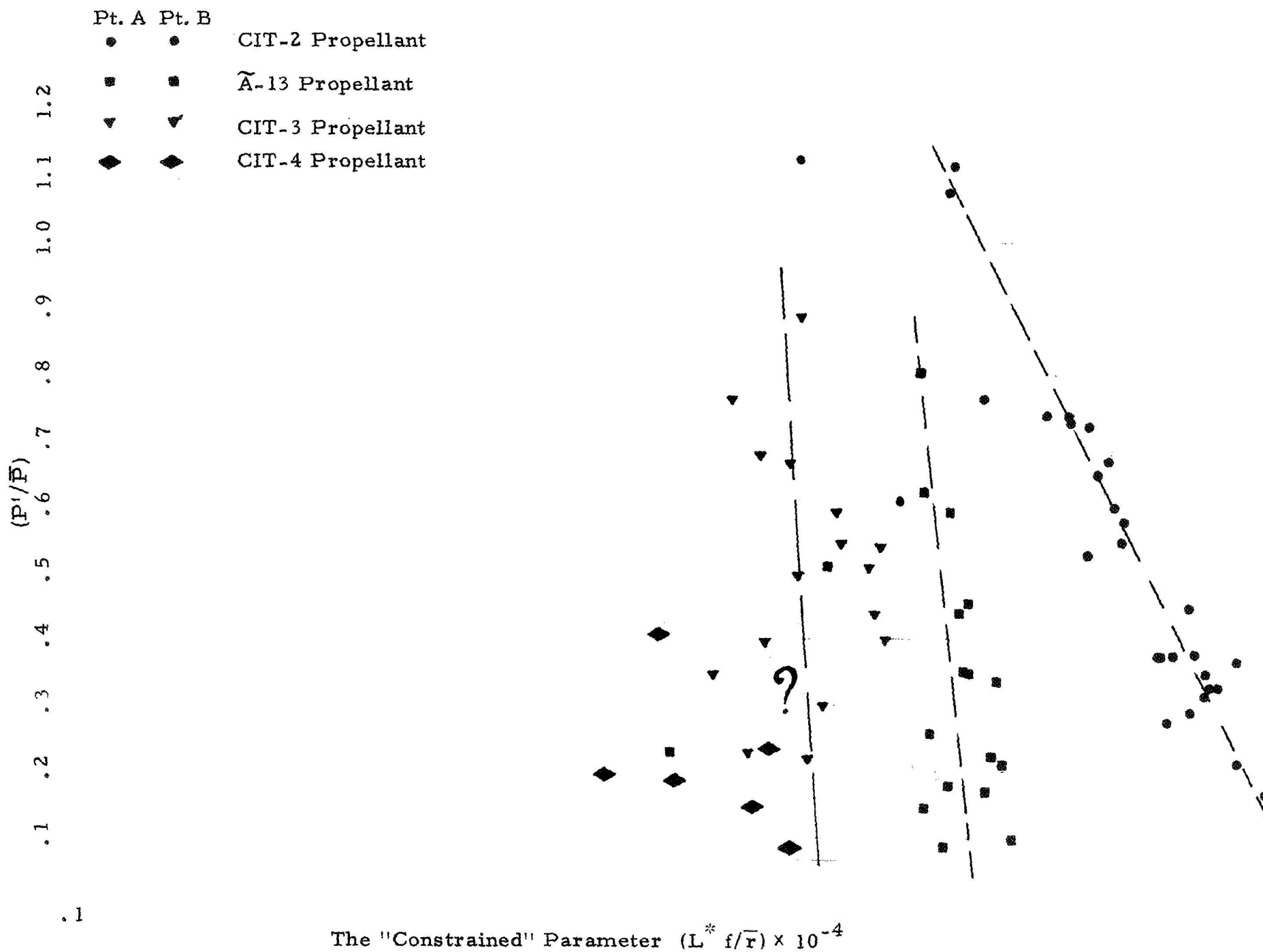
Fig. 7.17 Measured Pressure Amplitude Vs. Equivalent Free-Volume of Combustion Chamber.

CIT-2 Propellant (11 μ)

$\widetilde{A}$-13 Propellant (39.5 μ)

CIT-3 Propellant (175 μ)

CIT-4 Propellant (350 μ)

P' (psi)

V $(a_{100}f/\bar{r})$ cm^3
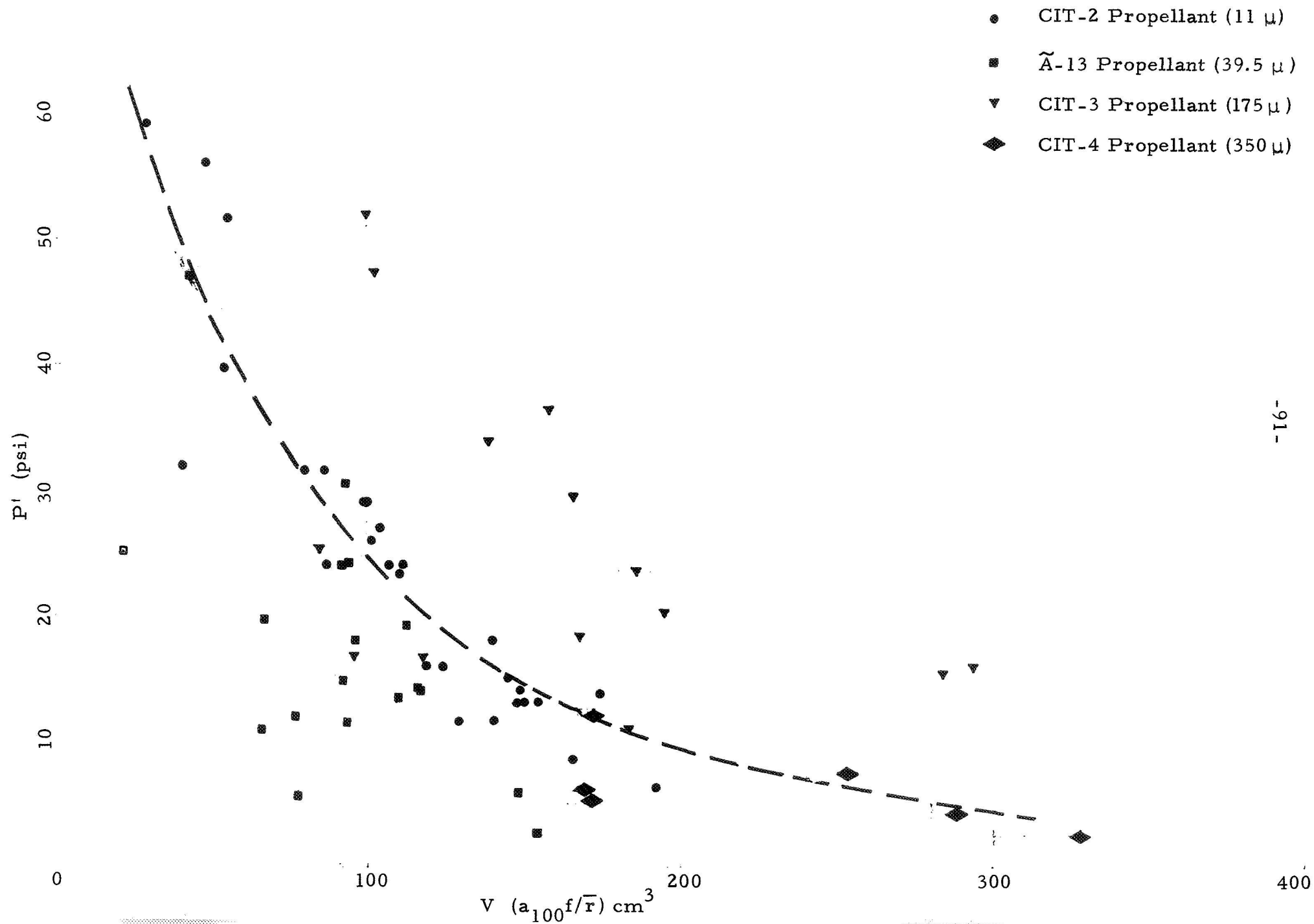
VIII. CONCLUDING REMARKS

This experimental work on L^* instability in solid-propellant rocket motors has yielded a variety of significant information. Many of the observed experimental trends are completely in agreement with anticipations based on qualitative arguments and previous experimental work. However, some of the trends are novel. The following remarks constitute a general summary of the present findings. These remarks are necessarily divided into two classes regarding pertinence to the mode of instability (common to all four of the propellants) and the propellants themselves (compositional variations).

Depending on the combinations of the two primary variables in rocket motor operation (characteristic length, L^*, and the mean pressure, $\bar{P}$), three fundamentally different types of pressure-time histories are observed. These are the chuff mode, Helmholtz mode, and the steady mode. As a slight variation, there exists the pressure burst phenomenon, where the rapidly growing Helmholtz oscillations result in a depressurization-rate (dp/dt) extinghishment of combustion.

Of the three principal modes of L^* instability, the Helmholtz mode is the most ordered. It is one-dimensional in nature. It may be excited only over a narrow range of values of L^* and $\bar{P}$. Besides, even when the $L^* - \bar{P}$ combination permits the Helmholtz mode, a large amplitude pressure disturbance seems to be necessary for its initiation. In general, the frequency of Helmholtz oscillations decreases with increasing values of L^* for a given propellant. The amplitudes of pressure oscillations during a firing are observed to decrease with increasing L^*; however, this trend is seen to lack generality when a large number of varied firings are considered. Even through the mist of data-scatter associated with the pressure amplitudes, the

ratio of chamber free volume to the mean regression rate is seen to be more relevant than the value of L^*.

The chuff mode is far from being one-dimensional. The nozzle is unchoked during most, if not all, of the chuff duration. Severe distortions of the propellant surface and combustion over isolated regions of the surface are evident. The events behind a chuff (pressure spike) are random, and are interpreted only in a statistical sense. Back flow of ambient gases into the chamber is seen as a definite possibility. The initiation of the chuff mode apparently bears a strong relation to the ignition technique. Copious uses of the ignitor paste are seen at times to suppress the chuff mode completely.

The "steady" mode is seen to involve an intrinsic "noise" level of pressure fluctuations. The random amplitude is seen to be nearly independent of the propellant, generally.

The pressure-burst phenomenon is best described as a short-time segment of the more general Helmholtz mode. Preceding the (dp/dt) extinguishment, generally speaking, the mean chamber pressure gradually decreases, although it is not always the case.

The stability boundary for L^* mode is parabolic, with dual values of mean pressure, in the L^* range of interest.

The coarser the oxidizer particles in a propellant, the more difficult it is to obtain data. The coarser oxidizer particle propellants are more difficult to ignite, enter the Helmholtz mode only with great difficulty, and are prone to depressurization-rate extinguishment even under mild conditions. As a corollary, the finer oxidizer particle propellants continue to burn even under severe (dp/dt) transients.

The oxidizer particle size directly controls the frequency of Helm-

holtz oscillations. On a meaningful relative basis, the coarser the oxidizer particles, the lower the frequency. As far as the particle size itself is concerned, the 100 per cent weight average point is more meaningful than the familiar 50 per cent weight average point. In the context of Helmholtz oscillations, the oxidizer particle size is a more important parameter than the often-used thermal depth $(\varkappa/\bar{r})$ in the solid. In every one of the tests conducted, the value of the parameter $(f a_{100})$ exceeded the mean regression rate $(\bar{r})$; that is, the important parameter $(f a_{100}/\bar{r})$ was never found to have a value less than unity.

Several of the observed effects (normalized frequency, high-pressure stability limit, etc.) do not vary monotonically with the oxidizer particle size. For example (see fig. 7.3), the frequency variable $(f a_{100}/\bar{r})$ increases in the following order of the oxidizer particle size: 39.5, 11, 350, 175.

When the oxidizer particle size is very fine, the behavior is different from the general trends, even qualitatively. This is amply demonstrated by the data on the CIT-2 $(11\,\mu)$ propellant.

(i) The frequency of Helmholtz oscillations is almost independent of, and increases slightly with, the value of L^{*} (decreases markedly for the other three propellants).

(ii) The frequency is almost independent of the mean regression rate (generally increases, rather strongly, for the other three propellants).

(iii) The pressure oscillations during the Helmholtz mode are distorted, i.e., possess higher harmonics to a significant degree (almost symmetrical, if not sinusoidal for the other three propellants).

(iv) The noise-level pressure amplitude is practically indiscernible (approximately 1 - 2 psi for the other three propellants).

(v) The amplitudes of the pressure oscillations during the Helmholtz

mode correlate <u>very well</u> with the value of L^* (poor correlation with L^* for the other three propellants).

(vi) The high pressure limit for unconditional stability matches excellently with the concept of thermal depth/heterogeneity in the propellant material (fair to poor agreement for the other three propellants).

Throughout the present study, the importance of condensed phase details (exemplified by the oxidizer particle size, characteristic thermal depth in the solid, ...) is felt in various different forms. These range from the ease of ignition to observed pressure amplitudes, resistance against (dp/dt) extinguishment to correlations of frequency. In general, the more homogeneous the solid, the more readily does the propellant exhibit instability. This general observation is consistent with the feeling that the important role of the condensed phase, in acting like a heat reservoir through the $c \cdot \Delta T$ term, is very effective if the solid is homogeneous. Also, attempts to increase the mechanical strength of propellants by adding ingredients that promote a bond between the oxidizer crystals and the binder (thereby increasing the homogeneity of the solid) have resulted in marked increases in the instability behavior. Those experiments will be reported separately; here, it suffices to note the satisfactory trend in agreement with the observations on the present propellants.

To summarize, the oxidizer particle size in the propellant is revealed as an important parameter that has strong influences on L^*-instability behavior.

APPENDIX I.   THE LOW BACK-PRESSURE FACILITY

Most of the quantitative information on L-star instability is obtained from the ordered Helmholtz mode. In order to excite the Helmholtz mode, a deep thermal profile in the solid (relative to the oxidizer particle size) seems to be necessary. Deep thermal profiles are favored at low values of mean regression rate; and the burning rate law ($\bar{r} = a\bar{P}^n$) leads to low chamber pressures.

Since a choked nozzle is almost a necessity for obtaining good data, low chamber pressures require a low back pressure (approximately $P_c/P_a \geq 2$). The L^* burner hardware was adapted to match an existing vacuum manifold. The design is shown in figure A1. Although no useful data were obtained during the present program, this facility exists in operating condition, and is described here.

The vacuum system consists of a $6\frac{1}{2}''$ pipe (P) communicating with a ≈ 150 cu. ft. tank (R) which can be maintained at a pressure level of 3 mm of mercury by a 80 cfm displacement piston pump (D). The nozzle end plate (N) of the L^* burner is rigidly bolted to the flange (F) with pressure sealing through the "O" ring at O . A $1/8''$ diameter radial hole (h_1) communicates with an axial blind hole (h_2) drilled at a distance of $7/8''$ from the axis of the motor assembly. The peripheral end of the radial hole is machined to take an 1/8 NPT pipe fitting which is used to attach the pressure gage (S) to the motor chamber. The ignitor wires are led out through a McCormick fitting (Mc) that seals pressure with the nozzle end plate.

Since the Taber gage pressure transducer is not suitable for negative (subatmospheric) pressures, a Statham (PA-822-200) pressure transducer was used in these tests.

Ignition at low subatmospheric pressures naturally presented insurmountable problems. Relatively high pressures ($\sim 10''$ of mercury) are needed at least temporarily. A rupture diaphragm was bonded to the nozzle face; the ignition pressure pulse ruptured the diaphragm and communication was established between the motor chamber and the vacuum manifold.

However, the depressurization rate during the diaphragm rupture was so great that the propellant got extinguished in every one of the tests employing the diaphragm. A new method of testing was tried consequently.

The valve (L) between the manifold and the large vacuum tank was kept closed at ignition, so that the motor chamber pressure was at the ambient value. After the chamber pressure was observed to register a higher value, corresponding to the establishment of regular combustion of the propellant, the valve was gradually opened to lower the manifold pressure during the firing. In this manner the (dP/dt) transient was kept very mild. Even with this arrangement, the propellant got extinguished each time the chamber pressure reached a value much lower than atmospheric. Since this extinguishment was very reproducible, at various speeds of opening the valve, it was felt that the low pressure combustion limit of the propellant might be the cause. Propellants have been known not to burn below a certain pressure level, the value of which varies with the individual propellant. Attempts would be futile to run the rocket motor at pressures below this limit.

Since the low pressure limits were unknown for the propellants of the present study, an experimental facility (see fig. A2) was constructed to determine these limits. A sealed plexiglas cylinder (A) has provision for holding a strand (approximately circular and 1/4'' diameter) of the propellant (P). The chamber communicates with a vacuum pump (V) through the cold trap (T) in which are condensed vapors evolving during the combustion of the propellant

strand.

At the time of the present report, the low-pressure combustion limits have not yet been obtained. The cold trap was not found to be very effective in any of the numerous tests conducted so far. This results in the contamination of the vacuum pump with the vapors from the propellant. It is to be recognized that at very low pressures in the chamber, the vapors are (probably) potentially combustible due to incomplete oxidation. The hazards of contamination of such vapors with the oil mist in the **piston** pump (V) are readily appreciated.

The facility exists in working condition for obtaining data when once an efficient cold trap is available.
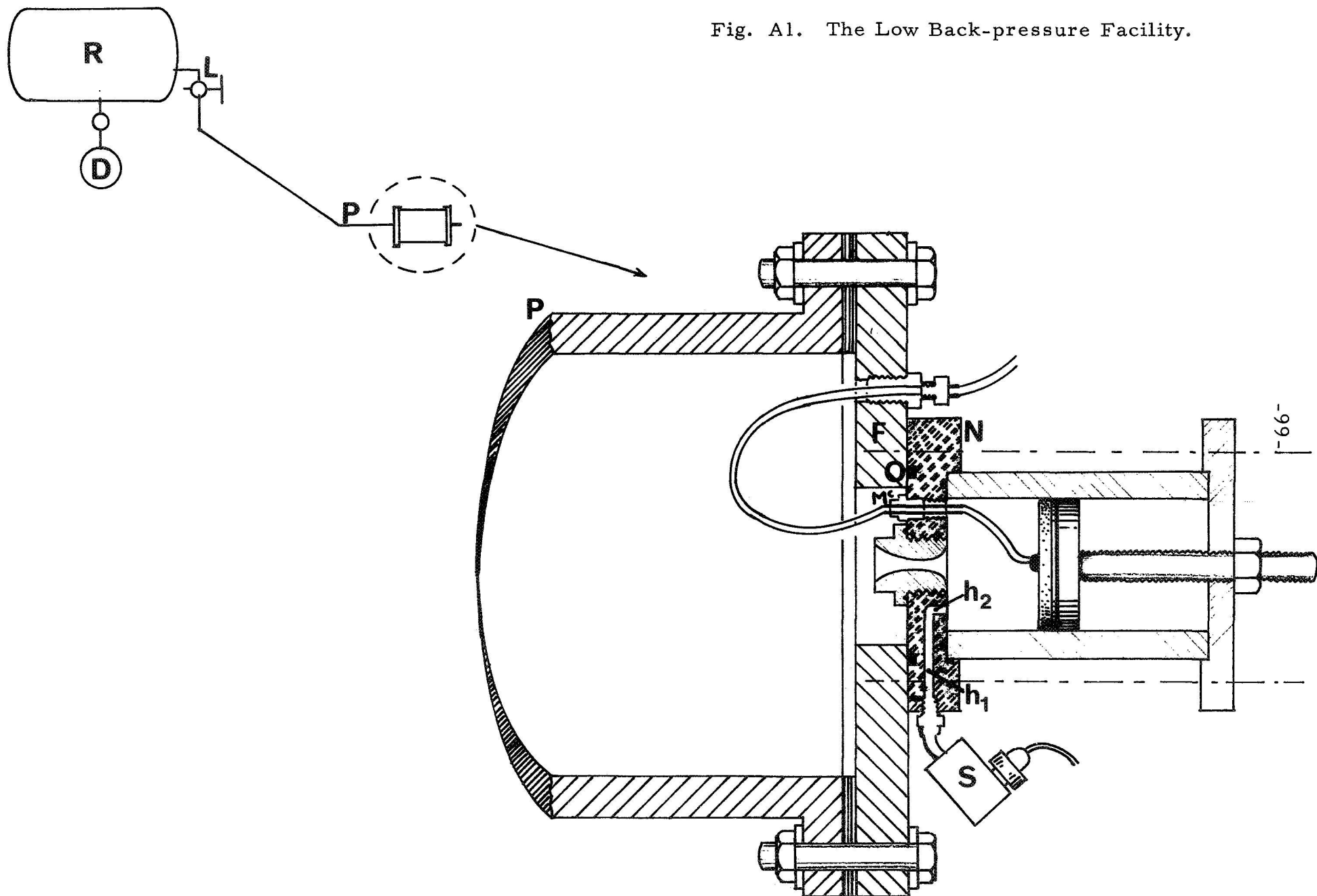
Fig. A1. The Low Back-pressure Facility.

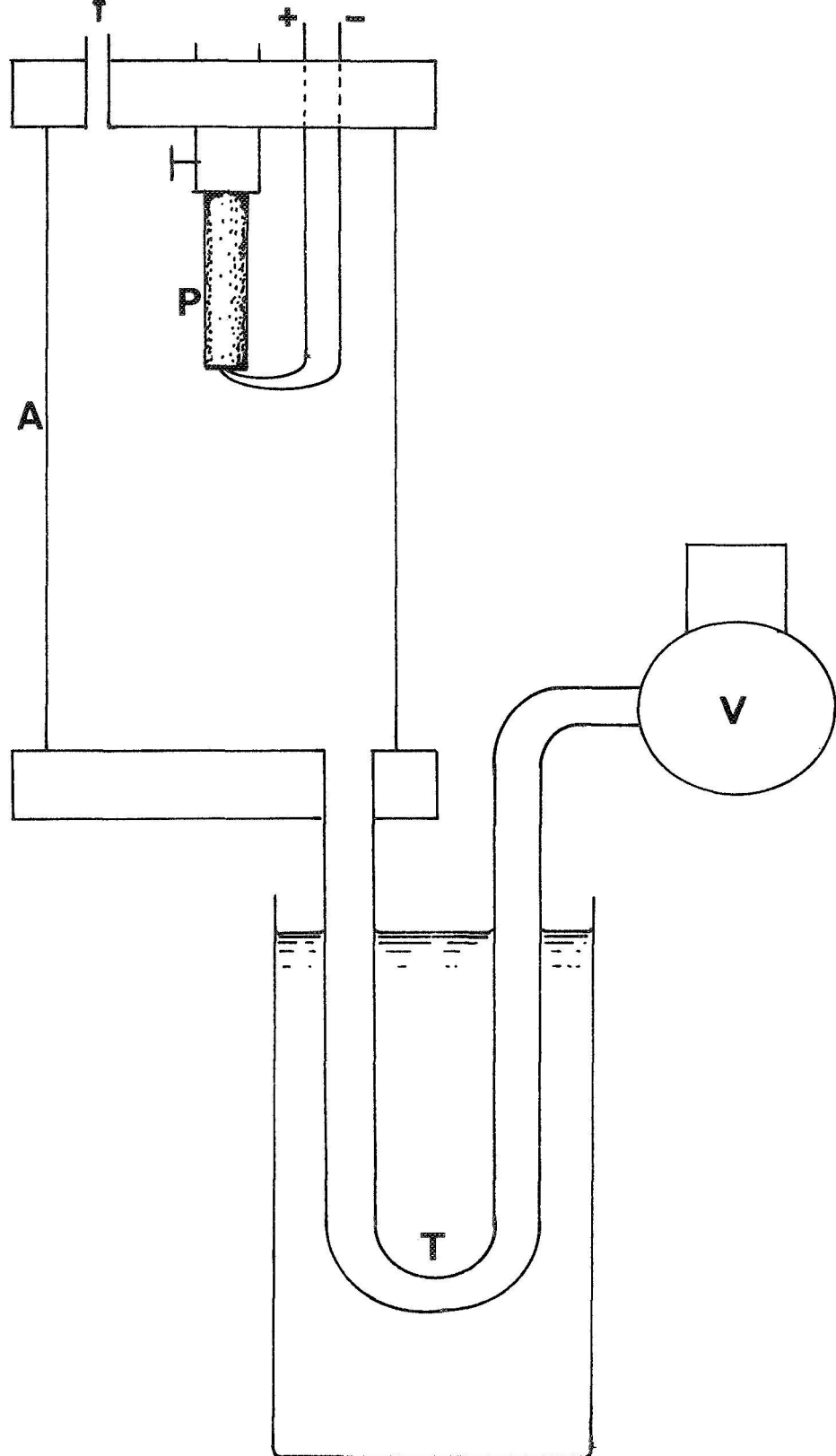Fig. A2. Experimental Setup for the Determination of the Low-pressure Combustion Limit of Propellants.

TABLE A1. PROCESSED DATA; CIT-2 (11 μ) PROPELLANT

Run No.	$\bar{P}$ psia	L^* cm	P' psi	$\dfrac{P'}{\bar{P}}$	$\dfrac{L^*_f}{\bar{r}}$	$\dfrac{L^*\bar{r}}{\varkappa}$	$\Omega = \dfrac{f\varkappa}{\bar{r}^2}$	$\dfrac{fa_{100}}{\bar{r}}$	$V/\bar{r}$ cm²sec	$V(\dfrac{fa_{100}}{\bar{r}})$ cm³
16	52.70	15.40	59.20	1.123	13471.4	3733.8	3.608	3.761	28.482	28.573
16	52.70	19.09	31.95	.606	19090.0	4628.5	4.124	4.300	35.306	40.489
17	52.10	22.30	55.90	1.073	22514.4	5355.2	4.204	4.341	41.639	47.753
17	52.10	25.13	39.70	.762	25371.6	6034.9	4.204	4.341	46.924	53.813
19	46.10	24.20	51.60	1.119	23385.8	5532.1	4.227	4.155	52.144	54.485
19	46.10	35.30	24.10	.523	37060.4	8069.6	4.593	4.514	76.061	86.344
22	42.80	33.90	31.50	.736	31868.1	7671.3	4.154	4.042	78.837	79.326
22	42.80	47.30	15.90	.371	49785.5	10703.6	4.651	4.526	110.000	123.926
23	42.80	34.90	31.50	.736	34350.4	7897.6	4.349	4.232	81.163	85.505
23	42.80	44.20	15.90	.371	47588.0	10002.1	4.758	4.630	102.791	118.456
24	39.92	37.40	29.00	.726	34510.3	8290.6	4.163	3.968	94.127	91.061
24	39.92	50.90	15.00	.376	53855.8	11283.1	4.773	4.550	128.094	142.108
25	40.55	39.95	27.00	.666	39320.9	8855.8	4.440	4.232	100.538	103.755
25	40.55	53.65	13.00	.321	56765.5	11892.7	4.773	4.550	135.015	149.785
26	41.80	41.10	24.00	.574	41703.9	9205.7	4.530	4.363	102.955	110.676
26	41.80	53.65	13.00	.311	55527.0	12016.6	4.621	4.450	134.392	147.361
27	40.30	40.15	29.00	.720	37047.9	8900.2	4.163	3.968	101.622	98.320
27	40.30	53.35	14.00	.347	55791.7	11826.2	4.718	4.497	135.033	148.063
28	40.30	41.25	26.00	.645	38062.9	9144.0	4.163	3.968	104.407	101.013
28	40.30	54.95	13.00	.323	58141.0	12180.9	4.773	4.550	139.082	154.298
29	40.30	51.30	18.00	.447	52596.0	11371.8	4.625	4.409	129.844	139.582
29	40.30	57.80	8.50	.211	62341.7	12812.7	4.866	4.638	146.296	165.446
30	42.80	42.20	23.30	.544	41535.4	9549.5	4.349	4.232	104.631	110.229
30	42.80	46.20	11.60	.271	48627.7	10454.6	4.651	4.526	114.549	129.051
31	40.30	40.50	24.00	.596	40194.4	8977.7	4.477	4.268	102.508	106.670
31	40.30	49.10	11.60	.288	52756.7	10884.1	4.847	4.620	124.276	140.009
41	38.10	58.30	13.75	.361	62334.9	12788.9	4.874	4.598	156.905	174.070
41	38.10	61.90	6.30	.165	68749.3	13578.6	5.063	4.776	166.593	191.982

TABLE A2. PROCESSED DATA; $\tilde{A}$-13 (39.5μ) PROPELLANT

Run No.	$\bar{P}$ psia	L^* cm	P' psi	$\dfrac{P'}{\bar{P}}$	$\dfrac{L^* f}{\bar{r}}$	$\dfrac{L^* \bar{r}}{\varkappa}$	$\Omega \equiv \dfrac{f\varkappa}{\bar{r}^2}$	$\dfrac{fa_{100}}{\bar{r}}$	$\dfrac{V/\bar{r}}{cm^2 sec}$	$V(\dfrac{fa_{100}}{\bar{r}})$ cm^3
127	53.10	136.00	23.90	.450	24369.1	24494.8	.995	1.792	257.340	91.356
127	53.10	140.00	17.90	.337	26605.1	25215.3	1.055	1.900	264.908	99.738
147	67.30	139.70	14.81	.220	26235.6	28064.5	.935	1.878	219.889	91.254
147	67.30	142.00	11.40	.169	25703.7	28526.5	.901	1.810	223.510	89.404
149	76.20	121.00	19.65	.258	21115.1	25844.5	.817	1.745	163.098	66.870
149	76.20	125.00	10.80	.142	20749.1	26698.9	.777	1.660	168.490	65.711
155	92.80	68.60	47.00	.506	14854.3	16157.2	.919	2.165	75.361	42.277
157	67.00	121.00	11.87	.177	22579.8	24168.1	.934	1.866	191.556	78.538
157	67.00	122.70	5.55	.083	22338.5	24507.7	.911	1.821	194.248	77.699
160	28.20	56.65	5.85	.207	27379.0	7587.0	3.609	4.833	208.349	148.345
160	28.20	58.85	2.63	.093	28442.3	7881.6	3.609	4.833	216.441	154.106
161	32.55	67.00	19.20	.590	22719.1	9592.0	2.369	3.391	209.854	112.062
161	32.55	71.00	14.17	.435	23534.4	10164.6	2.315	3.315	222.382	116.084
163	38.00	76.00	30.40	.800	20562.4	11670.1	1.762	2.706	202.465	92.526
163	38.00	99.00	13.45	.354	24323.6	15201.9	1.600	2.457	263.737	109.451
164	111.90	22.40	25.15	.225	8554.3	5689.6	1.504	3.819	20.202	21.555
170	39.10	72.70	24.20	.619	20852.3	11331.3	1.841	2.870	190.804	93.876
170	39.10	103.00	13.78	.352	24030.3	16054.0	1.497	2.333	270.328	108.131

TABLE A3. PROCESSED DATA: CIT-3 (175 μ) PROPELLANT

Run No.	$\bar{P}$ psia	L^* cm	P' psi	$\dfrac{P'}{\bar{P}}$	$\dfrac{L^*f}{\bar{r}}$	$\dfrac{L^*\bar{r}}{\varkappa}$	$\Omega \equiv \dfrac{f\varkappa}{\bar{r}^2}$	$\dfrac{fa_{100}}{\bar{r}}$	$\dfrac{V/\bar{r}}{2}$ cm²sec	$V\!\left(\dfrac{fa_{100}}{\bar{r}}\right)$ cm³
45	27.90	131.00	15.35	.550	17159.5	16183.3	1.060	4.388	475.501	283.541
46	29.40	116.50	15.85	.539	17762.7	14795.5	1.201	5.108	411.336	293.509
68	37.15	57.50	18.36	.494	13358.2	8032.7	1.663	7.783	140.273	167.760
68	37.15	64.00	10.95	.295	14576.7	8940.8	1.630	7.630	156.130	183.063
71	41.05	60.25	36.30	.884	13554.6	8764.7	1.546	7.537	130.962	157.940
74	54.30	76.10	29.50	.543	15525.8	12546.5	1.237	6.835	132.890	164.717
74	54.30	82.30	23.60	.435	17426.1	13568.7	1.284	7.093	143.716	184.877
75	50.90	74.70	33.90	.666	13106.4	11901.7	1.101	5.878	134.982	139.048
75	50.90	88.30	20.20	.397	18339.2	14068.6	1.304	6.958	159.557	194.564
79	77.00	45.70	52.00	.675	11716.8	8653.1	1.354	8.589	55.289	98.906
90	61.00	47.70	47.30	.775	10612.3	8205.7	1.293	7.453	71.744	101.184
90	61.00	69.20	36.00	.590	15249.4	11904.3	1.281	7.382	104.081	145.396
92	76.00	39.25	30.00	.395	12060.7	7431.8	1.623	10.294	47.485	101.809
92	76.00	45.20	16.65	.219	13889.0	8558.4	1.623	10.294	54.684	117.242
97	73.60	36.00	25.20	.342	9789.6	6799.8	1.440	9.110	43.660	82.637
97	73.60	39.10	16.67	.226	11150.1	7385.4	1.510	9.553	47.420	94.122

TABLE A4.   PROCESSED DATA: CIT-4 (350 μ) PROPELLANT

Run No.	$\bar{P}$ psia	L^* cm	P' psi	$\dfrac{P'}{\bar{P}}$	$\dfrac{L^* f}{\bar{r}}$	$\dfrac{L^* \bar{r}}{\kappa}$	$\Omega \equiv \dfrac{f\kappa}{\bar{r}^2}$	$\dfrac{fa_{100}}{\bar{r}}$	$V/\bar{r}$ cm²sec	$V\left(\dfrac{fa_{100}}{\bar{r}}\right)$ cm³
167	34.00	78.90	6.15	.181	8697.6	8653.9	1.005	6.173	227.463	169.414
168	31.93	95.10	7.36	.231	12077.7	10211.1	1.183	7.112	301.849	253.553
171	29.57	93.95	11.90	.402	8219.6	9762.3	.842	4.899	308.139	172.558
172	26.95	63.20	5.15	.191	6821.0	6319.0	1.079	6.044	258.575	171.880
173	29.10	97.50	4.15	.143	11447.0	10063.6	1.137	6.575	386.415	288.451
174	28.50	132.10	2.40	.084	13031.3	13512.9	.964	5.524	528.270	328.373

REFERENCES

1. Schöyer, H. F. R., "Report on Low-Frequency Oscillatory Combustion Experiments," Daniel and Florence Guggenheim Jet Propulsion Center, California Institute of Technology (1971).

2. Strand, L., "Low Pressure Combustion Studies," JPL Space Programs Summary 37-41, vol. IV, p. 85 (October 31, 1966).

3. Perry, E. H., "Investigations of the T-burner and its Role in Combustion Instability Studies," Ph. D. Thesis, California Institute of Technology (1970).

4. Kumar, R. N., "Some Considerations in the Combustion of AP/Composite Propellants," Daniel and Florence Guggenheim Jet Propulsion Center, California Institute of Technology (August 1972).

5. "Combustion of Solid Propellants and Low Frequency Combustion Instability," NOTS TP 4244 (June 1967).

6. Yount, R. A. and Angelus, T. A., "Chuffing and Nonacoustic Instability Phenomena in Solid Propellant Rockets," AIAA Preprint No. 64-148 (1964).

7. Horton, M. D. and Rice, D. W., "Effect of Compositional Variables upon Oscillatory Combustion of Solid Rocket Propellants," Combustion and Flame, vol. 8, p. 21 (March 1964).

8. Barrere, M., Nadaud, L., and Lhuillier, J. N., "Survey of ONERA and SNPE work on Combustion Instability in Solid Propellant Rockets," AIAA Preprint No. 72-1052 (1972).